Nonclassical and coherent emission from trapped ion crystals

Ph.D. thesis by

Petr Obšil

Palacký University Olomouc

2021

Title:	Nonclassical and coherent emission from trapped ion crystals
Author:	Ing. Petr Obšil
ORCID:	0000-0003-1020-3023
Advisor:	prof. Mgr. Radim Filip, Ph.D.
Consultant:	Mgr. Lukáš Slodička, Ph.D.
Study programme:	Optics and Optoelectronics (full-time form)
Institution:	Department of Optics, Faculty of Science, Palacký University Olomouc
Year:	2021
Pages:	105

Abstract

The thesis is dedicated to quantum optics experiments with trapped and laser-cooled $^{40}Ca^{+}$ ions. It presents the generation and observation of coherent and nonclassical light emission from trapped ion crystals and the possibility of its scaling to large ionic ensembles.

The ions are spatially localized in a linear Paul trap in the ultra-high vacuum chamber. The lifetime of an ionic crystal is inversely proportional to the vacuum pressure, therefore it is crucial to reach a sufficiently low pressure of the background gas for the scalable atomic ensemble. The thesis is concerned by a detailed description of the vacuum building procedures and characterization of residual pressure by analyzation of the formation rate CaH^{+} molecules, which led to the unprecedented value of the partial pressure of hydrogen in the room temperature ion trapping apparatus[A1].

The observation of coherent emission from a large number of quantum emitters is essential for the realization of many fundamental collective phenomena in quantum optics, including directional emission, optical generation of multipartite entanglement, or direct creation of quadrature squeezing of atomic resonance fluorescence. The thesis presents the observation of interference from linear ion chains consisting of up to 53 trapped ions. The presented measurements suggest that the visibility of the observed interference patterns does not decrease with an increasing number of ions, and its phase sensitivity is close to the theoretical predictions for an ideal situation[A2].

The light emitted from single atoms is incompatible with the classical description of electromagnetic waves. Nonclassical states of light scattered by single ion prove it. In the past decade, several experiments reported on the observation of light nonclassicality from a single and few emitter ensembles, which, however, was naturally disappearing with their increasing number. The thesis describes the experimental observation of discrete nonclassical light states from ion ensembles containing up to more than a thousand of ions[A3]. The further scaling was limited solely technologically, but not fundamentally, which in the future can allow the observation of nonclassical states from an even larger number of emitters.

Keywords: Quantum optics, Trapped ions, Interference

Název:	Neklasická a koherentní emise z chycených iontových krystalů
Autor:	Ing. Petr Obšil
ORCID:	0000-0003-1020-3023
Školitel:	prof. Mgr. Radim Filip, Ph.D.
Konzultant:	Mgr. Lukáš Slodička, Ph.D.
Studijní obor:	Optika a optoelektronika (prezenční forma)
Instituce:	Katedra optiky, Přírodovědecká fakulta, Univerzita Palackého v Olomouci
Rok:	2021
Počet stran:	105

Abstrakt

Disertační práce je věnována kvantově optickým experimentům s chycenými a laserově chlazenými ionty $^{40}Ca^{+}$. Práce popisuje generaci a pozorování koherentní a neklasické emise světla z chycených iontových krystalů a možnost jejich škálovatelnosti k velkým iontovým systémům.

Ionty jsou prostorově lokalizovány v lineární Pauliho pasti uvnitř komory s ultra-vysokým vakuem. Doba života iontového krystalu je nepřímo úměrná tlaku vakua, a proto je stěžejní dosáhnout dostatečně nízkých hodnot zbytkového tlaku, aby byl systém škálovatelný v počtu atomů. Disertační práce se detailně věnuje popisu jednotlivých kroků při stavbě vakua a charakterizaci zbytkového tlaku pomocí analýzy rychlosti formování CaH^{+} molekul, což ukázalo na extrémně nízké hodnoty parciálního tlaku vodíku pro iontový systém pracující za pokojové teploty[A1].

Pozorování koherentní emise z velkého počtu kvantových zářičů je nezbytné pro realizaci mnoha základních experimentů v kvantové optice, zahrnujících směrovou emisi, optickou generaci multipartitního kvantového provázání nebo přímé vytvoření kvadraturního stlačení atomové rezonanční fluorescence. Disertační práce prezentuje pozorování interference z lineárních iontových řetízků obsahujících až 53 chycených iontů. Představená měření naznačují, že kontrast pozorovaných interferenčních křivek neklesá se vzrůstajícím počtem iontů a fázová citlivost je blízko teoretickým předpovědím pro ideální situaci[A2].

Světlo vyzářené z jednotlivých atomů není možné zapsat klasickým způsobem popisujícím elektromagnetické vlny. Neklasické stavy světla rozptýleného jedním iontem jsou toho důkazem. V poslední dekádě byla uveřejněna řada experimentů pozorujících neklasické světlo ze systému jednoho nebo několika málo zářičů, nicméně pro zvyšující se počet zářičů tato pozorovatelnost neklasičnosti přirozeně mizela. Práce popisuje experimentální pozorování diskrétních neklasických stavů světla z iontových systémů obsahujících více než tisíc iontů[A3]. Další navýšení počtu iontů narazilo na technický limit, nikoliv principiální, což v budoucnu může umožnit pozorovat neklasické stavy ještě z většího počtu zářičů.

Klíčová slova: Kvantová optika, Chycené ionty, Interference

Acknowledgements

Let me quote John Donne, who wrote: ”No man is an island, entire of itself”, which is especially true in building trapped ion setup and carrying out experiments on it. My intent on this page is to thank all co-workers, friends and family.

At first, I thank my closest post-doctoral collaborator Lukáš Slodička for mentoring, scientific discussions and all effort put into the ion experiments. I am grateful to Radim Filip for kind guidance in progressive ideas and all his hard work devoted to the ion project.

The new trapping setup was built in collaboration with colleagues in Brno. It helped with a diversity of knowledge and technical support of such complex scientific institute. Ondřej Číp, Martin Čížek, Adam Lešundák, Minh Tuan Pham and other friends put hard work into the ion trapping project, which results in attractive experiments and conjoint publications, thank you, guys.

I am thankful to the people in my home department in Olomouc, namely Lukáš Lachman for theoretical discussions, Lukáš Podhora and Jarda Mika for cooperation in the laboratory, Ivo Straka for coding tips, Miroslav Ježek, Martina Nováková, Michal Dudka, Ivan Derkach, Petr Marek, Libor Moťka and others for lifting my spirits.

I want to thank ion trappers from Innsbruck, especially Rainer Blatt for providing us with a new linear Paul trap, Stefan Haslwanter for its machining and Kirill Lakhmanskiy for its plating. I spent ten beneficial weeks there on an internship, and I want to thank Yves Colombe, Gabriel Araneda, Vojtěch Krčmarský and others for a friendly and inspiring environment.

At last, it cannot be expressed in words, how I thank my family for the wholehearted support.

Declaration

I declare the thesis is my original work. I wrote it under the guidance of my advisor prof. Mgr. Radim Filip, Ph.D. and my consultant Mgr. Lukáš Slodička, Ph.D.. The aim of the thesis is to summarize the majority of my scientific activities during my post-graduate studies. It covers assembly of the new experimental apparatus for trapping $^{40}Ca^{+}$ ions, estimation of the residual hydrogen content in the vacuum chamber[A1], observation of the coherent scattering from many trapped ions[A2], and detection of nonclassical states of light emitted by a large number of ions[A3]. The nonclassicality of light was benchmarked by the theoretical criterion proposed by Lachman et al. [1]. All resources are summarized in References. The thesis does not contain any part of the other articles [O1–O5], which I also participated but with minor contribution.

The thesis may be freely distributed in an unchanged form and Palacký University Olomouc has the rights to archive, publish and distribute the thesis according to its internal regulations and Czech law.

Olomouc
March 2021

Petr Obšil
obsil@optics.upol.cz

Contents

Chapter 1

Introduction

Since advent of quantum physics, the experiments with single atoms or molecules were highly tempting, still unattainable. The underlying difficulty is to store atoms isolated from the surrounding world, which through the interaction causes the decoherence. Technological progress allowed trapping charged ions in the sufficient vacuum last few decades and particularly the development of semiconductor lasers facilitates the manipulation of the internal atomic structure. In the beginning, the experiments were simple, still not easy to carry out, and by the time the platform of trapped ions found utilization in several main disciplines: optical atomic clocks[2], quantum computation/simulation[3,4], quantum communication[5] and fundamental research[6].

Trapped ions proved to be more promising as a frequency standard than caesium fountain[7]. Together with the frequency comb, they allowed a new generation of atomic clocks employing optical transitions. This recently lead to frequency measurement with fractional uncertainties below 10^{-18} with trapped aluminium ion[8]. The only competing platform is atoms in optical lattices, which benefit from the contribution of a large number of atoms. The fractional instability $6.6 \cdot 10^{-19}$ over an hour was recently demonstrated with strontium atoms[9].

Quantum computing employs quantum bits, called qubits. In contrary to classical computing, it profits from superposition and interference, which leads to parallelism, and the space of states needed to describe the quantum register scales exponentially with the number of qubits. Therefore, some problems can be solved more efficiently by a quantum computer. The quantum supremacy was demonstrated by a 53-qubit superconducting processor[10]. The most famous algorithms include the one for the factorisation of large numbers[11,12] and for the search of unsorted data-bases[13]. From the beginning, the ions seemed like natural representants of the qubits for quantum computing[14] and today two most famous two-qubit ion gates are Cirac-Zoller[15], Mølmer-Sørensen[16]. Ion quantum gates were

demonstrated with infidelity below 10^{-4} in single-qubit operations and approximately one order higher in two-qubit operations[17,18]. The popular platform of superconducting qubits have not reached the gate fidelities[19] of trapped ions quantum processor so far, but in some way is advantageous. For example, the duration of logic operations is much lower for a superconducting qubit, even though it is compared with fast ion gates[20]. The most challenging is the protection of fragile qubit states of ions from decoherence mechanisms. The error correction protocols seem to pave the way to fault-tolerant quantum computing[21].

Besides ions can be utilized in metrology and quantum information processing, they can efficiently store quantum states, which can be exploited in quantum communications. The photons are the best carriers of information, however, signal exponentially decreases upon transmission, which also holds for the ultra-low-loss fibres. The conventional amplifiers or repeaters can not be used for amplification of the quantum states, which effectively limits the transition length or achievable bit rate. The paradigm is to substitute classical amplifiers/repeaters by quantum repeaters and perform the entanglement swap[22,23] between them. It involves quantum memory[24]. At microwave frequency, the memory exceeding ten minutes coherence time[25] was demonstrated. The practical qubit wavelengths should be near the telecom windows for possible conversion to the target transmission window[26]. The entanglement between single photon and single ion was recently demonstrated over 50 km of optical fibre[27].

The presented parameters of ions in diverse applications point out that the trapped ions are one of the best controlled quantum platform. They are also elementary constituents of matter and therefore suitable for studies of the interaction between light and matter at the truly fundamental level.

The requirement for such studies is a sufficiently strong photon-atom interaction[28], which is usually reached by high NA optics[29]. The complementary approach of the coupling between light and matter is based on utilization of high-finesse cavity[30,31], or by increasing the number of interacting particles[32,33]. The response of disorganized atoms grows with their number slowly, but utilizing the directional collective coherent interaction[34] leads to a quadratic increase in the ideal case. The double-slit experiment was implemented with ions[35]. Self-interference of the ion and its mirror image was demonstrated and the two-ion interference through the reflection from the mirror was carried out[36]. The interference of four equidistantly distributed ions in a line was observed[37]. These experiments showed the possibility of utilization collective coherent scattering from a few ions, but is it possible with tens or hundres of ions for practical implementation? The ion thermometry[38] estimates the thermal motional energy of the ions, how much the motion suppresses the interference observability from a higher number of ions? Additional relevant references are discussed in the section 4.1 in detail.

From the essence of the discrete level structure of an atom follows that it can scatter only single photons, which are incompatible with the classical description of electromagnetic waves[B1], therefore the light is truly nonclassical. This is contrary to the general knowledge about radiation from a large number of emitters, which radiate light consisting of classical waves. It has been many times proven by observation of the radiation from different type of sources like sunlight, laser radiation, which can be arbitrarily attenuated[39]. It is considered that the nonclassical character of light emitted by individual single-photon emitters disappears in the macroscopic limit due to the inevitable effects of the surrounding decoherence interaction of sources, light, and detectors. In reality, the situation is a little more complicated and the nonclassicality can be camouflaged even for the emission of two ions[40], when a change of observation direction significantly modulates the $g^{(2)}(0)$ below and over the one. Trapped ions already provided some astonishing observations of nonclassicality. The single $^{138}Ba^{+}$ ion was employed as one of the purest single photons sources[41]. The high-rate source of single photons from $^{40}Ca^{+}$ was published[42] or the deterministic single-photon source employing high-finesse cavity was demonstated[43]. However, what is the limiting number of emitters to lose the possibility of observing the nonclassicality? How large the system has to be? Section 5.1 goes through another substantial references.

The thesis is arranged as follows. The short introduction to the platform of trapped ions is followed by theoretical chapter 2, which underlines content for understanding the concept of the work. It discusses the radio-frequency trap in detail, together with the ion distribution inside one-dimensional Coulombic potential. The $^{40}Ca^{+}$ ion is characterized in terms of employed wavelengths and the decay of target transitions. The derivation of the optical Bloch equations for the atomic three-level system interacting with laser radiation is depicted. The correlation functions as a tool for characterization of light together with nonclassicality of boson statistics are defined. Chapter 3 summarizes step by step vacuum building procedures and characterization of residual hydrogen pressure inside the vacuum chamber. The formation rate of the CaH^{+} molecules is employed. Chapter 4 presents the observation of interference patterns of scattered radiation from large ionic ensembles. The interference curves are authentically fitted by numerical predictions calculated from the position of ions inside the trap. The observation of nonclassical states of emitted light from ionic crystals containing up to more than a thousand of ions is described in chapter 5, which is followed by the conclusion and outlook parts in the last chapter.

Chapter 2

Quantum optics with trapped ions

The chapter describes the principle of trapping charged particles using radio-frequency (RF) electric field. The linear and ring Paul trap are described, their geometry, parameters and stability diagrams are shown. The motion of trapped and cooled ion can be approximated by a quantum harmonic oscillator, which is shortly discussed. The linear ion chains are studied in the quadrupole trap, and the calculation of positions is presented. The $^{40}Ca^{+}$ ion element employed in our setup is discussed, its photoionization, laser cooling and generally the level structure. The chapter introduces the description of light-atom interaction, which is a key part in employing the ions in the quantum optics experiments. The correlation functions are depicted as a tool for the characterization of light. The definition of nonclassical light and sufficient conditions for nonclassicality are discussed.

2.1 Radio-frequency Paul trap

The experiments with single atoms are in high demand because they offer a series of new opportunities. One of the main difficulty is the isolation of the elements from the surrounding world, which causes unwanted decoherence. The isolation needed for purposes of quantum experiments has to be sufficiently long. It can be achieved by trapping of the elements and storing them in a vacuum. Within the work presented in this theses, we employ a linear Paul trap of Innsbruck design for trapping of calcium ions. The principle of trapping in the linear traps is described in the following part.

In order to confine the particle, the repulsive force $F = -\gamma r$ has to be applied on the shifted particle in target direction to restore the wanted position. For a charged particle in an electric field, since the electrostatic force is equal $F = -q\nabla\Phi_E$, it

means the requirement of the 3D potential in the form

$$\Phi(\vec{r}) = \frac{U_{\mathrm{DC}}}{2\tilde{r}^2}\left(\gamma_x r_x^2 + \gamma_y r_y^2 + \gamma_z r_z^2\right), \tag{2.1}$$

where γ_i are positive numbers. The corresponding conservative electric field has to fulfil the Gauss's law, which in the case means to accomplish the Laplace's equation for the potential $\Delta\Phi = 0$ is that

$$\gamma_x + \gamma_y + \gamma_z = 0. \tag{2.2}$$

Therefore, the simple electrostatic trapping potential in all dimensions is not allowed. The potential in eq. (2.1) has to be modified by adding a time-varying electric field so that it takes the form

$$\Phi(\vec{r}, t) = \frac{U_{\mathrm{DC}}}{2\tilde{r}^2} \sum_{i=x,y,z} \gamma_i r_i^2 + \frac{U_{\mathrm{RF}}}{2\tilde{r}^2} \cos(\omega_{\mathrm{RF}} t) \sum_{i=x,y,z} \delta_i r_i^2, \tag{2.3}$$

where ω_{RF} is angular frequency of the RF field. The dynamically driven RF traps are called Paul traps, after Wolfgang Paul, and it allows of trapping in all dimensions[6,44]. Penning traps[45] employ static magnetic field instead of RF electric field to trap charged particles.

The idea behind the RF trap can be simply illustrated on the example of a rotation saddle[46]. The RF field creates the saddle potential, which prevents slipping of the charged particle in one dimension, but supports it in the other, see the Fig. 2.1. Before the particle escapes, the potential will flip with frequency ω_{RF} and after phase π rad it ends at the other extreme, which prevents escaping of the particle

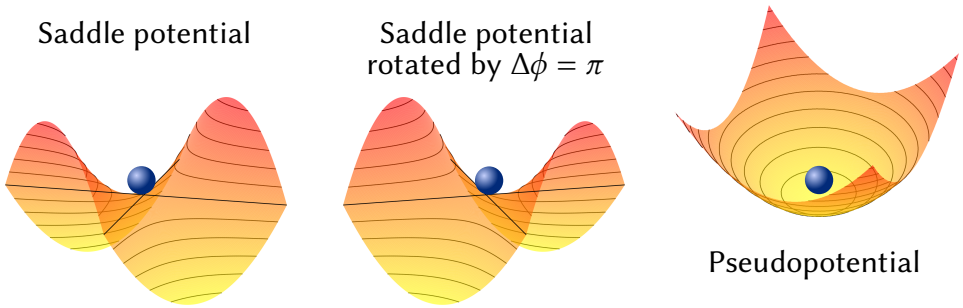

Figure 2.1: The RF trap potential. In the left, the RF potential is shown at defined time, this creates the saddle potential, which protects the particle slipping in one dimension and allows it in the other. The middle picture present same potential rotated by π rad of the RF field, which denies the particle escaping in the other dimension. When the parameters are set correctly, the effective potential called pseudopotential forms minimum in all dimensions, as depicted by the picture in the right.

in the direction previously allowed. Crucial parameters for the dynamical stability are trap geometry, electric charge and mass ration $Z|e|/m$ of the particle, the RF and DC voltage properties.

Specifically, the equation of motion of the particle with mass m and charge $Z|e|$ in the potential eq. (2.3) is

$$\ddot{r}_i = -\frac{Z|e|}{m}\frac{\partial \Phi}{\partial i} = -\frac{Z|e|}{m\tilde{r}^2}(U_{\mathrm{DC}}\gamma_i + U_{\mathrm{RF}}\cos(\omega_{\mathrm{RF}}t)\delta_i)r_i \tag{2.4}$$

and the substitutions

$$\xi = \frac{\omega_{\mathrm{RF}}t}{2}, \quad a_i = \frac{4Z|e|U_{\mathrm{DC}}\gamma_i}{m\tilde{r}^2\omega_{\mathrm{RF}}^2}, \quad q_i = \frac{2Z|e|U_{\mathrm{RF}}\delta_i}{m\tilde{r}^2\omega_{\mathrm{RF}}^2}, \tag{2.5}$$

result in the form of Mathieu differential equation

$$\frac{d^2u_i}{d\xi^2} + (a_i - 2q_i\cos(2\xi))u_i = 0. \tag{2.6}$$

The Mathieu differential equation solution has periodic coefficients and the general form of the stable solutions can be written as[47]

$$u(\xi) = A\sum_{n=-\infty}^{\infty} C_{2n}e^{i(2n+\beta_i)\xi} + B\sum_{n=-\infty}^{\infty} C_{2n}e^{-i(2n+\beta_i)\xi}, \tag{2.7}$$

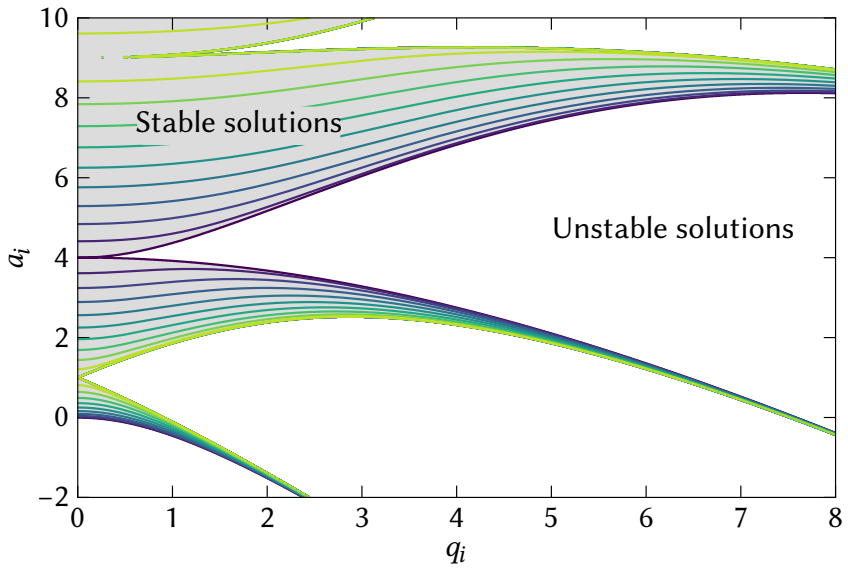

Figure 2.2: Contour plot of the stable solution of the Mathieu equation in standard form given by the eq. (2.6). The shaded surface represents periodic trajectory solutions with a real value of parameter β_i, otherwise the unshaded is purely imaginary and unstable.

where β_i and coefficients C_{2n} are dependent only on the values of a_i and q_i. The stability diagram is shown in the Fig. 2.2, which is contour plot of function β_i. The real β_i indicate stable solution, when the parameter belongs into the interval $\beta_i \in \langle 0, 1\rangle$, the surface is marked as grey. The purely imaginary β_i cover the rest of the graph and means unstable solution of Mathieu equation. The tail of the stable solution containing the point $(a_i, q_i) = (0, 0)$ is named the lowest stability region. The charged particle has to be restricted in all spatial dimensions, the trapping region is secured by superimposing stability regions in particular spatial directions.

2.1.1 Ring and linear Paul trap

The parameters in the eq. (2.3) are given by the geometry of the trap, which will also manifest in the stability diagram. The two most common configurations are the ring RF trap and linear RF trap, see the Fig. 2.3. Another types like multipole traps[48] or microfabricated traps[49,50] will not be discussed here.

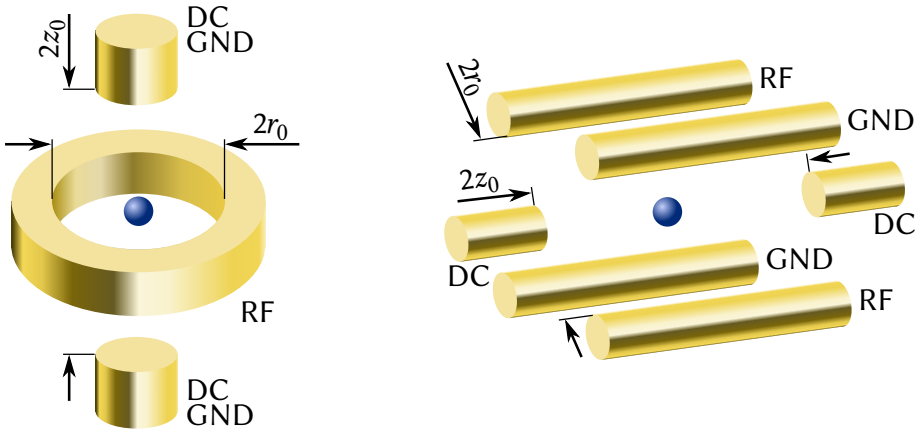

Figure 2.3: Schematic layout of the electrodes in the Paul trap. On the left is sketch of the ring trap with internal diameter $2r_0$ and tips electrodes distant $2z_0$. The RF and DC voltages are applied to ring and tip electrodes. On the right is depicted the linear RF trap, the lowest distance between diagonally positioned quadrupole electrodes is $2r_0$ and the distance of tip electrodes is $2z_0$. The RF voltage drive is applied between pairs of diagonally positioned quadrupole electrodes and the static voltage is connected to tip electrodes.

The ring RF trap is cylindrically symmetric around the z axis and consists of three electrodes. The two tip electrodes are conductively connected, between them and central toroidal electrode the driving voltage $U_{\mathrm{DC}} + U_{\mathrm{RF}} \cos(\omega_{\mathrm{RF}} t)$ is applied. The parameters of potential acquire values[44] $\gamma_x = \gamma_y = -\gamma_z/2 = \delta_x = \delta_y =$

$-\delta_z/2 = 1$ and $\tilde{r}^2 = r_0^2 + 2z_0^2$ that leads to

$$a_x = a_y = -\frac{a_z}{2} = \frac{4Z|e|U_{\mathrm{DC}}}{m(r_0^2 + 2z_0^2)\omega_{\mathrm{RF}}^2}, \tag{2.8}$$

$$q_x = q_y = -\frac{q_z}{2} = \frac{2Z|e|U_{\mathrm{RF}}}{m(r_0^2 + 2z_0^2)\omega_{\mathrm{RF}}^2}. \tag{2.9}$$

The configuration defines Mathieu equations in all directions and the overlap of diagrams in the lowest stability region is plotted in the Fig. 2.4.

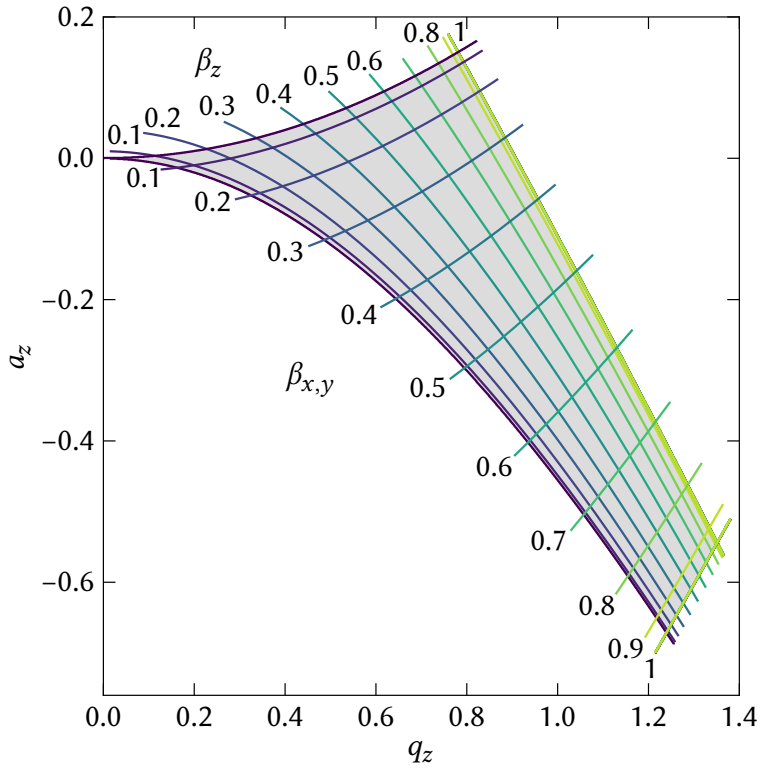

Figure 2.4: The overlap of stability diagrams for ring Paul trap plotted in the lowest stability region.

In the approximation $|a_i| \ll 1$, $q_i^2 \ll 1$, the trajectory of the motional equation can be found in the form

$$r_i(t) \approx r_i^0 \underbrace{\cos\left(\frac{\beta_i \omega_{\mathrm{RF}}}{2} t\right)}_{\text{secular motion}} \underbrace{\left(1 - \frac{q_i}{2}\cos(\omega_{\mathrm{RF}} t)\right)}_{\text{micromotion}}, \tag{2.10}$$

where

$$\beta_i \approx \sqrt{a_i + \frac{q_i^2}{2}}. \tag{2.11}$$

Therefore the motion is given by the superposition of secular motion and micromotion. The amplitude of micromotion depends on RF voltage U_{RF} and the distance of the ion from the trap centre. The deflections are synchronized with RF driving but with a phase delay of π rad. The angular frequency $\omega_{\mathrm{S}i} = \beta_i \omega_{\mathrm{RF}}/2$ of secular motion is lower than angular frequency of RF driving due to small value $\beta_i/2$. The amplitude of micromotion is lower by a factor $q_i/2$, the micromotion can be neglected when the amplitude of micromotion is much lower than the amplitude of secular motion. This can be achieved by laser cooling or by positioning of an ion into the centre of the trap. The ion motion is then given by secular oscillations in pseudopotential Ψ

$$Z|e|\Psi = \frac{m}{2} \sum_{i=x,y,z} \omega_{\mathrm{S}i}^2 r_i^2, \tag{2.12}$$

where $\omega_{\mathrm{S}i}$ represents angular frequency of harmonic oscillator.

The second convenient geometry of the electrodes is quadrupole configuration, which has two tip electrodes and the symetric configuration of four remaining electrodes forming square shape in transverse cut, see the Fig. 2.3. One pair of diagonal electrodes is connected to RF voltage and the other pair serves as ground, on tip electrodes is brought DC voltage.

The parameters of potential are[44] $\delta_x = -\delta_y = 1$, $\delta_z = 0$ and $\tilde{r}^2 = r_0^2$, which results in

$$q_x = -q_y = \frac{2Z|e|U_{\mathrm{RF}}}{m r_0^2 \omega_{\mathrm{RF}}^2}, \quad q_z = 0. \tag{2.13}$$

The DC voltage is usually not connected to the quadrupole electrodes. The example when this is needed, typically corresponds to a requirement of splitting radial frequencies of secular motion. The DC voltages on quadrupole electrodes are close to zero and therefore $a_x = a_y = 0$.

In the lowest-order approximation $|a_i| \ll 1, q_i^2 \ll 1$ the trajectory of the trapped partical is same as for ring trap eq. (2.10) and

$$\beta_x = -\beta_y \approx \frac{q_x}{\sqrt{2}}. \tag{2.14}$$

The overlap of stability diagrams in x and y directions is symmetrical due to the symmetrical configuration of quadrupole electrodes, the Fig. 2.5 shows the lowest stability region.

When the quadrupole configuration has not the tip electrodes the charged particles can go through and in the sensitive operation settings it filters out all particles except one with specific $Z|e|/m$ ratio. Therefore it has been practically employed in mass spectrometry from its discovery till present[51,52]. In linear Paul trap the axial direction is confined by the static voltage on the tip electrodes, which

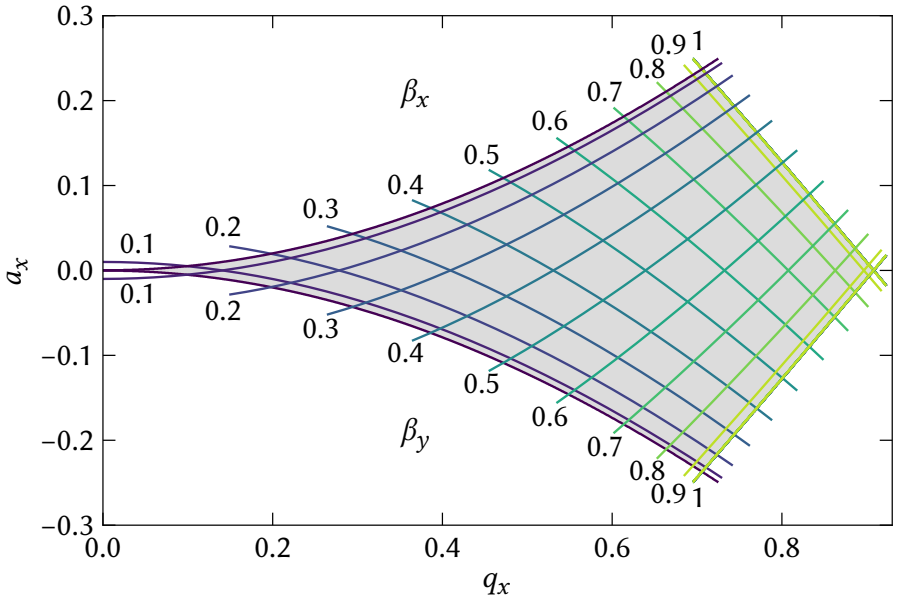

Figure 2.5: The overlap of stability diagrams for quadrupole configuration of electrodes in Paul trap, the graph shows the lowest stability region.

establish harmonic potential

$$\kappa Z|e|U_{\text{tip}} = \frac{m}{2}\omega_z^2 z_0^2, \tag{2.15}$$

the parameter κ stands for geometric factor of the employed trap. The axial secular angular frequency then corresponds to

$$\omega_z = \sqrt{\frac{2\kappa|e|U_{\text{tip}}}{mz_0^2}}, \tag{2.16}$$

which does not depend on the RF field confinement in the x-y plane.

2.1.2 Quantum harmonic oscillator

Since the RF trapping potential is approximately quadratic, the one dimensional Hamiltonian of the ion is given by[B2]

$$\hat{\mathscr{H}}_{\text{QHO}} = \frac{\hat{p}_z^2}{2m} + \frac{m\omega_z^2\hat{z}^2}{2} = \frac{\hat{p}_z^2}{2m} + \frac{k_z\hat{z}^2}{2}, \tag{2.17}$$

which is Hamiltonian of the quantum harmonic oscillator, analogue of the classical harmonic oscillator, where the restoring force $F = -k_z z$ is given by Hooke's law.

The time-independent Schrödinger equation

$$\hat{\mathscr{H}}_{\mathrm{QHO}} |\psi\rangle = E |\psi\rangle \tag{2.18}$$

determines the eigenenergies

$$E_n = \hbar\omega_z \left(n + \frac{1}{2}\right) \tag{2.19}$$

of energy levels, which belong to the particular eigenstates $|\psi_n\rangle$. The wavefunctions in the coordinate basis $\psi(z) = \langle z|\psi\rangle$ take form of Hermite polynomials. The energy spectrum is discrete with equidistantly distributed energy levels, which is appropriate for definition of the ladder operators

$$\begin{aligned} \hat{a} &= \sqrt{\frac{m\omega_z}{2\hbar}} \left(\hat{z} + \frac{i}{m\omega_z}\hat{p}_z\right), \\ \hat{a}^\dagger &= \sqrt{\frac{m\omega_z}{2\hbar}} \left(\hat{z} - \frac{i}{m\omega_z}\hat{p}_z\right). \end{aligned} \tag{2.20}$$

The operators satisfy bosonic commutation relation

$$\left[\hat{a}^\dagger, \hat{a}\right] = -1. \tag{2.21}$$

The action of these operators on the eigenstate $|n\rangle$ corresponds to lowering and raising of the energy by a single quanta

$$\begin{aligned} \hat{a} |n\rangle &= \sqrt{n} |n-1\rangle, \\ \hat{a}^\dagger |n\rangle &= \sqrt{n+1} |n+1\rangle. \end{aligned} \tag{2.22}$$

The number operator $\hat{n}$ is defined as

$$\hat{n} |n\rangle = \hat{a}^\dagger \hat{a} |n\rangle = n |n\rangle \tag{2.23}$$

and the Hamiltonian of the quantum harmonic oscillator, shown in the eq. (2.17), can be then rewritten as

$$\hat{\mathscr{H}}_{\mathrm{QHO}} = \hbar\omega_z \left(\hat{n} + \frac{1}{2}\right). \tag{2.24}$$

The lowest eigenvalue of $\hat{n}$ is 0, the corresponding eigenstate can not be lowered any further

$$\hat{a} |0\rangle = 0 \tag{2.25}$$

and the zero-point energy of this ground state is given by

$$\hat{\mathscr{H}}_{\mathrm{QHO}} |0\rangle = \frac{\hbar\omega_z}{2} |0\rangle. \tag{2.26}$$

2.1.3 Equilibrium positions in linear crystals

The advantage of the linear Paul trap is establishing the pseudopotential only in x-y plane. The static field confinement in the z direction does not cause the micromotion, which is coupled from the radial direction. The axial z trapping potential can be set independently of the radial direction. When the x-y potential is set much tighter[53] than in the z direction, the ions tend to crystallize in linear chain configurations. Then harmonic potential formed by charged tip electrodes and Coulombic repulsion between equally charged N ions results in a system described by the potential[54]

$$V = \sum_{i=1}^{N} \frac{m}{2}\omega_z^2 z_i^2 + \sum_{\substack{i,j=1 \\ i\neq j}}^{N} \frac{Z^2e^2}{8\pi\epsilon_0}\frac{1}{|z_i - z_j|}. \tag{2.27}$$

At the point, we assume sufficiently cool crystal and the minimum energy of the system is found at the equilibrium positions $z_i^{(0)}$ of all ions, which can be found as

$$\left[\frac{\partial V}{\partial z_i}\right]_{z_i = z_i^{(0)}} = 0. \tag{2.28}$$

When we substitute equilibrium position by $u_i = z_i^{(0)}/l$, where the length parameter l is defined by relation

$$l = \left(\frac{Z^2e^2}{4\pi\epsilon_0 m\omega_z^2}\right)^{1/3}, \tag{2.29}$$

then the eq. (2.28) acquires the form of a system of N nonlinear equations for the dimensionless equilibrium position u_i

$$u_i - \sum_{j=1}^{i-1}\frac{1}{(u_i - u_j)^2} + \sum_{j=i+1}^{N}\frac{1}{(u_i - u_j)^2} = 0, \quad \text{for } i = 1, 2 \ldots N. \tag{2.30}$$

The system can be solved analytically for $N = 2$, $N = 3$, otherwise the solution has to be found numerically. The positions of the two and three ions around the trap centre are given by

$$N = 2: \quad z_1 = -\left(\frac{1}{2}\right)^{2/3} l, \quad z_2 = \left(\frac{1}{2}\right)^{2/3} l, \tag{2.31}$$

$$N = 3: \quad z_1 = -\left(\frac{5}{4}\right)^{1/3} l, \quad z_2 = 0, \quad z_3 = \left(\frac{5}{4}\right)^{1/3} l. \tag{2.32}$$

The unknown relation of angular frequency ω_z between the voltage on tip electrodes U_{tip} is the last step for the practical implementation. To find the axial centre of mass (COM) motion frequency we employed the single trapped ion and for set U_{tip} voltage we tuned weak harmonic frequency on one of the axial electrodes and observed when the ions get into resonance on the camera. We performed a series of the measurements and fitted the data by theoretical expression in the eq. (2.16), see in the Fig. 2.6. Note the vertical axis is plotted as frequency f_z, but the mentioned equations include angular frequency $\omega_z = 2\pi f_z$. The wide axial potential at $U_{\text{tip}} = 10\,\text{V}$ corresponds $f_z = 103.7\,\text{kHz}$ in our trap. When the radial potential is much stronger the distance for two $^{40}\text{Ca}^+$ ions inside the trap is $d = 25.40\,\mu\text{m}$, the distributions of N ions at the conditions are plotted in the Fig. 2.7.

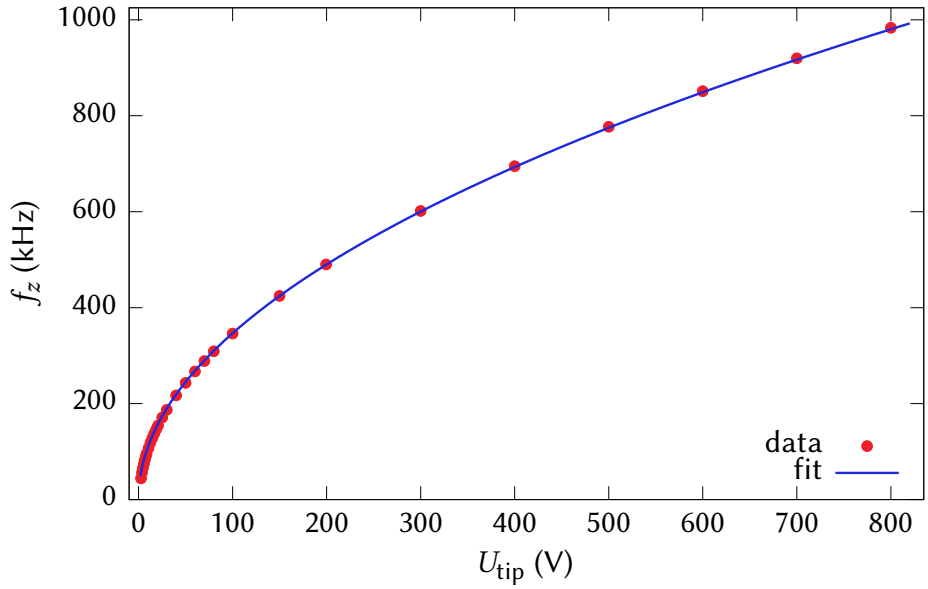

Figure 2.6: The axial frequency of single trapped $^{40}\text{Ca}^+$ ion as a function of the tip voltage U_{tip} in our setup. The red dots represent measured data, and the solid blue line is fit.

Even though the ions are crystalized to form a string they still experience thermal secular motion. The crystal containing N ions exhibit $3N$ normal oscillatory modes, it corresponds N in each spatial coordinate. Each of the motional modes can be described as an oscillatory motion $q_i(t)$ around the equilibrium position

$$z_i(t) = z_i^{(0)} + q_i(t). \tag{2.33}$$

The Fig. 2.8 depicts the situation for three ions positioned in a linear string. The oscillation angular frequency of axial COM mode ω_z is the same as for a single ion

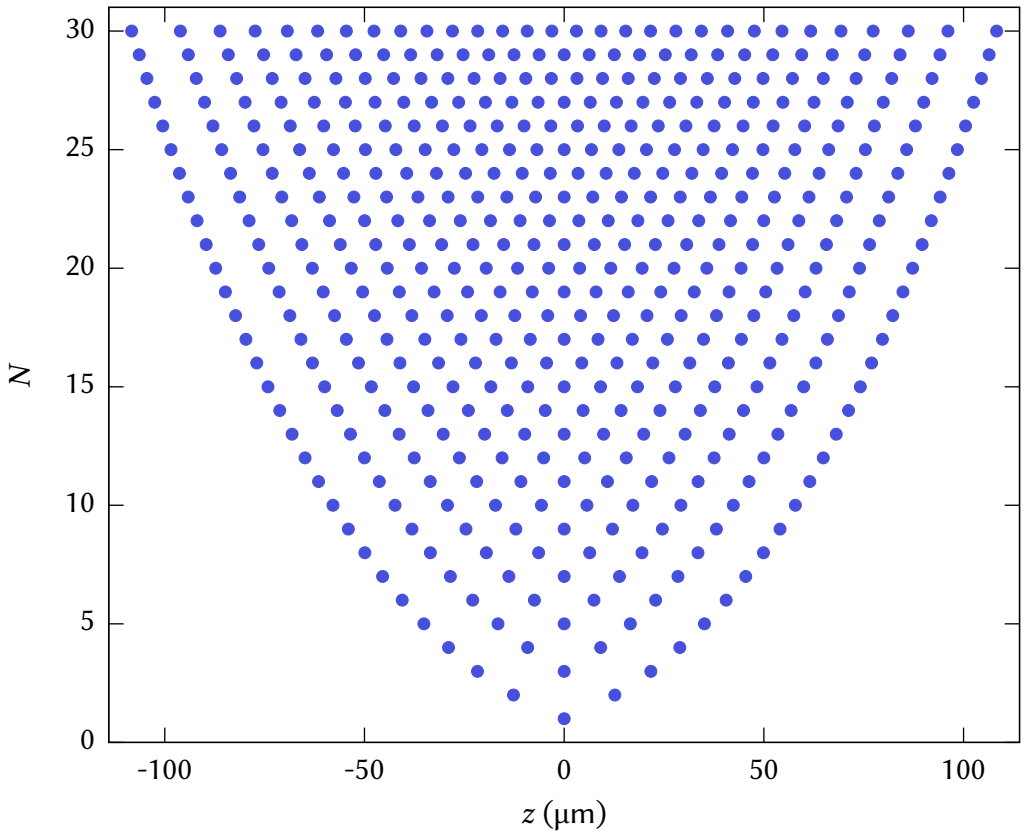

Figure 2.7: The calculated distributions of N $^{40}Ca^{+}$ ions inside our trap at $U_{tip} = 10\,V$ and for radial potential much tighter[53] than the axial.

occupying the trap. The angular frequency of the first higher axial mode called stretch or breathing[54] is equal to the value of $\sqrt{3}\omega_z$. The axial mode called egyptian has the highest angular frequency $\sqrt{29/5}\omega_z$. When we assume the same energy for all axial modes, then the amplitude should be smaller for higher modes due to higher frequency, but excitation of each mode is highly dependent on the practical trapping settings and laser excitation parameters. The oscillatory modes are important as the connection between ions when they establish something like a communication bus for two and more quantum gates protocols. In the radial direction, the higher modes are called rocking and zig zag.

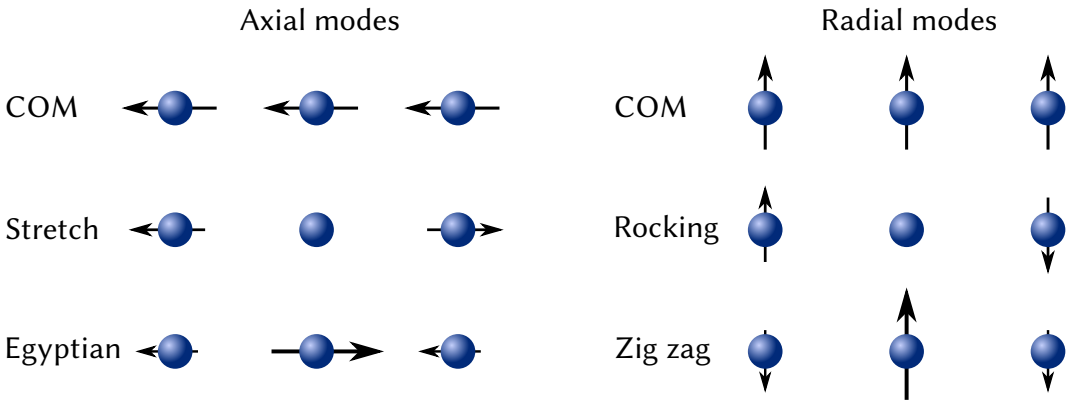

Figure 2.8: Illustration of secular motion in the axial and the radial directions for a three ion string.

2.2 Calcium ion

In our experiments, we chose to employ $^{40}Ca^{+}$ ions as a promising element in a field of quantum optics with all wavelengths in a visible spectrum. Calcium is a chemical element with atomic number 20 and belongs to the group of alkaline earth metal. It is reactive and tends to oxidize when exposed to the air. The calcium atom is heavily abundant chemical element on the Earth and its standard atomic weight[55] is $A_{r,std}(Ca) = 40.078$. The main isotopes abundances are listed in the Tab. 2.1. Note that we have employed merely $^{40}Ca^{+}$ ion in our experiments.

Its properties are similar to other elements from second column of the periodic table, the electron structure of $^{40}Ca^{+}$ ion is the most interesting for ion trappers. The most outer S orbital of neutral atom is fully occupied, which means that after single-electron photoionization the valence orbital contains a single electron. This makes the ion look like a hydrogen atom partially, still, the level structure is de-

Table 2.1: Overview of the calcium isotopes with natural abundance and relative atomic masses[55].

Isotope	Natural abundance (%)	Relative atomic mass (u)
^{40}Ca	96.941	39.9625912
^{42}Ca	0.647	41.9586183
^{43}Ca	0.135	42.9587668
^{44}Ca	2.086	43.9554811
^{46}Ca	0.004	45.9536927
^{48}Ca	0.187	47.952533

formed due to inner electrons in lower orbitals. To photoionize the neutral ^{40}Ca we employ the wavelength around $\lambda_{422} = 422.79\,\text{nm}$, which excites the electron to the upper P orbital and then the second laser with $\lambda < 389\,\text{nm}$ kicks the electron to continuum, within a two-photon ionization process[56,57]. The simplified level structure[54] of the resulting ionized atom corresponding to $^{40}Ca^{+}$ is depicted in the Fig. 2.9.

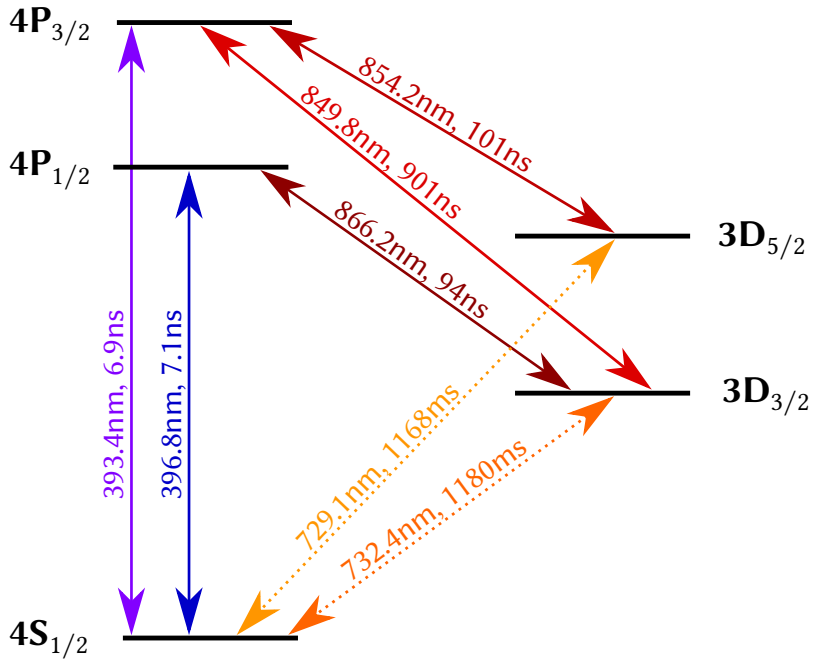

Figure 2.9: Simplified energy level scheme of the $^{40}Ca^{+}$ ion. The dipole and quadrupole transitions are marked by the solid and dotted arrows, respectively. The transition labels contain corresponding wavelengths and the inverse of transition rates.

For the valence electron, the lowest level is the S orbital, which is, therefore the ground state. The short-lived upper levels are constituted by the fine structure of P orbital, namely $4P_{1/2}$ and $4P_{3/2}$, with inverses of transition rates into the ground state $4S_{1/2}$ are 7.1 ns and 6.9 ns, respectively[58].

The metastable D orbital is long-lived level with $3D_{3/2}$ and $3D_{5/2}$ fine structure components. The quadrupole transition $4S_{1/2} \leftrightarrow 3D_{5/2}$ is usually employed as a qubit with the lifetime of the upper level of 1168 ms[59]. The qubit transition was subject of precise spectroscopic studies[60]. The 854 nm laser is then used as the reshuffling laser for the qubit upper level.

For Doppler cooling, we employed a 397 nm laser red detuned from the $4S_{1/2} \leftrightarrow 4P_{1/2}$ transition. The branching fraction of the decay for the $4P_{1/2}$ state into $4S_{1/2}$ and $3D_{3/2}$ are equal to probabilities 0.936 and 0.064, respectively[61]. The 866 nm

laser is needed for depopulation of the metastable $3D_{3/2}$ manifold. Since the $^{40}Ca^{+}$ ion has the nuclear spin equal to zero, there is no hyperfine splitting. In the experiments presented within this thesis, we apply a static magnetic field in the range of 6-12 Gauss in order to define the dipole transitions orientation in the experiments.

2.3 Atom-field interaction

The knowledge of light interaction with the ions is relevant in our experiments. We employ the laser light for detecting the ions in our trap, for cooling them, determining and manipulating their quantum state. The laser excitation parameters, which are important in calculations of our experiments, can be obtained from the numerical simulation of the interaction described by semi-classical theory. The Hamiltonian of an atom interacting with the radiation can be written in the way[62]

$$\hat{\mathscr{H}} = \hat{\mathscr{H}}_{\mathrm{A}} + \hat{\mathscr{H}}_{\mathrm{E}} + \hat{\mathscr{H}}_{\mathrm{I}}, \tag{2.34}$$

where the parts on the right side equation represent Hamiltonian of atom $\hat{\mathscr{H}}_{\mathrm{A}}$, field $\hat{\mathscr{H}}_{\mathrm{E}}$ and interaction Hamiltonian between them $\hat{\mathscr{H}}_{\mathrm{I}}$. The Hamiltonian with discrete energy levels corresponding to electronic states is given by

$$\hat{\mathscr{H}}_{\mathrm{A}} |i\rangle = \hbar\omega_i |i\rangle , \tag{2.35}$$

where $|i\rangle$ stands for eigenstates of the employed atomic levels, in our case a lambda scheme consisting of $i = 1, 2, 3$. Here, the indexes represent $^{40}Ca^{+}$ ground level $4S_{1/2}$, the excited level $4P_{1/2}$ and the metastable level $3D_{3/2}$. The ω_i is the electron transition frequency of the i^{th} level. The atomic Hamiltonian written as matrix in orthonormal basis (1,0,0), (0,1,0), (0,0,1) is

$$\mathscr{H}_{\mathrm{A}} = \hbar \begin{pmatrix} \omega_1 & 0 & 0 \\ 0 & \omega_2 & 0 \\ 0 & 0 & \omega_3 \end{pmatrix}. \tag{2.36}$$

When we choose the rotating frame with the state $|2\rangle$ the Hamiltonian simplifies to

$$\mathscr{H}_{\mathrm{A}} = \hbar \begin{pmatrix} \omega_1 - \omega_2 & 0 & 0 \\ 0 & 0 & 0 \\ 0 & 0 & \omega_3 - \omega_2 \end{pmatrix}. \tag{2.37}$$

Two laser fields drive the transitions $|1\rangle \leftrightarrow |2\rangle$ and $|3\rangle \leftrightarrow |2\rangle$, then the classical monochromatic laser field for the transition $|1\rangle \leftrightarrow |2\rangle$ is given by

$$\vec{E}'_{12}(t) = \vec{\epsilon}_{12} E_{12} e^{-i\omega_{12}t}, \tag{2.38}$$

where ω_{12} marks the angular frequency, E_{12} amplitude and $\vec{\epsilon_{12}}$ stands for polarization vector. The field $\vec{E'_{32}}(t)$ is defined analogously. In dipole approximation is assumed that the laser light interacts merely with the electric dipole moment of the ion and the higher-order moments are neglected. The interaction Hamiltonian is then expressed as

$$\hat{\mathscr{H}}_{\mathrm{I}} = -\vec{D} \cdot \vec{E'}, \tag{2.39}$$

where $\vec{D}$ represents the atomic dipole. In this approximation, the quadrupole transition $|1\rangle \leftrightarrow |3\rangle$ is forbidden and accordingly the level $|3\rangle$ is assumed to be stable. The matrix of interaction Hamiltonian can be written as

$$\mathscr{H}_{\mathrm{I}} = \hbar \begin{pmatrix} 0 & \frac{\Omega_{12}}{2} e^{i\omega_{12}t} & 0 \\ \frac{\Omega_{12}}{2} e^{-i\omega_{12}t} & 0 & \frac{\Omega_{32}}{2} e^{-i\omega_{32}t} \\ 0 & \frac{\Omega_{32}}{2} e^{i\omega_{32}t} & 0 \end{pmatrix}, \tag{2.40}$$

where

$$\hbar\Omega_{12} = \vec{\epsilon}_{12} \cdot \vec{D}_{12} \cdot E_{12} \tag{2.41}$$

and $\hbar\Omega_{32}$ analogously. The quantity Ω_{12} is Rabi frequency, which characterizes the population oscillation speed of the target transition in the field. The coupling strength can be expressed using the saturation parameter S_{12} by relation

$$S_{12} = \frac{\Omega_{12}}{\Gamma_{12}}, \tag{2.42}$$

where Γ_{12} is the decay rate. The complete semiclassical Hamiltonian is given by

$$\mathscr{H} = \hbar \begin{pmatrix} \omega_1 - \omega_2 & \frac{\Omega_{12}}{2} e^{i\omega_{12}t} & 0 \\ \frac{\Omega_{12}}{2} e^{-i\omega_{12}t} & 0 & \frac{\Omega_{32}}{2} e^{-i\omega_{32}t} \\ 0 & \frac{\Omega_{32}}{2} e^{i\omega_{32}t} & \omega_3 - \omega_2 \end{pmatrix}. \tag{2.43}$$

The unitary evolution

$$\mathscr{U} = \begin{pmatrix} e^{-i\omega_{12}t} & 0 & 0 \\ 0 & 0 & 0 \\ 0 & 0 & e^{-i\omega_{32}t} \end{pmatrix} \tag{2.44}$$

transforms the Hamiltonian into the rotating frame at the laser frequencies and the final form of Hamiltonian of two excitation laser beams coupled with a three-level atomic system simplifies to

$$\mathscr{H}' = \hbar \begin{pmatrix} \omega_{12} + \omega_1 - \omega_2 & \frac{\Omega_{12}}{2} & 0 \\ \frac{\Omega_{12}}{2} & 0 & \frac{\Omega_{32}}{2} \\ 0 & \frac{\Omega_{32}}{2} & \omega_{32} + \omega_3 - \omega_2 \end{pmatrix}. \tag{2.45}$$

2.3.1 Density operator formalism

The description above did not include spontaneous decay from state $|2\rangle$ or other decoherence mechanisms. For the description of the system in a mixed state, the density operator formalism is used. In the employed basis the operator reads

$$\hat{\rho} = \sum_{i,j=1,2,3} \rho_{i,j} |i\rangle \langle j| . \tag{2.46}$$

Since the diagonal elements correspond to probabilities of finding the ion in the state, the trace has to fulfil $Tr(\hat{\rho}) = 1$. The quantum Master equation is used to deal with the dynamics of the system

$$\frac{d\hat{\rho}}{dt} = -\frac{i}{\hbar}\left[\hat{\mathscr{H}}, \hat{\rho}\right] + \hat{\mathscr{L}}(\hat{\rho}), \tag{2.47}$$

where dissipative processes are described by the term

$$\hat{\mathscr{L}}(\hat{\rho}) = -\frac{1}{2}\sum_{m}\left(\hat{C}_m^{\dagger}\hat{C}_m\hat{\rho} + \hat{\rho}\hat{C}_m^{\dagger}\hat{C}_m - 2\hat{C}_m\hat{\rho}\hat{C}_m^{\dagger}\right). \tag{2.48}$$

The decay processes from level $|2\rangle$ are included as

$$\hat{C}_{21} = \sqrt{\Gamma_{21}} |1\rangle \langle 2| , \quad \hat{C}_{23} = \sqrt{\Gamma_{23}} |3\rangle \langle 2| . \tag{2.49}$$

The finite linewidths δ_{12}, δ_{32} of laser radiation are covered by

$$\hat{C}_{12} = \sqrt{2\delta_{12}} |1\rangle \langle 1| , \quad \hat{C}_{32} = \sqrt{2\delta_{32}} |3\rangle \langle 3| . \tag{2.50}$$

2.3.2 Bloch equations

The quantum Liouville eq. (2.47) for linearly dependent elements of $\hat{\rho}$ can be re-written into the form

$$\frac{d\vec{\rho}_i}{dt} = \sum_j \mathscr{M}_{ij}\vec{\rho}_j, \tag{2.51}$$

where

$$\vec{\rho} = (\rho_{11}, \rho_{12}, \ldots, \rho_{32}, \rho_{33}). \tag{2.52}$$

This system of linear equations is called optical Bloch equations. From the initial condition $\vec{\rho}(0)$ the solution at time t can be calculated by

$$\vec{\rho}(t) = e^{\mathscr{M}t}\vec{\rho}(0). \tag{2.53}$$

The normalization of ρ was established at the beginning and the sum of diagonal elements, respectively occupation probabilities remain normalized

$$\sum_i \rho_{ii} = 1 \quad \forall t. \tag{2.54}$$

In general, the linear system of the Bloch equations has to be solved numerically to achieve the steady-state solution characterized by $\vec{\rho}(\infty)$ =const., where $\dot{\vec{\rho}} = 0$. The three-level system is not a convenient model to use. For our purposes, it is often necessary to include more levels, as a weak static magnetic field lifts the degeneracy of states. In practical, it means to employ the eight-level system for our $^{40}Ca^{+}$ ion.

2.4 Degree of coherence

The radiation in the cavity is described by the same Hamiltonian as already discussed quantum harmonic oscillator. In order to quantize the light, the bosonic operators $\hat{a}^{\dagger}$, $\hat{a}$ are used and the quantized electric field operator takes the form[B3]

$$\hat{E}(\vec{r},t) = \hat{E}^{(+)}(\vec{r},t) + \hat{E}^{(-)}(\vec{r},t) = \sum_{\mathbf{k}} \epsilon_{\mathbf{k}} \mathscr{E}_{\mathbf{k}} \left(\hat{a}_{\mathbf{k}} e^{-i(\omega_{\mathbf{k}} t - \mathbf{k}\cdot\mathbf{r})} + \hat{a}^{\dagger}_{\mathbf{k}} e^{i(\omega_{\mathbf{k}} t - \mathbf{k}\cdot\mathbf{r})} \right), \tag{2.55}$$

where the annihilation operators belong to $\hat{E}^{(+)}(\vec{r},t)$ and the creation operators belongs to the adjoint part $\hat{E}^{(-)}(\vec{r},t)$.

2.4.1 Correlation functions

The correlation functions represent an essential tool for the characterization of light. The order of correlation function corresponds to the order of moment of the function. The most relevant orders are the first two. The form of the normalized first-order correlation function is

$$g^{(1)}(\vec{r}_1,t_1,\vec{r}_2,t_2) = \frac{\left\langle \hat{E}^{(-)}(\vec{r}_1,t_1)\hat{E}^{(+)}(\vec{r}_2,t_2) \right\rangle}{\left[\left\langle |\hat{E}(\vec{r}_1,t_1)|^2 \right\rangle \left\langle |\hat{E}(\vec{r}_2,t_2)|^2 \right\rangle \right]^{1/2}}. \tag{2.56}$$

The $g^{(1)}$ is function of electric field amplitude and characterizes the coherence of light, or in another way, the ability to interfere. It can be employed to quantify the temporal coherence

$$g^{(1)}(t,t+\tau) = g^{(1)}(\tau) = \frac{\left\langle \hat{E}^{(-)}(t)\hat{E}^{(+)}(t+\tau) \right\rangle}{\left\langle \hat{E}^{(-)}(t)\hat{E}^{(+)}(t) \right\rangle}. \tag{2.57}$$

The function is usually employed in measurements with Michelson and Mach-Zehnder interferometer, where the input light is split into two waves with the same amplitudes. The visibility of the interference fringes is then equal to $|g^{(1)}| \in \langle 0, 1 \rangle$, where zero represents an incoherent field, one corresponds to fully coherent light, and other values indicate partially coherent light. The $g^{(2)}$ defined as

$$g^{(2)}(\tau) = \frac{\left\langle \hat{E}^{(-)}(t)\hat{E}^{(-)}(t+\tau)\hat{E}^{(+)}(t+\tau)\hat{E}^{(+)}(t) \right\rangle}{\left\langle \hat{E}^{(-)}(t)\hat{E}^{(+)}(t) \right\rangle^2}, \tag{2.58}$$

characterizes the photon statistics, and it is the correlation function of intensities, therefore it can be rewritten to the form

$$g^{(2)}(\tau) = \frac{\left\langle \hat{I}(t)\hat{I}(t+\tau) \right\rangle}{\left\langle \hat{I}(t) \right\rangle^2}. \tag{2.59}$$

If the operators in the eq. (2.59) are replaced by classical intensities, the correlation function for classical states of light has to fulfil the Cauchy-Schwarz inequality, which gives[B4]

$$\begin{aligned} g^{(2)}(\tau) &\leq g^{(2)}(0), \\ 1 &\leq g^{(2)}(0). \end{aligned} \tag{2.60}$$

However, the quantum theory allows for violation of both relations. The correlation function gives a threshold value of $g^{(2)}(0) = 1$ for coherent state $|\alpha\rangle$ corresponding to idealized laser light. Another type of classical light is thermal light, which exhibits the correlation in temporal photon distribution. The states of light with $g^{(2)}(0) < 1$ are nonclassical with the most recognized example corresponding to photon number states.

The $g^{(2)}(\tau)$ function defined in the eq. (2.59) practically means to measure the correlation of time-shifted intensities. The Hanbury Brown and Twiss (HBT) configuration provides convenient way to do it, see the Fig. 2.10. It illustrates the phenomenon of an atom being the single-photon source[63] and the indivisibility of the single photon on a beam splitter[64]. The single photon is either reflected or transmitted on the non-polarizing beam splitter 50:50 (BS) and detected on APD_2 or APD_1, respectively. The coincidences are processed in the correlation unit. The described example presents the measurement of nonclassical light. The single photon can not be detected on both detectors, therefore there is no correlation for the zero delay between APDs and $g^{(2)}(0) = 0$ in the ideal case. Note, the atoms can emit more photons[65] at the nearly same time in the cascade processes. All atom-like

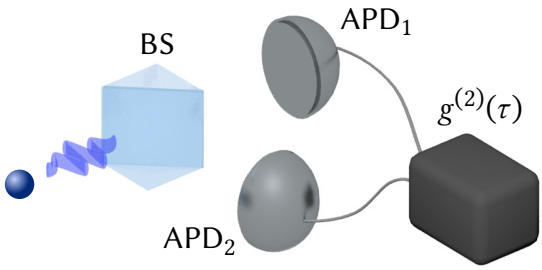

Figure 2.10: The Hanbury Brown and Twiss configuration. The single photon is emitted by the single ion and then is either reflected into APD_2 or transmitted into APD_1 by a beam splitter. The event is recorded and processed in the correlation unit.

emitters were gifted by this intrinsic feature of emission of nonclassical light. The population decay and excitation in the atom are accompanied by emission and absorption of photons, respectively. The correlation functions can be then rewritten in terms of the rising $\hat{\sigma}_+ = |e\rangle\langle g|$ and the lowering $\hat{\sigma}_- = |g\rangle\langle e|$ operators as

$$g^{(1)}(\tau) = \frac{\left\langle \hat{\sigma}_+(t)\hat{\sigma}_-(t+\tau)\right\rangle}{\left\langle \hat{\sigma}_+(t)\hat{\sigma}_-(t)\right\rangle} \tag{2.61}$$

and

$$g^{(2)}(\tau) = \frac{\left\langle \hat{\sigma}_+(t)\hat{\sigma}_+(t+\tau)\hat{\sigma}_-(t+\tau)\hat{\sigma}_-(t)\right\rangle}{\left\langle \hat{\sigma}_+(t)\hat{\sigma}_-(t)\right\rangle^2}. \tag{2.62}$$

The atomic resonance fluorescence is dependent on the laser parameters in continual driving. The system is described by Bloch equations, which is a system of linear equations. The corresponding temporal correlation functions obey same equations. This is known as the quantum regression theorem[B5,B6]. Therefore the correlation functions can be directly obtained from the density matrix of the system.

2.4.2 Nonclassical light

The density matrix of any state of light can be written as

$$\hat{\rho} = \int P(\alpha)\,|\alpha\rangle\langle\alpha|\,d^2\alpha, \tag{2.63}$$

where $|\alpha\rangle$ is a coherent state, defined as the eigenvector of the annihilation operator

$$\hat{a}\,|\alpha\rangle = \alpha\,|\alpha\rangle\,. \tag{2.64}$$

The $P(\alpha)$ is a quasi-probability distribution[B6]. When $P(\alpha)$ is not a probability density function, it means, it is more singular than a Dirac delta function or is negative at any point, then the state is nonclassical. In other words, the nonclassical state can not be written as a statistical mixture of coherent states.

One can differentiate between two forms of nonclassicality depending on the type of measurement employed for its detection. The first type of observation employes the measurement of continuous variables and allows for measuring high intensities of light. A representative example of the nonclassical state sensed typically in this way, corresponds to state with a quadrature squeezing. Complementary, the second type of observation utilizes the discrete variables. For example, the Fock states can be estimated from the photon number distribution measurements. This thesis studies only the second form of detection of nonclassicality. In particular, the state of light is determined merely from temporal photon distribution.

The theoretical criterion of nonclassicality can not be directly measured, therefore the sufficient conditions are used in real experiments. The inequality $g^{(2)}(0) < 1$ is impractical due to the whole photon statistics has to be known. The α parameter directly employs measurable quantities of HBT arrangement, and it allows us to formulate a condition used for detection of nonclassicality. When the α is lower than one[64]

$$1 > \alpha = \frac{p_c}{p_1 p_2}, \tag{2.65}$$

the state is nonclassical. The values p_1, p_2 represent probabilities of single clicks of detector 1, 2 and p_c is the probability of coincidence click of both detectors in the HBT detection arrangement as depicted in the Fig. 2.10.

The alternative sufficient condition of nonclassicality[1] can be defined in terms of the probability P_0 of a no-click of the selected detector and a no-click of both detectors P_{00} in the HBT arrangement. When the distance d obeys the inequality

$$d = P_0 - \sqrt{P_{00}} > 0, \tag{2.66}$$

then the state is nonclassical. This criterion was derived ab initio without any assumptions about the detected light state. The criterion can be used in imbalanced case of HBT arrangement, this is covered in chapter 5 together with the practical implementation.

Chapter 3

Experimental apparatus assembly

The chapter is dedicated to the vacuum affair of our experimental apparatus and is divided into two main sections. The first section reviews the vacuum assembly of a new $^{40}Ca^{+}$ room temperature trapping apparatus and the key steps, like cleaning, baking, pumping are described in detail. The second part is focused on the quantification of the residual background gas, specifically hydrogen, by analysis of the $^{40}CaH^{+}$ molecule formation rate. Summary of the work is published in the article [A1].

3.1 Introduction

As it was already mentioned, the necessary condition for quantum optical experiments with single atoms or molecules is to achieve sufficiently long trapping lifetimes. The trapping of charged particles has been described in the previous chapter 2. This chapter will discuss the isolation of trapped particles from the surrounding space by storing them in a vacuum, which has a direct impact on the lifetime of the trapped system. The lifetime of the trapped ensemble is usually limited by collisions with surrounding freely moving particles. The average distance of particle travel between two collisions is called the mean free path λ. Considering an air at the standard condition[66], the mean free path can be approximately expressed by a function of pressure P_{air} as

$$\lambda_{\text{air}} = \frac{6.5 \cdot 10^{-3}}{P_{\text{air}}}. \tag{3.1}$$

This results in $\lambda_{\text{air}} = 65\,\text{nm}$ at atmospheric pressure $P_{\text{air}} \approx 10^5\,\text{Pa} = 10^3\,\text{mBar}$. The value is in good agreement with the precise estimation[67], but it's indeed too low for sufficiently long lifetimes of the trapped specimen with the mass corresponding

to a single or a few atoms. In a room temperature vacuum apparatus, the ultra-high vacuum (UHV) levels of pressure $10^{-9} - 10^{-12}$ mBar can be achieved, which corresponds to a range of mean free path $\lambda_{\text{air}} = 6.5 \cdot (10^4 - 10^7)$ m satisfactory for the majority of the quantum optics experiments. Therefore it became the target vacuum pressure for trapping single atomic ions or small ion crystals. Assuming the collision probability grows linearly with the number of trapped particles in the crystal, the scalable system needs even lower pressure of vacuum for their practical usability. Otherwise, the vacuum pressure can limit the performance of the experimental setup, or even worse, impose requirements for frequent ion reloading in the most advanced branches of ion trapping applications, which involve a scalable system containing tens to hundreds of ions[A3,68–74].

A further step of enhancing the vacuum pressure can be done by cryogenically cooled setup[75,76]. Lowering temperature causes a decrease of outgassing, therefore surfaces inside the vacuum chamber work as entrapment pumps, which leads to a decrease of vacuum pressure and opens the possibility of reaching the vacuum pressures beyond UHV level. Moreover, the residual gases have reduced kinetic energy due to the use of cryogenic vacuum setup. Besides that, another important advantage observed in cryogenic ion trapping setups corresponds to the reduced heating raters[77,78], which typically depend on the trap material, surface and other parameters. The heating rates reduction was observed by two to three orders of magnitude during the transition from the room-temperature operation to cryo regime[50,79].

Background gases collisions with trapped ions can manifest in several observable phenomena. They can lead to chemical reactions[80], change of electron population inside the atom[76,81], thermalization of the crystal or even direct ejection from the trapping potential. Practically, the thermalization of ion crystal leads to decrease of the fidelity in quantum computing and quantum simulations. Collisional heating also affects the frequency of atomic qubits by two different principles: the collisions randomize the phase of the atomic state and secondly, it changes the motional state of the oscillator, which causes a time dilatation shift by second-order Doppler effect[70,82]. The study of chemical reactions in Paul trap became very promising, the main advantage of quadrupole and multipole traps is the possibility to directly measure the mass of components of the chemical reactions. For all other types of experiments, the chemical reactions are unwanted and with that arises a problem, how to deal with the products of chemical reactions. There are basically two ways: reload the crystal or dissociate the products.

Well-assembled UHV setup has mostly the highest partial pressure of hydrogen due to its large concentration in stainless steel and high diffusion rate[83]. Therefore, a study of reactions of hydrogen with atomic ion species seems to be logical and various situations were theoretically and experimentally studied. Many of these

reactions are photochemical, it means they are laser-induced, therefore can be tuned by laser parameters. Experimentally has been demonstrated the processes of producing molecules BeH^+ by the reaction of neutral freely moving hydrogen and trapped cooled ions of $^9Be^+$[84], similarly has been observed reactions with other species as with Yb^+[85], also the dissociation[86], Mg^+[87,88] and demonstration of laser cooling them directly or sympathetically[89,90]. Our setup is equipped only by a source of Calcium atoms and thus the most relevant for us are the reaction products CaH^+. It has been shown that CaH^+ molecules are astrophysically important as it was detected in the stars[91], in the Sun and also play an important role in molecular clouds of the interstellar medium[92]. These ascertainments raise the relevance of the molecule and stimulated a series of experiments. The reaction rate of producing CaH^+ was estimated[93,94], conditional dissociation[94] of CaH^+ was demonstrated in Paul trap, rovibrational states were studied both theoretically[95] or experimentally[92,96] and also coherent manipulation of pure quantum states of a single CaH^+ was demonstrated[97].

3.2 Vacuum construction

The section describes our build-up procedure of vacuum setup in detail. It contains the employed vacuum pumps, choice of materials, trap description, cleaning procedures, and three-stage bake process.

3.2.1 Vacuum pumps

To reach UHV pressure, we employed four different vacuum pumps. From outside, the vacuum chamber was pumped by a turbomolecular pump and as its pre-pump, we used a Roots pump. These two pumps were delivered as a standard two-stage vacuum system (HiCube 80 Pro/ACP 15, Pfeiffer Vacuum).

Inside the vacuum chamber, we used two entrapment pumps. The farthest pump from the trap is a combination of an ion pump and non-evaporative getter (NEG) pump (NEXTorr® D 100-5, SAES Getters) and the second one is a pure NEG pump (CapaciTorr® D 50, SAES Getters) positioned in the proximity of the ion trapping region at 55 mm distance, see the Fig. 3.1. The estimated pumped volume of the vacuum chamber is approximately 1.6 litres.

3.2.2 Vacuum chamber

Below 10^{-6} mBar pressure levels, outgassing of materials plays an important role and can compensate the amount of pumped gas. Therefore low-outgassing UHV

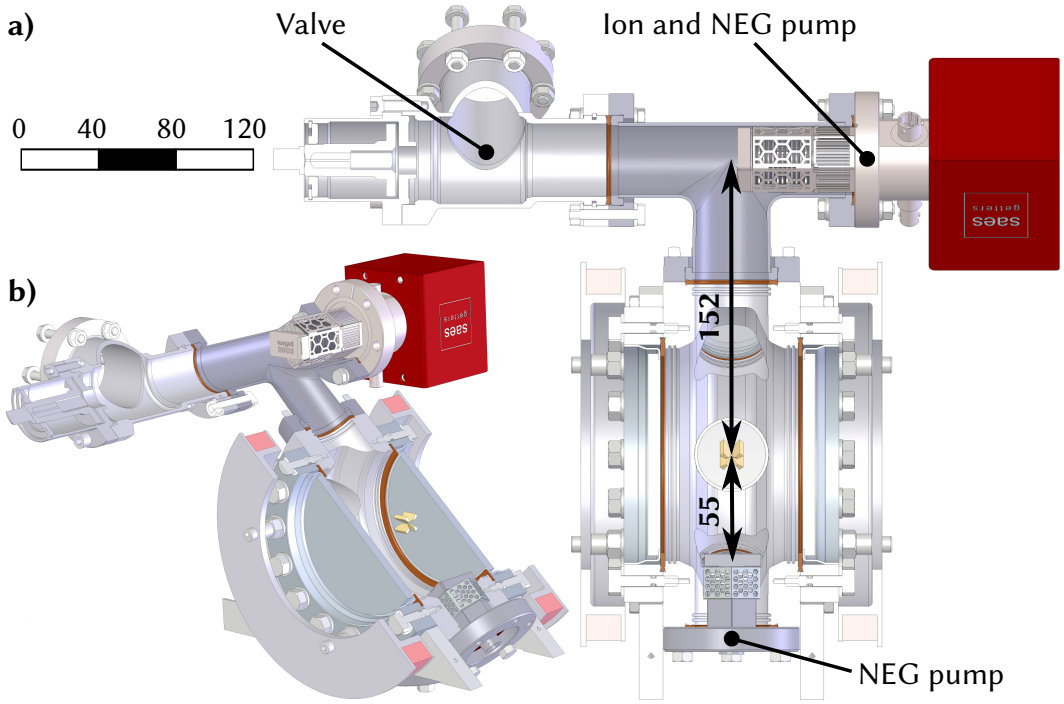

Figure 3.1: Visualization of cut-through vacuum chamber and four blades of quadrupole trap. Trap holder and its other parts are not depicted. a) The side-top view with spatial scale in millimetres. b) The rotated 3D perspective to illustrate the spatial layout of the vacuum chamber.

compatible materials were chosen. The most represented compound is stainless steel, which serves also as the construction element of the setup. The non-magnetic stainless steels SS 316 LN and SS 304 were used to minimize unknown magnetic field gradients across the trapping region. The SS 304 is essentially also non-magnetic, but under mechanical stress has a higher tendency to become slightly magnetic than SS 316 LN. The vacuum chamber, employed flanges, screws, and other parts are made solely from SS 316 LN stainless steel. The only exception is the combined ion and NEG pump, which has SS 304 parts but also includes a removable permanent magnet necessary for the ion pump operation, however, its position within the chamber corresponds to the farthest placement from the trap, see the Fig. 3.1. The flanges of optical viewports are also made from SS 316 LN, the windows are from fused silica with broadband anti-reflection coatings covering 397 to 850 nm range. Conductors inside the chamber are made from oxygen-free high conductivity (OFHC) copper including feedthroughs to vacuum trap electrode connections, conductors of the in-vacuum thermistor, which wires are isolated by UHV compatible Kapton® isolation. OFHC copper gaskets are silver-plated. The trap holder is from titanium and SS 316 LN. The calcium oven is from stainless

steel, sealed by indium and carried by Macor®. A few screws are gold-plated, the rest is silver-plated. The in-vacuum screws should be hollowed not to create an air cavity, the source of outgassing, our screws are grooved. The trap electrodes are situated in a sapphire crystal holder, which define their precise position.

The Paul trap was manufactured separately in advance and this paragraph covers some useful information about it. The trap is made from six titanium electrodes, the quadrupole and tip electrodes, all of them were electroplated by gold, see the Fig. 3.5-right. In addition, two pairs of SS 316 LN stainless steel electrodes are used for compensation of the micro-motion[98]. The titanium electrodes were cleaned in an ultrasonic (US) bath for first in acetone and subsequently in methanol. The hydrogen fluoride was employed to etch the native titanium oxide layer on the surface. It is appropriate to store the etched and cleaned parts submerged in water or better in some alcohol to slow down the re-oxidation. The tip electrodes were electroplated in solution TSG-250 at the temperature 60 °C for 40 minutes with the current of 10 mA. The radial electrodes similarly for 30 minutes with the current of 5 mA. The established layer of gold was smooth with low roughness, specifically, the grain size is less than a micrometre in diameter, and the layer of gold is approximately 10 µm thick. The layer improves the electrical conductivity for the radio-frequency driving, which reduces the temperature loses and related heating of the trap. The designed distance between the ion and the radial electrode is 566 µm, between the ion and endcap electrodes is 2250 µm. The measured heating rates with single $^{40}Ca^{+}$ ion and employed thermometry on the $4S_{1/2} \leftrightarrow 3D_{5/2}$ transition gave the value (5.1 ± 0.4) phonon/s for the axial motion at 1.2 MHz in the final constructed setup.

3.2.3 Cleaning

Besides choosing the appropriate UHV compatible materials, the crucial point in the process of building any UHV chamber is cleanliness. Outgassing of the residual organic compounds can compete with the pumping speed and limit the achievable vacuum pressure. During the whole cleaning and assembling process, we were strictly using cleanroom suits, nitrile powder-free gloves certified for cleanroom applications, hairnets, and anti-dust mouth masks. The setup was assembled in the regular optical laboratory inside a flow box employing the filter of class H13 of norm EN 1822. Most parts of the vacuum setup were cleaned in the ultrasonic bath with industrial detergent, demineralized (DM) water, and high-performance liquid chromatography (HPLC) grade alcohols, respectively. The thoroughly cleaned parts were always stored exclusively in flowbox during the periods of assembly procedures.

General cleaning procedure

In most cases, we used a cleaning procedure summarized in the Table 3.1. The second step corresponds to filling and pouring out a beaker with DM water while there were bubbles from the detergent, usually 3-5 times. For very greasy parts from the workshop, we repeated steps 1 and 2 ones more, if needed. Steps 4 and 6 mean we changed DM water in the beaker 2-3 times before we filled it by Alcohol. We did not use any ultrasonic bath cleaning for the employed vacuum chamber, silver-plated OFHC copper gaskets, electrical feedthroughs, and optical viewports, as they were specified to be clean upon delivery and so we just wiped them with HPLC methanol before the assembly. Furthermore, windows and feedthroughs can be damaged by US cleaning procedure. The gold-plated trap electrodes were merely submerged in the methanol bath.

Table 3.1: Overview of the general cleaning procedure used mainly for stainless steel parts.

1.	10 min. in US bath in 5% Simple Green®
2.	Rinse under DM water to get rid of the detergent
3.	5 min. in US bath in DM water
4.	Quick rinse (~10 s) under DM water
5.	10 min. in US bath in HPLC aceton
6.	Quick rinse (~10 s) under DM water
7.	10 min. in US bath in HPLC methanol

OFHC copper cleaning procedure

For OFHC copper parts, we employed a distinct cleaning procedure, see the Table 3.2. Copper tends quickly oxidize on the surface when exposed to air. Therefore, the first step is to degrease and remove layers of oxide by etching in diluted citric acid, in our case the industrial detergent Citranox® already contains both. After etching, we rapidly rinsed the parts under flowing DM water and instantly submerged into the beaker with HPLC isopropyl alcohol. The last stage was degreasing in HPLC methanol, the submerge is also useful for short term storage, as an alternative to letting it rust in the air. Note that the employed cleaning procedure for copper parts avoids the aceton cleaning[99].

Table 3.2: Overview of the copper cleaning procedure.

1.	10-15 min. in US bath in 2% Citranox®
2.	Rapid (~2 s) rinse under DM water to get rid of the detergent and immediate submerge into HPLC isopropyl alcohol
3.	10 min. in US bath in HPLC isopropyl alcohol
4.	10 min. in US bath in HPLC methanol

3.2.4 Air-bake

For thoroughly cleaned and outgassed stainless steel chambers pre-pumped with a turbomolecular pump, the limiting residual element with the highest partial pressure corresponds to hydrogen due to its large concentration in stainless steel and high diffusion rate through it[83,B7]. The conventional method of dealing with diffusing hydrogen is based on the establishment of a diffusion barrier on the surface of the stainless steel. Usually, the pure and clean surface is needed when building a vacuum setup, but a layer of oxide on stainless steel works as a barrier for hydrogen. The process of establishing this useful oxide is called an air-baking[100]. It has been predicted and observed that even small coating defects of the oxidized stainless steel flanges can lead to a lateral diffusion and outgassing of hydrogen into the chamber[101].

The air-bake was executed after cleaning procedure of all stainless steel parts including the chamber, blank flanges, reduction, flexible bellow hose, and T-shape pipe. The baking oven was ramped up at a rate of 1 °C per minute to the target temperature 400 °C, where it was maintained for 8 hours and afterwards was ramped down at the same rate to reach room-temperature. The air-bake resulted in a visible golden colour of the stainless steel surface corresponding to chromium-oxide, see the Fig. 3.2.

3.2.5 High temperature pre-bakeout

The most problematic and limiting factor of building UHV is outgassing. The way how to deal with it is choosing low-outgassing materials, reducing contaminants on a surface, meant cleaning process, or decreasing outgassing by using a cryo setup. The outgassing rate of a room-temperature vacuum system is usually decreased by degas procedure at a higher temperature. The approach is to heat the vacuum vessel to increase the outgassing/pressure and pump the system at the state, which degasses the setup much faster. After coming back to room temperature, the system finds a balanced state of pumping/outgassing at a lower pressure level.

Figure 3.2: Stainless steel parts inside the oven. On the left before air-bake, on the right after the air-bake.

Two stages of bakeout become standard in the community. The first one pre-bakeout is at a higher temperature often without temperature-sensitive parts like windows, trap and other. It enables faster outgassing of hydrogen from stainless steel but also water before the final assembly.

Our optical viewports have specified the maximal baking temperature 200 °C. We replaced them by air-baked blank flanges in pre-bakeout. We did not install the trap, trap holder and combined ion/NEG pump. This combination enables pre-bakeout at a temperature 270 °C.

The assembled vacuum system reached a sufficiently low pressure to perform a helium leak test after approximately one hour from the beginning of the pumping. The helium leak test detected no leaks into the chamber. Therefore, we could close the oven and ramp-up the temperature at a rate 15 °C per hour to the final temperature 270 °C. The temperature was held and simultaneously pumped for 9.5 days. The second day of pumping, we also heated the flexible bellow hose at 50-60 °C for a few hours, the temperature was limited by the turbopump, which can be damaged by higher working temperature. The whole outgassing process was monitored by the residual gas analyser (RGA), which showed a substantial decrease of the most prominent residual compounds, including predominant hydrogen, nitrogen/carbon monoxide, water, methanol, carbon dioxide.

The rate of ramp-down temperature was 15 °C per hour, and we let the system under vacuum until we were ready to quickly assemble the final setup. During

opening the vacuum, it is always good to fill the system with high-grade nitrogen gas, because of outgassing of nitrogen is much easier than water absorbed from humid air, also it reduces the risk to contaminate the chamber. We did not have pure nitrogen, so at least we used the dryer to dry the air before the chamber filling.

3.2.6 Final bakeout

When we opened the chamber, we had everything prepared for a quick final assembly to reduce the surface sorption of humidity from the air. We installed the trap holder with trap, calcium oven, thermistor, and all connections. We closed the vacuum chamber by viewports and combined ion/NEG pump without removable magnets, which have to be taken off before baking. The Fig. 3.3 shows the finally assembled chamber inside the oven.

After approximately 1 hour of pumping, sufficiently low pressure had been established to proceed the helium leak test with a necessary tightening of the screws. We closed the oven and set the ramp-up rate of the temperature in the oven to 15 °C per hour. This time the maximum temperature was limited by vacuum windows at 200 °C, we chose the bakeout temperature 195 °C for 10 days.

The second day of bakeout, we heated the flexible bellow hose at 50-60 °C for a few hours to degas, similarly as in pre-bakeout. Note that heating of the hose and pipe were covered by isolation and alumina foil, see the Fig. 3.3. The temperature ramp-down rate was the same as a ramp-up with a targeted 45 °C, which was safe for attaching the ion pump magnets. This was followed by a 1 minute run to test and degas the ion pump. After that, we removed the magnets again. The calcium oven, originally sealed by an indium plug, was heated for 2 minutes to outgas it.

The last step was the activation of the NEG pumps inside the chamber by their driving units. The units have only two working regimes, the weak one conditioning regime and the full activation regime. We started with the conditioning regime to avoid a rapid increase of pressure inside the chamber. First, we switched on the NEG pump near the trap and after about 2 minutes also the conditioning regime of the NEG pump in T-shape pipe. After approximately 15 minutes from turning on the conditioning regime, we set the full activation of the NEG pump near the trap, 2 minutes later also the NEG in T-shape pipe. This leads to higher increase pressure, and we had to stop RGA until the pressure decreased below a safe level. We activated both NEG pumps for 1 hour. During the waiting time for NEG pumps cool down, we disconnected the units and shutdown the oven. When the NEG pump in T-shape pipe cooled down to a safe level, we mounted the magnets and turn on the ion pump. One minute later, we closed the valve between the chamber and the turbomolecular pump and observed the step increase of hydrogen pressure on RGA outside the chamber, which was the sign of NEG pumps pumping. At the

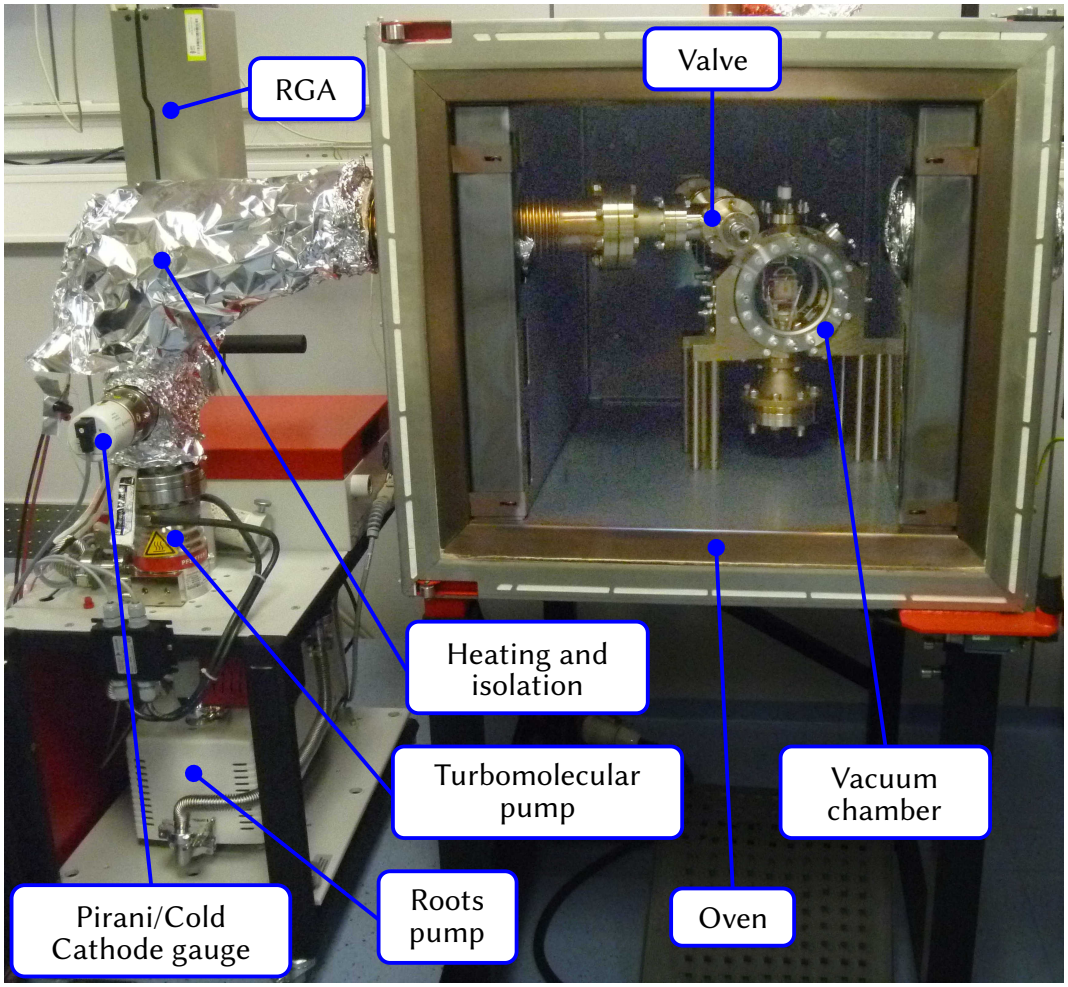

Figure 3.3: The picture shows the final form of the vacuum setup inside the oven before the last bakeout.

point when the oven was still at a temperature of about 40 °C we fully opened the doors of the oven.

The last partial pressures before the valve closure measured by RGA were signifying the dominant residual gas being hydrogen with the partial pressure of $(4.62 \pm 0.05) \cdot 10^{-8}$ mBar followed by more than an order of magnitude lower population of nitrogen/carbon monoxide $(1.5 \pm 0.2) \cdot 10^{-9}$ mBar, carbon dioxide $(1.3 \pm 0.2) \cdot 10^{-9}$ mBar, water $(1.0 \pm 0.2) \cdot 10^{-9}$ mBar and methanol $(6 \pm 2) \cdot 10^{-10}$ mBar, the rest of the residual gases were below the noise floor of the RGA at about $2 \cdot 10^{-10}$ mBar level.

The current on the ion pump decreased quickly, and after an hour we saw on the driving unit the current below 10 nA. After another hour it showed solely

0 nA, it means out of gauge of the ion pump, which corresponds to a pressure $< 10^{-11}$ mBar for nitrogen according to the manual.

3.3 Experimental apparatus

The scheme of the whole vacuum chamber setup including the trap is shown in the Fig. 3.4. The parts are coloured specifically, the pumps are red, the valve is green, the coils are brown, the feedthroughs are yellow. The body of the vacuum chamber is stainless steel octagon with two DN100CF and eight DN40CF flanges. The upper feedthrough serves for connection of the RF voltage to the blade electrodes of Paul trap. The helical resonator is mounted on the top of the feedthrough and it is driven by another coil connected to amplifier and RF generator. The driving frequency of the linear Paul trap is $\approx$ 30.2 MHz. The driving coil of the helical resonator is driven by the power of 1-4 W. The bottom feedthrough connects tip

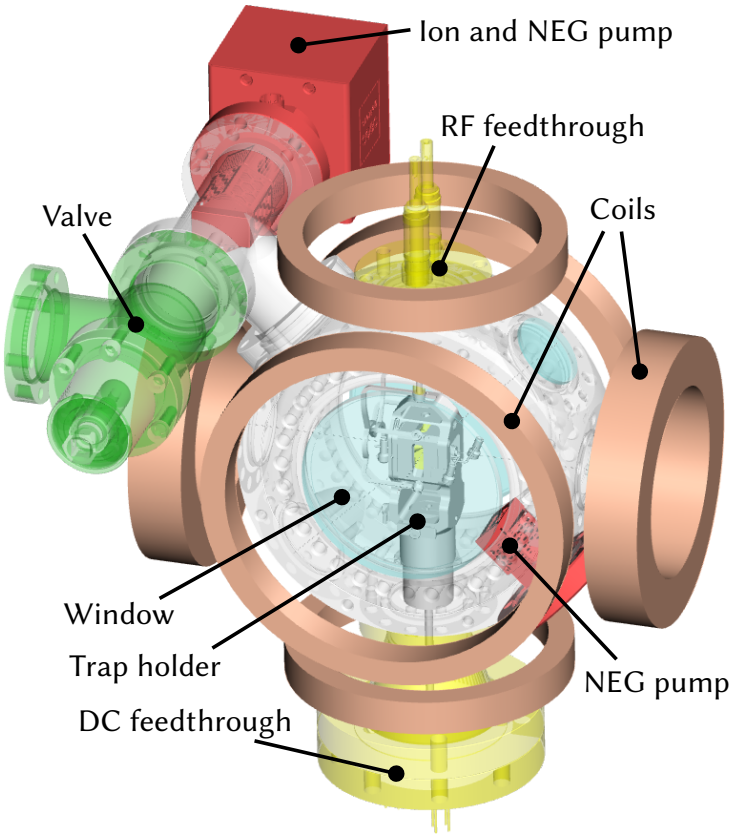

Figure 3.4: Design of the ion trapping apparatus. The parts of vacuum construction are coloured to better distinguish between them.

electrodes, compensation electrodes, calcium oven and the thermistor placed on the trap holder. The magnetic coils are positioned outside the vacuum in all three orthogonal directions, to form a Helmholtz coil for the generation of the nearly uniform magnetic field around the trap area. The currents through the coils are stabilized to produce a static magnetic field needed for lifting the degeneracy of atomic levels.

The Fig. 3.5 shows Paul trap, resistively heated calcium oven, positioning of optical viewports. The axis of optical accesses are printed as solid blue lines. The figure also shows the design of the Paul trap manufactured in the group of R. Blatt from University of Innsbruck.

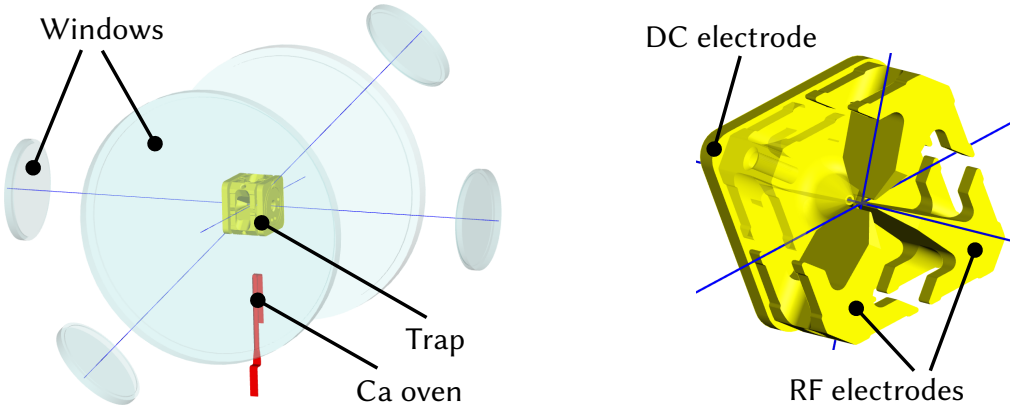

Figure 3.5: The geometric arrangement of the ion trapping setup. The optical windows, calcium oven, ion trap and axis of optical accesses into the trap are shown in the left. The design of the Paul trap is drawn in the right.

The $^{40}Ca^{+}$ ion level scheme is shown in the Fig. 2.9. The ions are Doppler-cooled by a 397 nm laser, which is red-detuned from the $4S_{1/2} \leftrightarrow 4P_{1/2}$ transition and the 866 nm laser is used to depopulate the metastable $3D_{3/2}$ manifold. The fluorescence at 397 nm scattered by ions is collected in a radial direction by an objective (S6ASS2241, Sill optics) covering $\approx 2\,\%$ of the full solid angle. The collection lens is positioned outside the vacuum chamber and the collected photons are often detected on EMCCD camera (Luca-S, Andor), see the Fig. 3.6. The repumper 866 nm and weak cooling 397 nm laser beams are applied at an angle of 45° with respect to the axial trapping direction. The laser frequency and amplitude stabilization schemes and their distribution and delivery to the trap are described in the thesis [102].

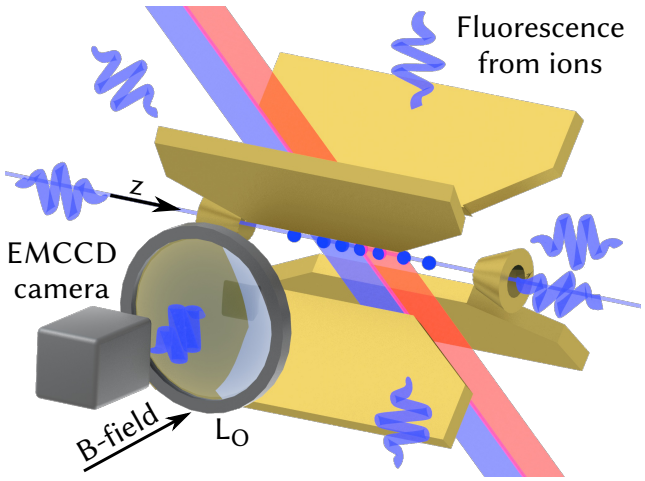

Figure 3.6: A schematic illustration of the experimental setup. Inside the linear Paul trap is a linear chain consisting of $^{40}Ca^{+}$ ions, which scatter the light from the cooling 397 nm laser beam. The fluorescence is collected by a lens L_O positioned outside the vacuum chamber and detected on EMCCD camera. The magnetic field B is applied in the observation direction.

3.4 Estimation of the hydrogen pressure

Most of the ion trapping apparatus worldwide have not any precise vacuum gauge inside the chamber and the only available information for vacuum pressure estimation is given by the current flowing through the ion pump. The attainable knowledge from the current is rough and provides limited knowledge about the vacuum pressure achieved inside the chamber and even less, at the particular position of the trapping region, which is typically far away from the pump due to ion pump includes a permanent magnet. This section focuses on the utilization of the inelastic interaction between trapped ions and background gas for the estimation of the background gas pressure. Specifically, the reaction of trapped $^{40}Ca^{+}$ with background gas hydrogen was used to estimate the partial hydrogen pressure inside the vacuum chamber.

3.4.1 General description

It seems that the low vacuum pressure is the goal. Actually, the sufficient lifetime of the crystal is the aim, and vacuum pressure is the determining factor. For a scalable system with many ions, it is challenging to reach a satisfactory long lifetime, which is mainly limited by the vacuum level around the trap, the laser cooling efficiency, or physical properties of the employed trap. In turn, the ion crystal

lifetime with some additional information can serve as a probe of the background gas pressure.

The most conventional method for estimation of vacuum pressure, which employing collisions of background gas atoms/molecules with trapped ions, involves the elastic momentum transfer resulting in a swap of ions positions, thermalization of the whole crystal, or even direct ejection of ions from the trap[82]. Note that we estimated our trapping potential to be around 3.5 eV, which is a relatively high depth preventing the escape of thermalized ions from the trap, and we have not observed any ion loss in the standard experiments. For example, experiment [4] with $^{171}Yb^{+}$ ions reported the mean time between Langevin collisions in the order of one collision per hour per trapped ion. For 53 ions they observed an average lifetime of about 5 minutes, with rare events the long ion chain could survive for up to 30 minutes. The rate of single dark ion position change in the $^{40}Ca^{+}$ crystal was observed with a period 86 s on average for a 6 ion crystal chain and 27 s for a crystal of 20 ions[103]. The authors claim that not all of these collisions had enough energy to thermalized the whole crystal. The similar experiment employing $^{171}Yb^{+}$ observed with 5-ions including single dark resulted in a hopping rate with a period 49 s on average[104]. The recent rigorous analysis of the reordering rate as a function of the reorder energy barrier for a two-ion $^{40}Ca^{+}$–$^{27}Al^{+}$ crystal, for the purpose of estimation the frequency shift of the optical atomic clock induced by collisions with background gas, resulted in the hydrogen background gas pressure of $(5.19 \pm 0.08) \cdot 10^{-10}$ mBar[82].

As already mentioned, for further decrease of a vacuum level, the cryogenic vacuum setup[75,76] can be employed, which is also speeding up and simplifying the vacuum building procedure due to the suppressed outgassing rate. The background gases have reduced kinetic energy in cryo setups, which positively affects the lifetime of crystals and the observability of collisional heating is limited. The background gas molecules typically do not have enough energy to thermalize or at least swap ions and some energetically lower process of transition between two states has to be employed. The zig-zag crystal structure is a great example of a weakly stable configuration, and by counting the number of swaps, the background gas pressure was estimated to $P_{4.7K} < 1.3 \cdot 10^{-12}$ mBar for an experiment[76].

Let us stress that these types of measurements observing the consequence of momentum kick from background gas are highly dependent on the exact crystal configuration, potential depth, potential profile, laser cooling parameters, thus they are not easily comparable. In addition, the detection of thermalization ion crystal can be complicated due to the short Doppler re-cooling time. From the mentioned experiments, it is noticeable that the crystal structure reordering can be detected by the position change of one or more dark ions. If it is assumed that the ordering of ions after re-crystallization is random, then the probability of the

dark ion position change is easily calculated from the number of ions. It should be emphasized again that the mentioned momentum transfer measurements are highly dependent on the height of the reorder energy barrier[76,82], which has to be carefully calibrated.

Another cryogenic setup[75] reported the implementation of unwanted charge-exchange between background gas and trapped ions, which is more likely for highly charged trapped ions. The highly charged single Ar^{13+} ion was sympathetically cooled by a single laser-cooled Be^{+} ion and the lifetime of this two-ion crystal was measured. The interaction of interest corresponded to charge-exchange between hydrogen and a single Ar^{13+} ion, by which the upper limit of the vacuum pressure $P_{4.6K} < 1.26(-0.11/+0.12) \cdot 10^{-14}$ mBar was derived.

We decided to implement vacuum pressure measurement based on a chemical reaction between trapped ions and background gas, namely, $^{40}Ca^{+}$ and residual hydrogen in the chamber. The advantage of employing a molecular reaction is the high insensitivity to trapping potential shape and depth and also to laser cooling parameters. However, it is not insensitive to laser excitation parameters in general, since the reaction is photochemical. With detailed knowledge of the particular reaction between an atomic/ionic isotope and a specific contaminant, it can serve also for residual gas analysis.

3.4.2 Reaction rate measurement

The knowledge about the vacuum pressure in our setup is limited, the ion pump shows current 0 nA. In addition, we do not observe any dark ion production, we have the last RGA data before closing the valve, the data confirms the general understanding that hydrogen is typically the most representative background gas in stainless steal UHV chambers.

The setup employs $^{40}Ca^{+}$ trapped ions and so the estimation of the partial pressure of hydrogen can conveniently utilize the measurement of the reaction rate[93,94] for the reaction

$$^{40}Ca^{+}(4P_{1/2}) + H_2 \rightarrow {}^{40}CaH^{+} + H. \tag{3.2}$$

The reaction is photochemical, which means that the population of the $^{40}Ca^{+}$ ion has to be excited to the upper electronic level by light, in this case to the $4P_{1/2}$ level. The dynamics of the reaction is given by the equation[93]

$$N_{^{40}Ca^{+}}(t) = N_{^{40}Ca^{+}}(0) \cdot e^{-\gamma \cdot t}, \tag{3.3}$$

where $N_{^{40}Ca^{+}}(t)$ is the number of non-reacted ions after time t, $N_{^{40}Ca^{+}}(0)$ is the number of non-reacted ions at the beginning of the measurement $t = 0$ and γ

is the reaction rate. The reaction rate can be expanded as $\gamma = p_e n_{H_2} k_r$, with p_e representing the excited state population of the $4P_{1/2}$ level, n_{H_2} is the number density of the H_2 gas, and k_r indicates the reaction rate constant. The number density n_{H_2} together with the equation of state give the final partial pressure of hydrogen $P_{H_2} = n_{H_2} k_B T$.

The number of reactions of trapped $^{40}Ca^+$ ions with background gas hydrogen is too low due to the low number density n_{H_2} of hydrogen in our ordinary experimental settings, therefore the number of probe ions and the $4P_{1/2}$ level population p_e were increased to improve the observability in reaction rate measurement. A reasonable number of 34 $^{40}Ca^+$ ions was chosen for the stability of crystal in the trap, and the possibility of near-equal saturation parameter for all ions. The Doppler cooling during a typical experiment corresponds to the probability p_e on the order of a few percents or lower, which is not satisfying for the measurement in the chamber of advanced UHV pressure. The steady-state solution of 8-level optical Bloch equations was used for fitting the data from fluorescence spectra measurement with four dark resonances shown in the Fig. 3.7. This served for a precise calibration of the fluorescence intensity observed on the EMCCD camera to the probability p_e. The probability of excited state was tuned up to the average value of $p_e = (15.9 \pm 1.7)\,\%$ for every ion in the string using the global excitation beam.

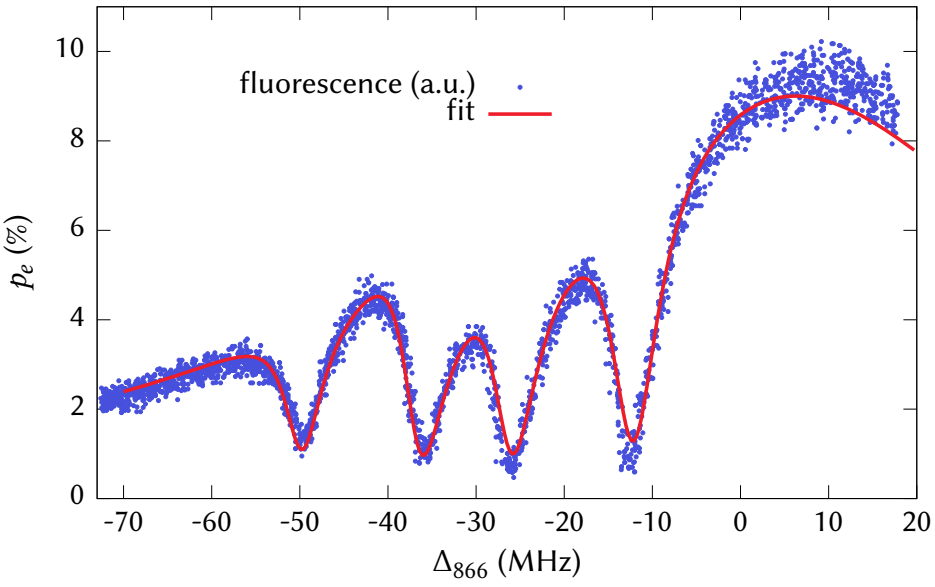

Figure 3.7: The measured fluorescence spectra as a function of the 866 nm laser detuning. The fit corresponds to a steady-state solution of 8-level optical Bloch equations and serves for a precise calibration of EMCCD camera by the value of $4P_{1/2}$ level population.

The higher value of p_e was not used, because the stability of the ion crystal was starting to significantly degrade in the long term. After all these adjustments, the observation time of the single reaction was still very long, and thus the laser beams with stable parameters were ensured by a frequency lock to the optical frequency comb, referenced to a hydrogen maser[102].

The whole measurement took 51 hours. The ions were trapped in linear chain configuration for individual observability of each ion. The 3 W power went into the driving coil of the helical resonator, which resulted in radial centre of mass motion frequencies $f_x \approx f_y \approx 1.86$ MHz. The axial tip voltage was set to $U_{\text{tip}} = 8$ V, which resulted in linear ion chain configuration for trapped 34 $^{40}Ca^+$ ions with the corresponding axial COM mode frequency of $f_z \approx 91$ kHz. At these trapping potential settings, the micromotion was precisely optimized. During the long term measurement, we observed extremely rare events when the 397 nm beam excited the $4S_{1/2} \leftrightarrow 4P_{3/2} \leftrightarrow 3D_{5/2}$ Raman transition. Therefore, we utilized continuous 854 nm laser excitation set close to the $3D_{5/2} \leftrightarrow 4P_{3/2}$ transition resonance for depopulating the $3D_{5/2}$ level. An additional strong 397 nm laser beam used for equal excitation of all ions in the string was applied along the axial direction as well as the reset 854 nm beam. Picture from EMCCD camera of the formed linear chain containing 34 $^{40}Ca^+$ ions is shown in the Fig 3.8. The bottom image was taken

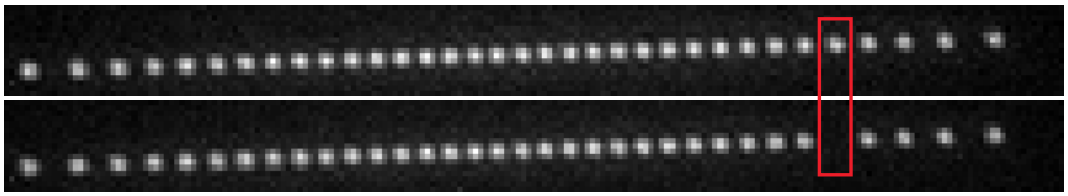

Figure 3.8: The image of the 34 $^{40}Ca^+$ ion string taken by EMCCD camera during the measurement (top picture). An rare event, when a single ion from the linear chain became dark due to a chemical reaction (bottom picture).

when the extremely rare event happened, one ion became dark during the reaction rate measurement. All pictures of 34 $^{40}Ca^+$ ion crystal have been taken with 500 ms acquisition time and corresponding capture rate of 1.95 Hz. From the time-lapse record, each snapshot was taken and processed individually in the following way. Around every image of ion, the square border was drawn, see the Fig. 3.9, and the average count rate from the area was evaluated to differentiate between bright and dark ion.

The comparison of the average count rate per pixel between the bordered bright ion and background of the EMCCD camera was made. A representative histogram of the evaluated areas of fluorescing ion versus background is shown in the Fig. 3.10. It demonstrates that the fluorescing ion is well separated and recognized from the background on EMCCD camera. Even though the acquisition

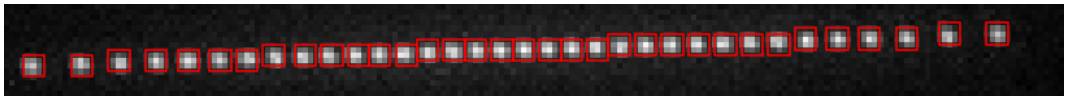

Figure 3.9: The image of the 34 $^{40}Ca^{+}$ ion string taken by EMCCD camera during the measurement. The red squares represent borders of the areas used to process and evaluate whether the selected ion is bright or dark.

time is 500 ms, this separation guarantees the observability of non-fluorescing ion at time scales beyond 250 ms.

In total, four reactions were observed within the whole measurement. They were found in the measured data by post-processing. The product of the reaction became non-fluorescing and stayed in this dark state for minutes, specifically for 63.5 s, 934.5 s, 506 s, and 366.5 s. After that time the ions became bright again, this is most likely attributed to the off-resonant photodissociation[96]. These dark ion times at the order of minutes statistically exclude any further uncaptured single ion non-fluorescing events, which means that any chemical reaction followed by

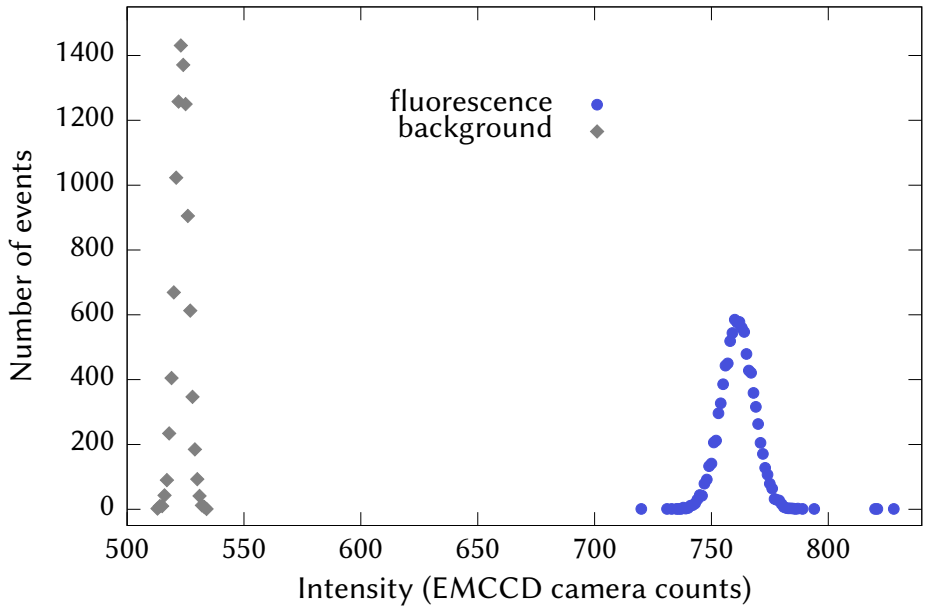

Figure 3.10: The histogram of measured intensities corresponding to average counts per pixel per acquisition time 500 ms from EMCCD camera. The blue circles and grey squares represent the average intensities from the area around the outermost ion in the 34-ion string and the area of the same size positioned at a corner of the picture shown in the Fig. 3.9, respectively. The graph is evaluated from 10^4 recorded images.

dissociation faster than the recognition time of about 250 ms with the same experimental settings. For that reason, we could conclude that there were not any other reactions except four per 51 hours. It gives 1 reaction per 12.75 hours on average.

We also suppose that all four reactions are associated with the photochemical reaction of $^{40}Ca^{+}$ with H_2 according to the eq. (3.2), which is based on the assumption that hydrogen is the most representative contaminant, which comes from the RGA measurement before closing the valve, the fundamental knowledge of the UHV system, and the standard residual content of the most apparatus build on stainless steel UHV parts[75,76,82,83,B7]. Thus, it is highly improbable that the trapped $^{40}Ca^{+}$ ions reacts with other species of a background gas, therefore the calculated partial pressure of hydrogen represents an upper limit of this value, because of the contribution of other elements to observed reactions would effectively correspond to lower concentration of hydrogen inside the chamber.

The equation (3.3) and the equation of state were used to calculate the upper limit for the partial pressure of hydrogen inside the chamber with a resulting value $P_{H_2} \leq (2.1 \pm 1.1) \cdot 10^{-13}$ mBar for the reaction rate constant k_r from reference [93] and $P_{H_2} \leq (5.5 \pm 2.8) \cdot 10^{-12}$ mBar for k_r from [94].

The error bars of the calculated partial pressure of hydrogen were given by the convolution of a standard deviation of the $4P_{1/2}$ level population p_e and from the statistical uncertainty of four reaction events. The standard deviation of probability p_e was estimated from the uncertainty of dark resonances calibration of EMCCD camera intensity scale. The main source of uncertainty is given by the random and time-independent success of the four reaction events. As it is a substantial number of trials with a small success probability, the limiting case of the binomial distribution corresponding to Poisson distribution was used.

3.5 Summary

The UHV construction can be perceived more like a routine[A1,105] nowadays, but still, there is necessary knowledge needed for achieving the sufficient vacuum level including some particular requirements for ion trapping systems. The final pressure inside the vacuum chamber is important for the lifetime of a trapped ionic crystal. The tendency of scaling up the number of ions puts higher requirements on vacuum quality for the preservation of crystal lifetime. The final UHV pressure surrounding the trap has proven the ability to work with large ion crystals for long storage and measurement times, which was crucial for observation of specific quantum optics phenomenas presented in chapters 4 and 5.

We presented a reaction rate measurements to quantify the partial hydrogen pressure inside the vacuum chamber. Including a list of relevant references em-

ploying the lifetime of the trapped crystal as a probe of background gas pressure. The estimation of the $^{40}CaH^+$ molecule formation rate puts the upper limit on the partial pressure of hydrogen $P_{H_2} \leq (2.1 \pm 1.1) \cdot 10^{-13}$ mBar for the reaction rate constant k_r [93] and $P_{H_2} \leq (5.5 \pm 2.8) \cdot 10^{-12}$ mBar for k_r [94]. We observed four photochemical reactions during the 51 hours long measurement in sum with a string consisting of 34 $^{40}Ca^+$ ions, it is the lowest reported number in a room-temperature ion trapping system, to our best knowledge.

Meanwhile, we were measuring the experiment a similar estimation of hydrogen partial pressure with trapped $^{171}Yb^+$ ions was published[76]. The dark ions production from ytterbium ions by collision with hydrogen can follow two paths, population trapping in the metastable $^2F_{7/2}$ state of ytterbium, or production of YbH^+ molecules. By independent estimation of the dark ion rate production in the cryogenic vacuum setup, the pressure $P_{4K} < 1.3 \cdot 10^{-13}$ mBar was calculated.

The main ideas and core of this chapter about vacuum building and hydrogen pressure estimation were summarized in the article [A1], and the intent was to produce a solid reference for dealing with UHV systems.

Chapter 4

Scalable interference from long ion strings

This chapter reports on the measurements of multi-path interference of single photons scattered from trapped ions. The interference patterns are presented from different sizes of ion crystals. The controlled interference of light is observed from a linear crystals containing up to 53 trapped ions. The results of the observation are summarized in the article [A1].

4.1 Introduction

The wave character of light was diligently examined for many decades. At the beginning of the 19th century, the double-slit experiment was described, also known as Young's interference experiment after Thomas Young. The experiment demonstrates the wave-like behaviour of light when two waves interfere to produce an interference pattern. The sketch of the experiment is shown in the Fig. 4.1-left.

After comparison of the atomic sizes with the wavelengths of atomic resonance fluorescence, it can be claimed that the atoms are point-like emitters, still, their localization can be challenging[106]. If we replace the slits by atoms in Young's interference arrangement, as shown in the Fig. 4.1-right, we get the similar type of interferometer. However, compared to the conventional case with coherent laser inputs, atoms are in addition saturable single-photon emitters with internal discrete energy level scheme.

In short, the interaction of coherent light with quantum-like particles already acquitted oneself well as a platform for testing the fundamental theories and as a device of prospective applications, especially with atomic systems[B8,B9]. The suitability is caused by the extremal sensitive response of scattered coherent light to

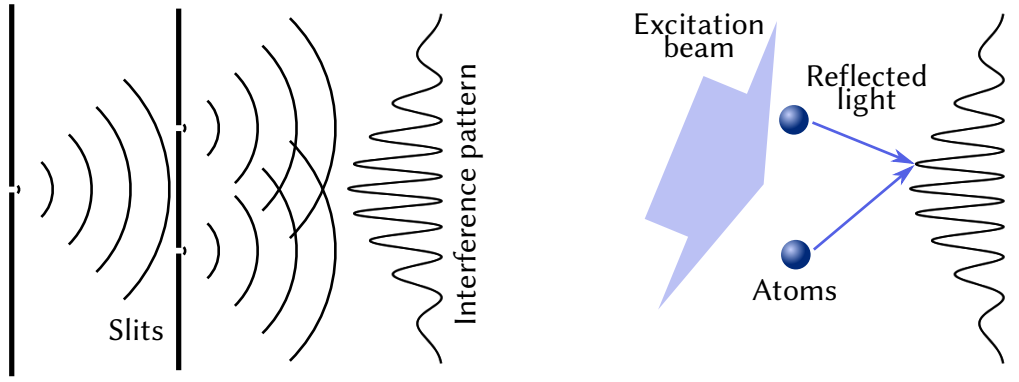

Figure 4.1: The picture on the left illustrates the original Young's interference experiment. On the right is shown an equivalent interferometer, where the slits are substituted by the atoms, the interference pattern is plotted in the far-field.

intrinsic and environmental effects, which the atomic ensembles offer[B10]. Therefore, that kind of systems and the impact of their collective effects were theoretically studied[34,107–109]. Experimentally, the preservation of optical coherence after scattering from atoms finds the application in crystallography[B11,110]. The Bragg scattering was also observed from many atomic emitters beyond the solid crystal structures, when the neutral atoms were localized in optical lattices[111–119] at large inter-atomic distances and also from ions trapped in the Penning trap[120,121].

The interference from individually addressable ions, same as multi-path interference[122] and with control over the positional errors causing phase jitter[123] has been experimentally observed just from a maximum of four ions[35–38,124].

The possibility of scaling up the number of emitters without dramatically losing coherence can offer the optical generation of multi-partite entangled states[125–130], design the enhanced and controllable source of collective atomic emission[131–136], or in turn, improve the collection and absorption of photons in few-atom ensembles[134,135,137,138].

4.2 Experimental setup

The linear configuration of the atoms is the simplest and natural approach of scaling emitters in the mentioned Young's interference experiment, shown in the Fig. 4.2. In essence, the observability of the interference pattern is given by the contrast of fringes. In the mentioned linear configuration, the density of fringes is high in the radial direction and increases with the number of atoms. It imposes requirements on the higher spatial detection resolution, moreover narrower fringe is coupled with lower efficiency, and this unfavourably affects contrast and the

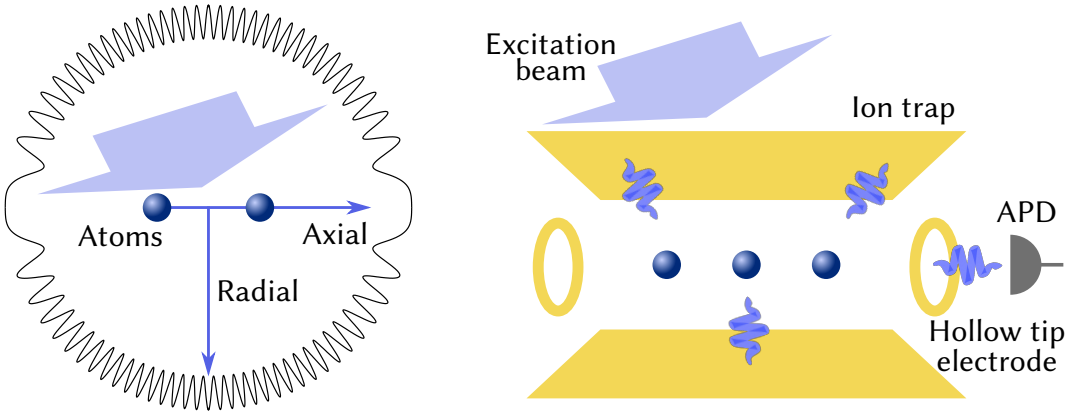

Figure 4.2: The picture on the left illustrates the density of the interference pattern, in a far-field, as a function of scattering direction from two atoms. On the right is displayed an experimental realization with ions in the Paul trap, the arrangement is convenient for observation of the interference in the axial direction.

possible observability of interference pattern even for a low number of ions[35,37]. Observation of the interference pattern in the axial direction has a couple of advantages, including mentioned low density of fringes and perfect indistinguishability of emitters. These attributes guarantee exclusive overlap of radiation from atoms and low gradient in the interference pattern, still it preserves the fundamental addressability of individual atoms in the radial direction. The illustration of the realistic experimental arrangement is shown in the Fig. 4.2-right.

It is convenient to scan the interference pattern by changing the inter-ionic distance by tuning the voltages on the tip electrodes in this configuration. The biggest disadvantage of the employed geometry in our particular experimental setup corresponds to coupling the radiation through the holes in the tip electrodes with very small aperture, which reduces the coupling efficiency. The internal diameter of the hole in the tip electrodes is just 0.5 mm, corresponding to the solid fraction angle of $\Omega_{ax} = 1.3 \cdot 10^{-5}$, which unfavourably affects the collection efficiency.

We have to choose a specific trapping potential to trap the $^{40}Ca^{+}$ ions as linear ion chains along the axial axis. The potential has to be tighter in the radial direction than in the axial, which we secured by ≈ 2.5 W of input power into the helical resonator, this resulted in the radial secular frequencies $f_x \approx f_y \approx 1.66$ MHz, while the axial potential was tuned by lower static voltage in the range from $U_{tip} = 4$ V up to $U_{tip} = 900$ V, corresponding axial frequency range was $f_z \approx 60$ kHz–1044 kHz. The micromotion was compensated for all these voltage settings by additional micromotion compensation electrodes.

The interference is observed for the scattered 397 nm laser light, which is red-detuned from the $4S_{1/2} \leftrightarrow 4P_{1/2}$ transition as a standard Doppler cooling laser

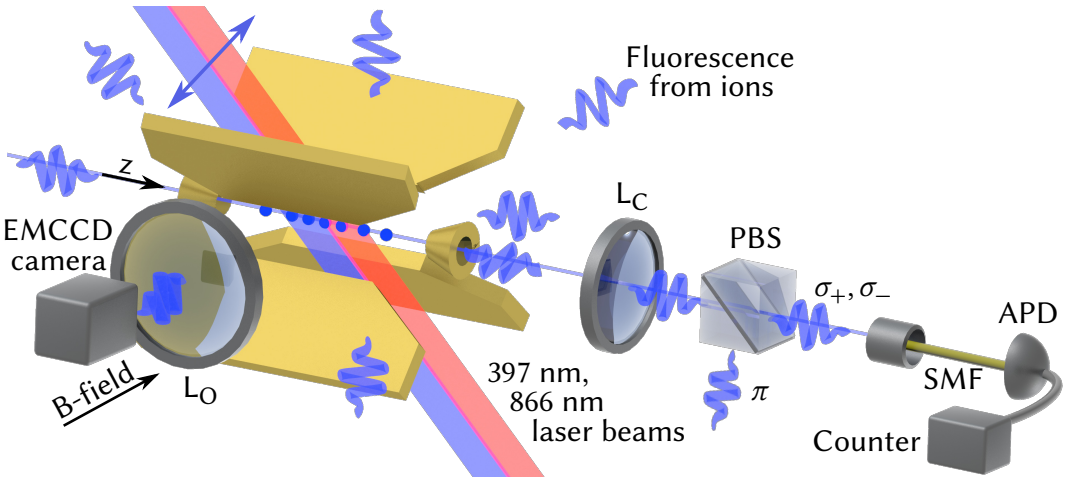

Figure 4.3: The picture shows a simplified scheme of the employed experimental arrangement. Ions confined in the linear Paul trap scatter the excitation 397 nm laser light. The phase interference is observed along the trap symmetry axis through a small aperture in the tip electrode. The light is collected by the coupling lens L_c and its polarization is filtered using a polarization beam splitter (PBS) to maximize the portion of elastically scattered photons in the detected signal. The scattered light is detected by the single-photon avalanche photodiode (APD) after coupling into the single-mode fibre (SMF). The phase of scattered light is tuned by adjustment of the applied axial potential strength through voltages U_{tip}. The radial observation direction serves for the observation of the ion crystal on the EMCCD camera. The static magnetic field $|\vec{B}| = 6.1$ Gauss is applied in the same direction.

beam, see the Fig. 2.9. The scattering was carried out in the continuous regime. We simultaneously employed the 866 nm laser for reshuffling the $3D_{3/2}$ population back to the $4P_{1/2}$ level coming from the $4P_{1/2} \rightarrow 3D_{3/2}$ decay. The experimental setup scheme is shown in the Fig. 4.3, both laser beams propagate through the centre of the trap at an angle 45°.

The polarization of the excitation beams is perpendicular to the magnetic field, which is static and with the amplitude of $|\vec{B}| = 6.1$ Gauss. The scattered light is collected in two directions, radial and axial. In the radial direction, where the magnetic field is applied, the light is collected through the high numerical aperture lens onto the EMCCD camera. The ion observation on the EMCCD camera serves for the ion number counting, inspecting the ion crystal stability, rough checking of spatial distribution of ions, and their individual emission intensity. The detection efficiency of photons scattered in the axial direction is restricted by the hole in the tip electrode. The photons are transmitted from the chamber by a vacuum window. The collection is done by a single plano-convex lens L_C with focal length $f_C = 150$ mm, which is positioned 150 ± 2 mm from the trap centre to collimate the

fluorescence. The photon coupling into the single mode optical fibre is ensured by a mirror and the fibre coupler, in front of which the PBS is positioned. The PBS is set to filtering out the π photons and to transmitting the photons scattered from the σ^+ and σ^- atomic transitions, which maximizes the overlap between the detectable photons and the polarization of the excitation laser beam. This serves for optimizing the amount of elastically scattered photons in the detection mode. The photons are coupled into a single-mode (SM) fibre, which guarantees transmission only the fundamental LP_{00} spatial optical mode. The configuration became a robust detection ensemble after coupling the scattered light into the SM fibre. The SM fibre is connected to a fibre-coupled single-photon avalanche photodiode (APD) with a quantum efficiency of 77 % specified by the manufacturer.

The most significant detection losses come from coupling through the small hole in the tip electrode, which contributes to the reduction of the detection efficiency by a value of $1.3 \cdot 10^{-5}$ by transmitting a tiny fraction of the solid angle. By adding the rest of loses, we find the overall calculated detection efficiency of $\eta_e = 3.7 \cdot 10^{-6}$ for photons emitted from ion located at the centre of the trap. This value very well corresponds to the measured absolute detection efficiency of $\eta_m = (3.6 \pm 0.4) \cdot 10^{-6}$. The experimental measurement of detection efficiency was done in the pulse sequence by preparing the population in the $3D_{3/2}$ manifold and counting the 397 nm photons produced by the spontaneous Raman transition $3D_{3/2} \rightarrow 4P_{1/2} \rightarrow 4S_{1/2}$ in comparison to the total number of trials[A3,41], the process will be described in the subsection 5.3.2 in more detail.

For further investigation of the coupling, we measured the count rate from a single ion as a function of displacement from the centre of the trap in the radial direction. The measurement resulted in a Gaussian-like profile of cut through the detection optical mode, by fitting the data, we obtain the waist $w_0 = 17\,\mu m$ of the detection gaussian mode. It corresponds to the Rayleigh length of $z_R = 2.3\,mm$ for scattered laser light at 397 nm wavelength. Therefore, the light scattered from long ion strings should be coupled with similar efficiency for all ions aligned along the axial optical axis in the Rayleigh length range. The experimental veryfication of the independence of the detection efficiency on the axial position was done also by directly measuring the count rate from a single ion positioned on the axial axis in the observational range of our EMCCD camera, see the Fig. 4.4. As expected, the blue triangles show the near-constant count rate from a single ion at different axial positions inside the trap within the range wider than 500 µm. The figure includes a camera picture of 53 ions, which are linearly aligned at U_{tip} =5.3 V. The red dots correspond to calculated positions of ions in this linear string. This crystal represents the longest string of ions we employed for observing the interference pattern. Its spatial extension at the applied axial voltage U_{tip}=5.3 V is 367 µm. These measurements confirm the uniform coupling efficiency of radiation through the holes in

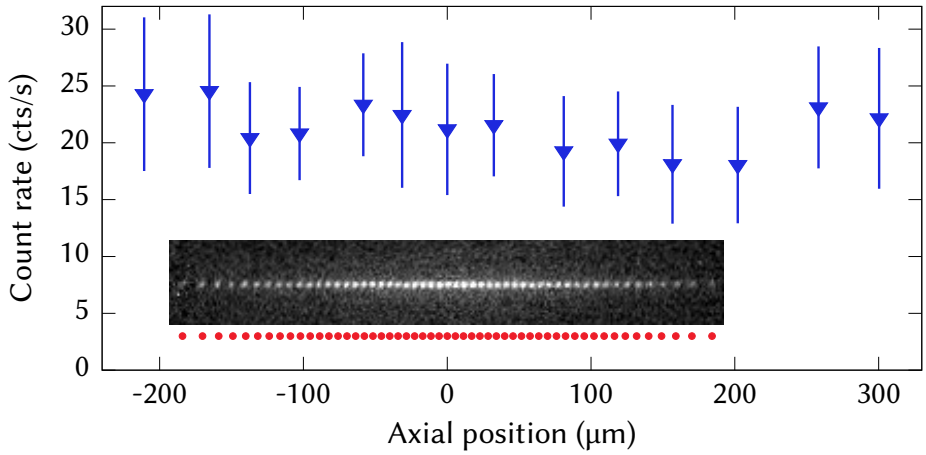

Figure 4.4: The blue triangles represent the measured count rate coupled through the tip electrode hole as a function of the single-ion position on the axial axis when the zero indicates the centre of the trap. The picture illustrates the crystal containing 53 ions at the lowest voltage $U_{\text{tip}} = 5.3\,\text{V}$ employed in the presented experiments and the red dots represent the same situation with calculated positions. The image of ions serves as a demonstration of the maximal spatial extent of the measured linear chain.

tip electrodes from axially positioned ions in a wide range of positions. Together with the smallest gradient in the interference pattern, the axial configuration is also convenient for bulk detection of scattered light.

4.3 Observation of coherent light scattering

This section describes the measured interference patterns produced by a various number of ions formed as linear Coulomb crystals inside the Paul trap.

4.3.1 Two-ion interference

The setup introduced in previous sections is expected to be a scalable system with respect to the number of ions for observation of scattering in single spatial mode. The observation of interference of light emitted by two ions is the simplest case, and it will be described in detail, as it can serve for calibration purposes and straightforward estimation of many crucial experimental parameters. The Fig. 4.5 shows the drawing of the excitation and detection geometry. The excitation laser beam is incident at an angle of $\theta_{397} \approx 45^\circ$ on two ions distant $d_{2\text{ion}}$ in the radial observation direction of EMCCD camera. The distance of the ions is tuned by the

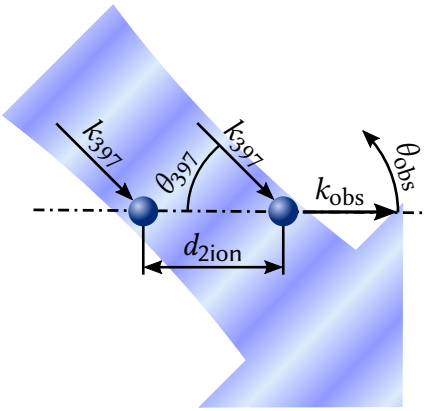

Figure 4.5: The picture shows the geometric arrangement of two ions with a mutual distance d_{2ion}. The interference is observed in the direction of k_{obs} at an angle $\theta_{obs} = 0^{\circ}$. The excitation laser beam is incident in the direction of k_{397} at an angle θ_{397} with respect to the crystal axis.

voltage U_{tip} applied to the tip electrodes, which determines the exact position of the individual ions in the calibrated trap[54], as discussed in the subsection 2.1.3.

The 866 nm laser beam has the same path as 397 nm, it is employed as repumper and for simplicity is excluded in the figure. The wave vector k_{obs} represents the observation direction, which corresponds to the angle $\theta_{obs} = 0^{\circ}$. Two ions with a small probability reflect the incident 397 nm light and the scattered light can be indistinguishably detected in the observation direction. The interference pattern can be conveniently tuned by controlling the distance d_{2ion}. The effective distance between the two ions for the incident laser beam is $d_{397} = d_{2ion} \cdot \cos\theta_{397}$, therefore the total relative phase difference is $\delta\varphi = d_{2ion}(1 - \cos\theta_{397}) \cdot \omega_{397}/c$, where ω_{397} represents the angular frequency of scattered photons and c is the speed of light.

The measured count rates of scattered light from the two-ion crystal as a function of U_{tip} are shown in the Fig. 4.6. The horizontal voltage axis is linearized in terms of two-ion distance d_{2ion}, the count rate data corresponds to the 20 s integration time. The error bars were evaluated statistically from four 5 s long data samples with the deducted background. The background count rate (9.3 ± 1.2) cts/s was measured without 866 nm repumper laser beam in a 200 s long measurement, the value of it is shown as a solid black line and a dot with an error bar depicts the measured data point. The manufacturer defines the dark count rate of 10 cts/s. Therefore, we can conclude, that the level of the background corresponds almost exclusively to the dark counts of the detector, which is mostly a consequence of coupling through the tip-electrode hole, that significantly affects the contrast of the fringes.

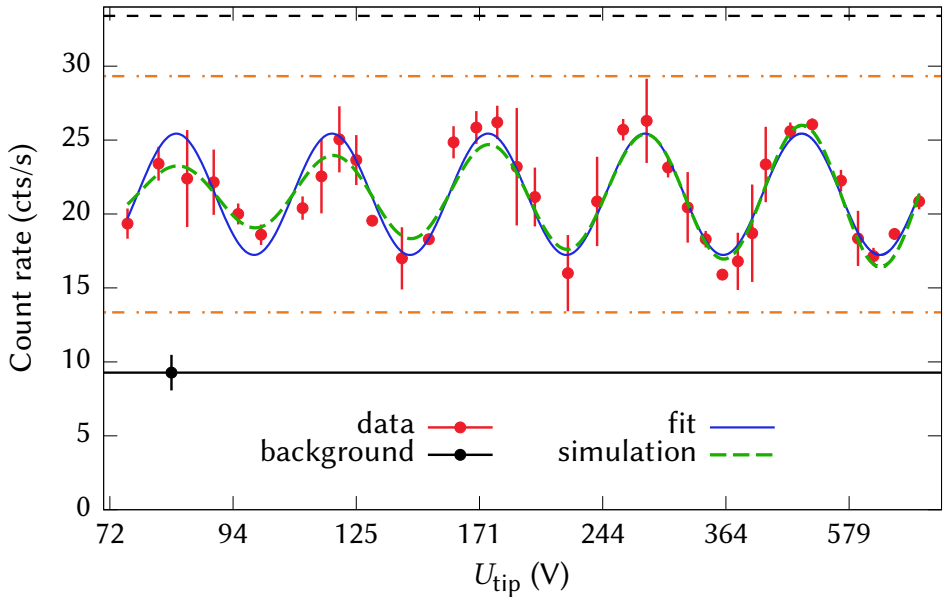

Figure 4.6: The interference fringes from two ions measured as a function of tip voltage. The horizontal axis is not linear in voltage, but in the two-ion distance. The red dots represent the measured photon counts per second, the solid blue line corresponds to the numerical simulation with fitted amplitude and offset to the data. The solid black line shows the level of measured background, the dashed black line corresponds to the maximal constructive interference value for the light with the same amplitudes and for ideal fully coherent scattering. These clues are reduced to the upper and bottom dash-dotted orange lines by including the independently estimated portion of inelastically scattered photons. The dashed green line includes also the effect of position jitter due to the estimated finite populations of motional modes.

The measured interference pattern can be described by equation

$$I_{\text{det}} = 2I_1(1 + |g^{(1)}| \cos(\delta\varphi)). \tag{4.1}$$

It depends on the relative phase $\delta\varphi$, the light intensity from a single ion I_1 when considering the same intensity contributions of both ions and the degree of the first-order coherence $g^{(1)}$. The solid blue curve stands for the fitted function, where amplitude and offset were the fitting parameters, they correspond to the I_1 and $|g^{(1)}|$ from eq. (4.1). The phase factor $\delta\varphi$ in the presented fits was given by the two-ion distance $d_{2\text{ion}}$, which is set by the voltage on the tip electrodes U_{tip} and by the angle of the incident laser beam θ_{397}. The interference pattern is sensitive to the angle, therefore we precisely estimated the distances by a tape measure and calculated the angle as $\theta_{397\text{-M}} = (45.24 \pm 0.06)^\circ$, the mentioned fit

can be also adjusted and exploited to fit the angle, this gave us the matched value $\theta_{397\text{-fit}} = (45.19 \pm 0.04)^\circ$.

The interference oscillations obtained by the fit were used for estimation of the visibility $V = (I_{\text{fit}}^{\max} - I_{\text{fit}}^{\min})/(I_{\text{fit}}^{\max} + I_{\text{fit}}^{\min}) = |g^{(1)}| = 19\,\%$, where the indexes max and min mean the maximal and minimal value, respectively. After subtraction of the background counts the visibility increases to $V = 34\,\%$. The value is comparable with previously realized phase interference experiments with Doppler cooled ions[36–38].

The contrast of the interference pattern is mainly decreased by two principal reasons. The first is the inelastic scattering of the photons, and the second is the ion motion, which causes optical dephasing[36–38,139]. Both effects were optimized before the measurement. The low excitation regime was established to enhance the fraction of elastically to inelastically scattered photons. The frequencies of lasers were tuned to optimize the cooling conditions while maximizing the contrast of the fringes. The model of the eight-level optical Bloch equations was used to fit the dark resonance spectroscopy measurement to get the laser excitation parameters. To obtain the ratio of the elastic to the inelastic portion of scattered photons, we found the effective saturation parameter $s_{397} = 0.51$ of the 397 nm laser beam driving the $4S_{1/2} \leftrightarrow 4P_{1/2}$ transition. The saturation parameter of weak laser beam detuned by Δ is given by[B12,B13,140]

$$s = \frac{\frac{\Omega^2}{2}}{\Delta^2 + (\frac{\Gamma^2}{4})}. \tag{4.2}$$

Using the equations

$$\begin{aligned} \langle I_{\text{coh}} \rangle &= \frac{1}{2}\frac{s}{(1+s)^2}, \\ \langle I_{\text{incoh}} \rangle &= \frac{1}{2}\frac{s^2}{(1+s)^2}, \\ \langle I_{\text{tot}} \rangle &= \langle I_{\text{coh}} \rangle + \langle I_{\text{incoh}} \rangle, \end{aligned} \tag{4.3}$$

we estimated the portion of the elastically scattered photons as 66 %. This corresponds to the reduction of visibility by a factor of 0.34 in two-ion case, according to the interference law and definition of the visibility.

The motional decoherence mechanism is not so straightforward. It is obvious that the axial motional modes have a direct projection onto the axial observation orientation besides the radial mode, but the axial COM mode does not contribute and the most significant contributor is an axial stretch mode. For the radial mode, the zig-zag motion is the most important and again the COM mode the least.

The dashed green line in the Fig. 4.6 represents the precise simulation when the effects of inelastic scattering and motional decoherence were taken into account. In the ideal case without decoherence, the interference curve was limited at the bottom by a solid black line representing the background count rate and at the top by a dashed black line representing the maximal interference. Due to the portion of inelastically scattered photons, the borders are shifted to the positions of two dash-dotted orange lines. The rest of the decrease of interference amplitude is caused by the secular motion. The Gaussian position uncertainties of the axial stretch and radial zig-zag modes were included in the simulation, the mean phonon numbers of the modes were estimated by spectroscopic measurement. The amplitude of simulation interference oscillation slowly falls for lower voltage. The effect is caused by decreasing the secular frequency of axial mode and associated extension of Gaussian position width. This is in good agreement with the measured data. It underlines the high degree of control. The precise prediction of the interference pattern was obtained just from knowledge of the background count rate, average count rate from a single ion, the portion of inelastically scattered light, and the secular motion simulation.

It was already mentioned that the gradient of the interference pattern is minimal in the axial direction. To illustrate this phenomena, we simulated a particular interference pattern with $N = 2$ ions, where we have fixed the $U_{\text{tip}} = 480\,\text{V}$ at the interference maxima for $\theta_{\text{obs}} = 0^{\circ}$, see the Fig. 4.6, and then we evolved the observation angle θ_{obs}. The graph is plotted in polar coordinates in the Fig. 4.7. The simulation was calculated in the far-field, also the background and decoherence mechanisms were excluded and the amplitude of the radiation from the single ion was normalized to 1, therefore the interference maxima acquires the value 4. The picture conveniently illustrates the angular width of the interference fringes in the axial and radial direction.

4.3.2 Few-ion interference

This subsection presents the observation of interference from a larger number of ions $N > 2$. The intensity of fully coherent light scattered from N emitters and observed in the axial direction can be calculated from their superposition

$$I_{\text{coh}} = \left| \sum_{j=1}^{N} A_j e^{i\Delta\phi_j} \right|^2 , \tag{4.4}$$

where A_j is the amplitude of scattered light from j-th ion and it was set equal to unity for all ions in strings containing up to 20 ions. The $\Delta\phi_j$ represents the relative phase shift of a particular j-th emitter, clearly dependent on the angle of the incident laser beam $\theta_{397\text{-M}}$, the angle of the observation direction θ_{obs}, the wavelength

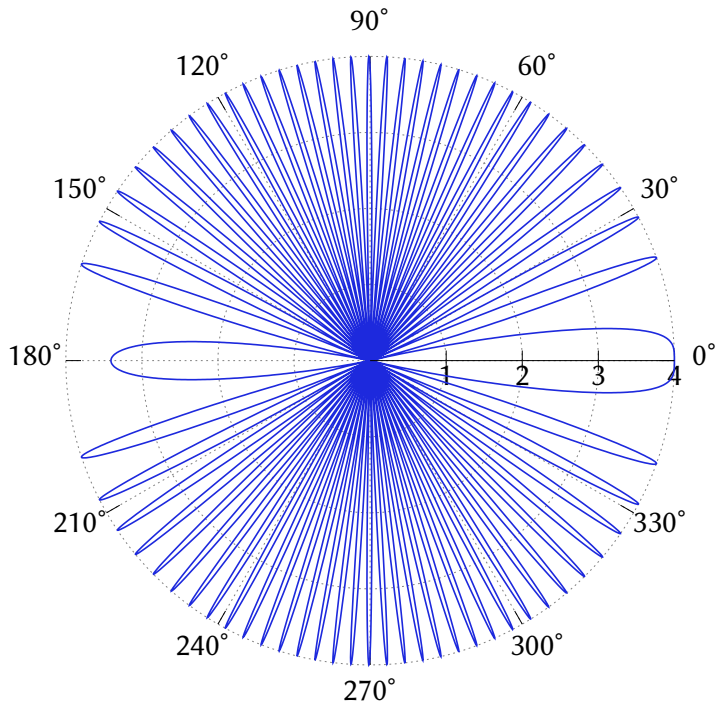

Figure 4.7: The calculated interference fringes produced by two ions are plotted in the far-field, the angle of an incident laser beam is $\theta_{397\text{-M}} = 45.24^\circ$ (134.76°) to the axial line containing both point-like ions. The interference pattern is plotted as a function of the observation angle θ_{obs}, see Fig. 4.5. The mutual distance of ions is 6.72 µm, which correspond 480 V applied to the tip electrodes in our trap.

of coherently scattered photons 397 nm, and the position of j-th ion. The first three mentioned were constant during measurements and only the positions of ions in harmonic potential were tuned through the voltage U_{tip}, see the section 2.1.3. The resulting curve is an ideal interference pattern I_{coh} established by fully coherently scattered photons and was rescaled to match the observed intensity using equation

$$I_{\text{obs}} = I_{\text{incoh}} + \kappa \cdot I_{\text{coh}}, \tag{4.5}$$

where I_{incoh} is the offset and κ is used to rescale the amplitude of the interference pattern. The I_{incoh} is formed by the incoherent contribution of scattered light and background count rate. The background was precisely measured before or after of each interference measurement for 200 s and deducted in the final graphs, only two-ion case Fig. 4.6 contains it for illustration. We do not calculate the incoherent contribution as in the previous two-ion case because of the complexity of the motional decoherence mechanisms. It growths rapidly with a number of modes, which is dependent on the number of ions. The portion of inelastically scattered

photons remains the same as in two-ion interference, while the magnetic field and laser cooling parameters remain the same.

The fits of the measured interference patterns with fitting parameters I_{incoh} and κ are shown as a solid blue line. The measured interference patterns for 3, 4 ions are shown in the Fig. 4.8. The intensity is plotted again as a function of voltage U_{tip}, but now the axis is linear in voltage despite the two-ion interference Fig. 4.6, where the linearization with respect to the parameter $d_{2\text{ion}}$ was used to obtain the harmonic fringes.

The Coulombic potential in the axial direction distributes the ions nonuniformly for more than 3 ions. The three-ions still have the uniform distribution

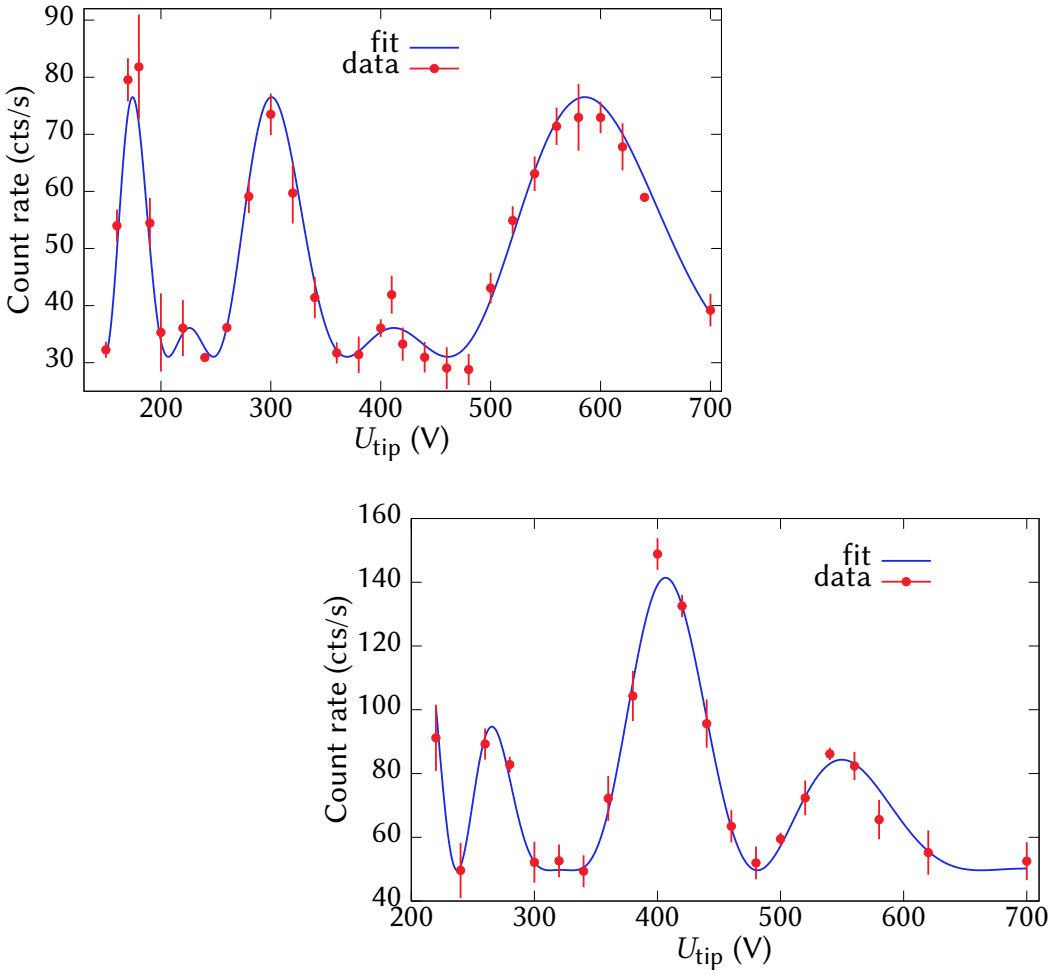

Figure 4.8: The graphs present the observed interference patterns from 3 and 4 ions. The red dots correspond to the measured data and the solid blue line is calculated interference pattern, which amplitude and offset were fitted to experimental data.

and the maximal points of interference were found approximately at 170 V, 300 V, 600 V. The three maximal peaks correspond to the cases when all three ions contribute to the interference constructively. In the picture are also two smaller peaks localized between the neighbouring maxima, the two peaks correspond a situation, when the adjacent ions contribute destructively, the phase shift between them is $\pi \cdot (2n + 1)$, still the outermost have the phase shift exactly twice as large $2\pi \cdot (2n + 1)$ and contribute constructively.

For four and more ions, the configuration of fully constructive interference of all ions positioned in the Coulombic potential does not exist. There is only a possibility to reach partial constructive interference, which can almost reach the value of the fully constructive interference, but this is likely only for crystals with a small number of ions.

For an illustration of interference curves of equidistantly distributed emitters, we calculated the interference curve in the same way as for the presented configuration in the experiment but with uniformly distributed emitters, see the

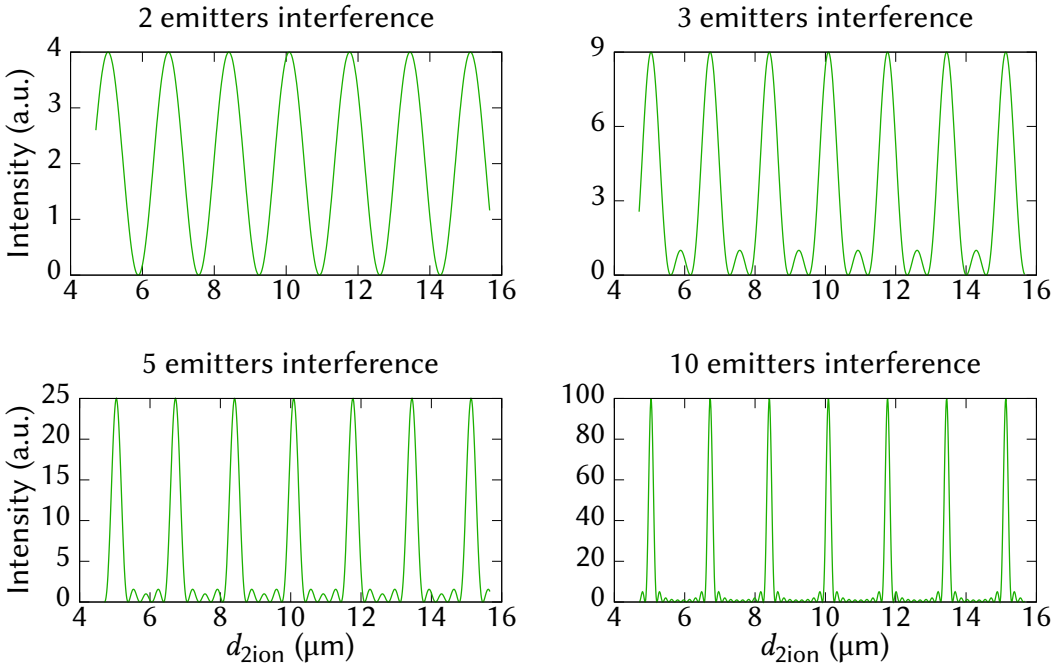

Figure 4.9: The solid green lines present the interference curves calculated in the same way as for ions in the trap, the single difference is the equidistant distribution of the emitters. The graphs include simulations from 2, 3, 5 and 10 fully coherent emitters with normalized amplitude to unity, therefore the maximal interference scale as N^2. The horizontal axis is linearized to two-ion distance d_{2ion}.

Fig. 4.9. The interference patterns are plotted as a function of inter-ion distance and without background and decoherence mechanisms. The maximal constructive interference is periodically reached with the expected value scaled as N^2, where N is the number of emitters plus the amplitude of each emitter is set to unity. Between the maximal interference peaks are smaller peaks and their number scales as $N - 2$.

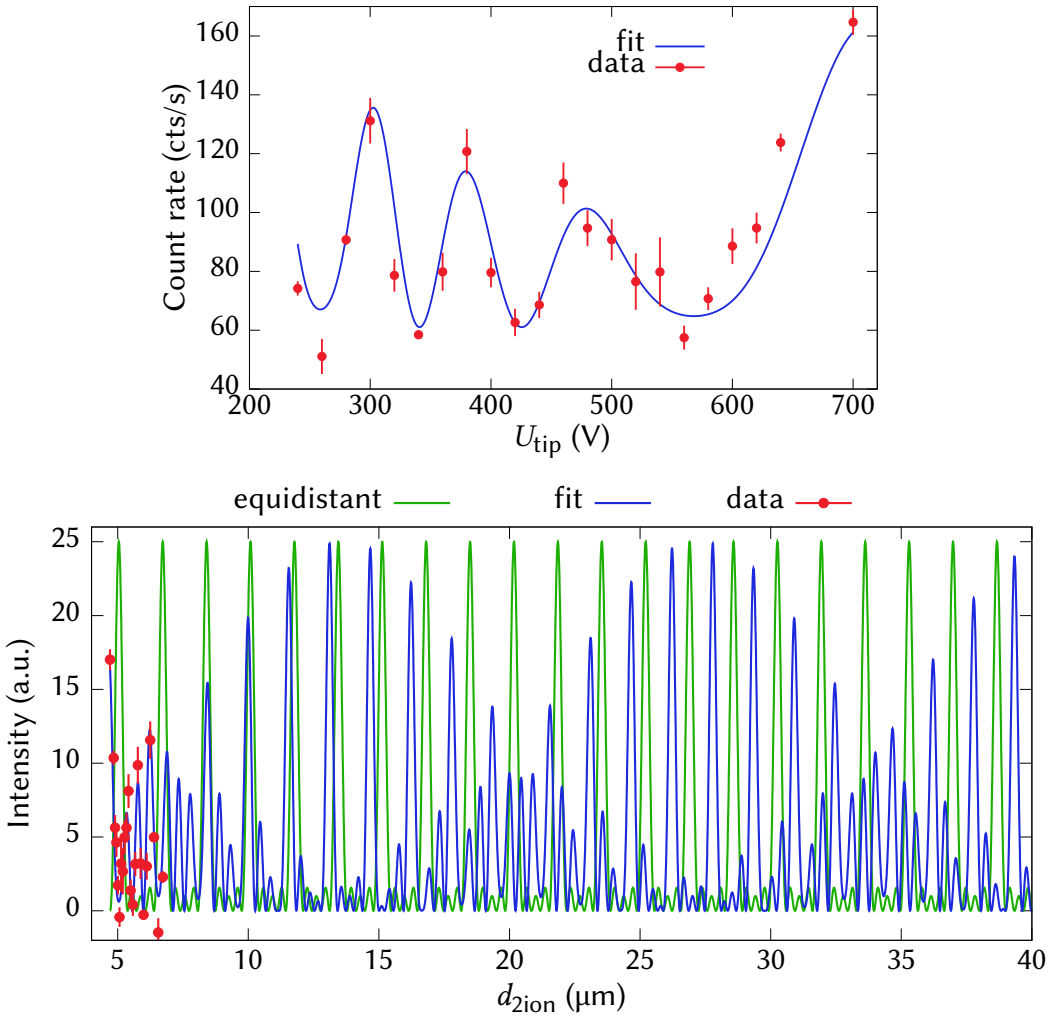

Figure 4.10: The graphs present the observed interference patterns from 5 ions. The red dots constitute the measured data, which were fitted by the calculated interference pattern showed a solid blue curve. The bottom graph represents the same but the vertical axis is normalized to correspond the calculation with amplitudes of emitters set to unity and the horizontal axis was linearized in terms of two-ion case. The solid green curve corresponds to the interference pattern emitted by equidistantly distributed emitters. The curves were horizontally prolonged.

The five-ion interference is presented in the Fig. 4.10, the upper graph shows the measured data in a obtained range of values with the corresponding fit, on the other hand, the bottom chart includes a prolonged curve of the fit. The fitting curve seems to less fit the measured data for five-ion crystal than other cases, this is caused by lower stability of the crystal due to trap and laser cooling parameters. During the measurement, the crystal had often a tendency to melt. After melting, we detuned the cooling 397 nm laser to the red from employed transition to crystalize the ions. We continued with measurement after setting the 397 nm laser back. The bottom chart in the Fig. 4.10 has a linearized horizontal axis to two-ion distance $d_{2\text{ion}}$. The calculated curves are normalized by setting the amplitude of

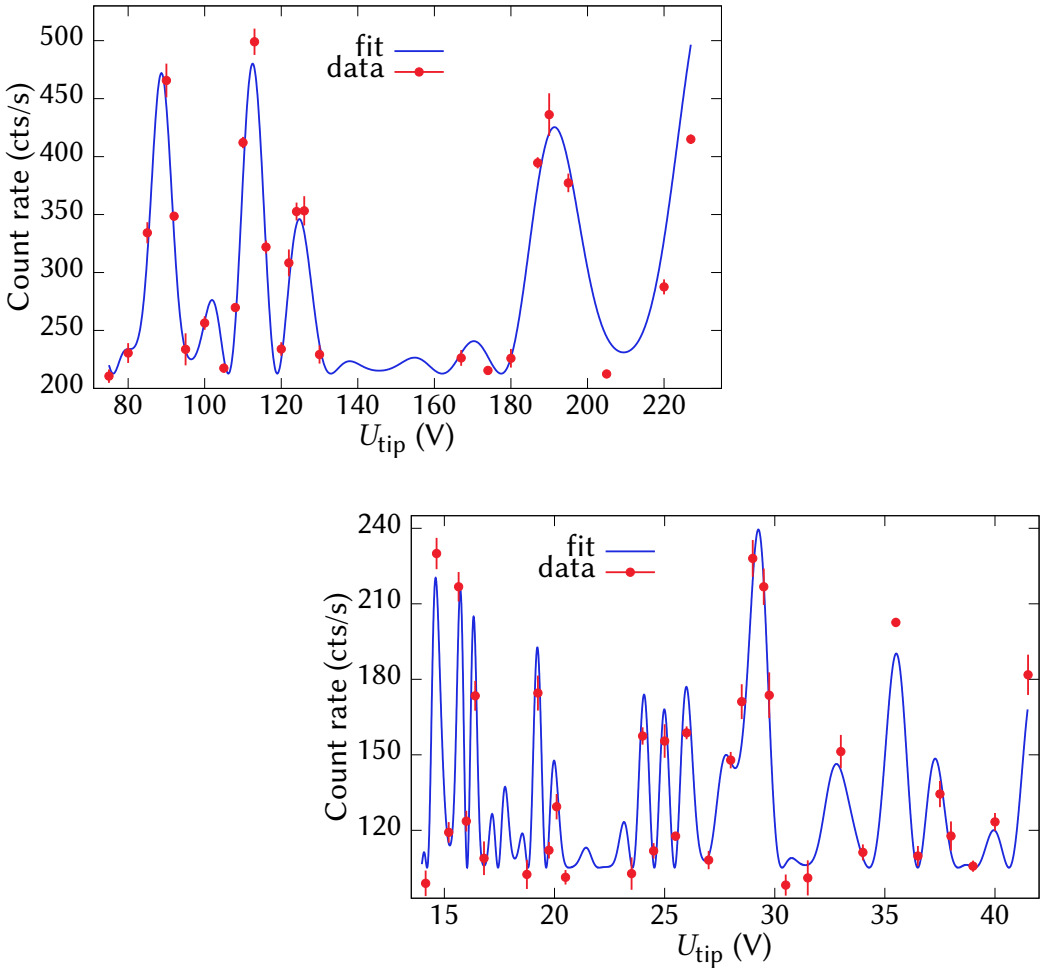

Figure 4.11: The graphs present the observed interference patterns from 10 and 20 ions. The red dots constitute the measured data and the solid blue line is calculated interference pattern, which amplitude and offset were fitted to experimental data.

each emitter to 1. The measured data are rescaled by fit from the upper graph to correspond the normalized curves, the offset is deducted and the amplitude is normalized. The renormalization causes that some measured intensities became negative. The green curve represents the interference pattern of five equidistantly positioned emitters, already shown in the Fig. 4.9. Fully constructive interference occurs periodically in the case. The interference pattern from emitters positioned in the harmonic potential is formed only by partially constructive interference, which for some emitters positioning almost reaches the value of fully constructive interference, but not within the measurable range. In comparison with the theoretically calculated pattern, it is obvious the real measurable voltage range is limited, and the interesting part of interference with high interference peak can lay out of the range.

The experimental range of tip voltages is dependent on a number of ions. The larger crystals have to be trapped at a lower U_{tip} in order to trap the linear chain configuration of ions. For example, the two-ion interference was measured in the larges range of U_{tip} from 75 V to 780 V and the ten-ion interference in the range 75 V to 227 V, and 20-ion interference in the range 14 V to 41.5 V, see the Fig. 4.11.

The measurements with low tip voltages containing more than 20-ion crystals included a positive voltage offset $U_{\text{tip-add}} = 170$ mV in the corresponding simulation for matching the measured interference data. The most probable explanation is the effect of the residual stray fields or patch potentials affecting the trapped ions[77,141].

4.3.3 Many-ion interference

Until now, the amplitudes A_j of all ions were $A_j = 1$, but for long ion strings, we have to take into account the beam profile and the corresponding uneven excitation of the ions. Therefore, the simulation includes the spatial Gaussian modulation of the scattered beam amplitude

$$A_j(z) = A_j(0)\frac{1}{\sqrt{2\pi}\sigma_z}\exp(-z^2/(\sigma_z^2)), \tag{4.6}$$

caused by the spatial profile of the 397 nm beam intensity, where z is the axial position measured from the centre of the trap, $A_j(0)$ is the excitation in the middle of the trap for the purpose of simulation setting equal 1 and σ_z represents the width of the beam projected onto the axial axis. In the measured data for 28, 53 ion strings we used the FWHM=115 µm axially projected 397 nm Gaussian beam diameter resulting in grey fitting interference curves. The corresponding graphs are shown in the Fig. 4.12. This optical restriction was the technical limiting aspect in the measurements with long ion strings, but in the future can be overcome by rebuilding

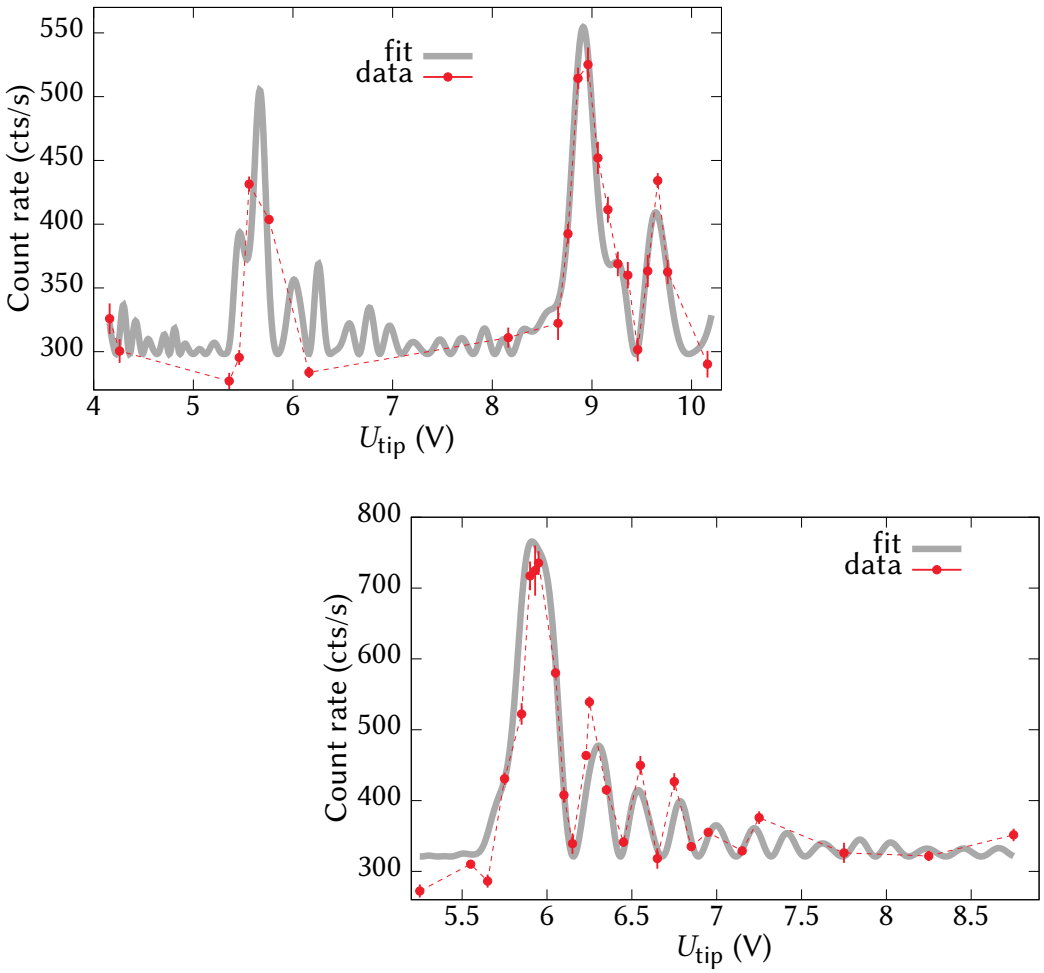

Figure 4.12: The graphs present the observed interference patterns from 28 and 53 ions. The red dots constitute the measured data and the solid grey line is the calculated interference pattern, which amplitude and offset were fitted to the experimental data, the simulation had to take into account the Gaussian spatial beam intensity to fit the pattern plausibly.

the optical path and employing elliptical laser beams, or by the excitation of the more acute angle of incident laser beams.

4.3.4 Contrast of interference patterns

The interference pattern measured from 53 ions contains the interference peak with highest count rate we observed, it is located around 6 V and reaches 735 cts/s on average. The peak has also a higher contrast than some other interference patterns.

In analogy with the two-ion case, we can define the local visibility within the measured range for other interference patterns. The visibilities calculated from the interference data are plotted as a function of the number of interfering ions in the Fig. 4.13.

The visibility for an exact interfering number of ions is calculated in two ways, firstly from extremal measured data points as green triangles and secondly from fitted curves within the measured range of voltages, depicted as blue squares. The neighbouring data points are connected by dashed lines to better distinguish blue and green data sets. The graph shows that the estimated visibilities remain in the range of values 0.34 to 0.53.

It was already mentioned that the measured interference pattern, can be divided into a coherent and incoherent part. The interference minima is defined by the incoherent contribution and for equally contributing ions can be expressed as $N \cdot I_{\text{incoh-single-ion}}$. Meanwhile, the interference minima is regularly represented in every measured intensity graph, the fully constructive interference maxima is observed only in cases with 2 and 3 ions, due to equidistant distribution. For a few ions, the interference maxima formed by partially constructive interference can still reach almost fully constructive interference, but it can not be usually found in

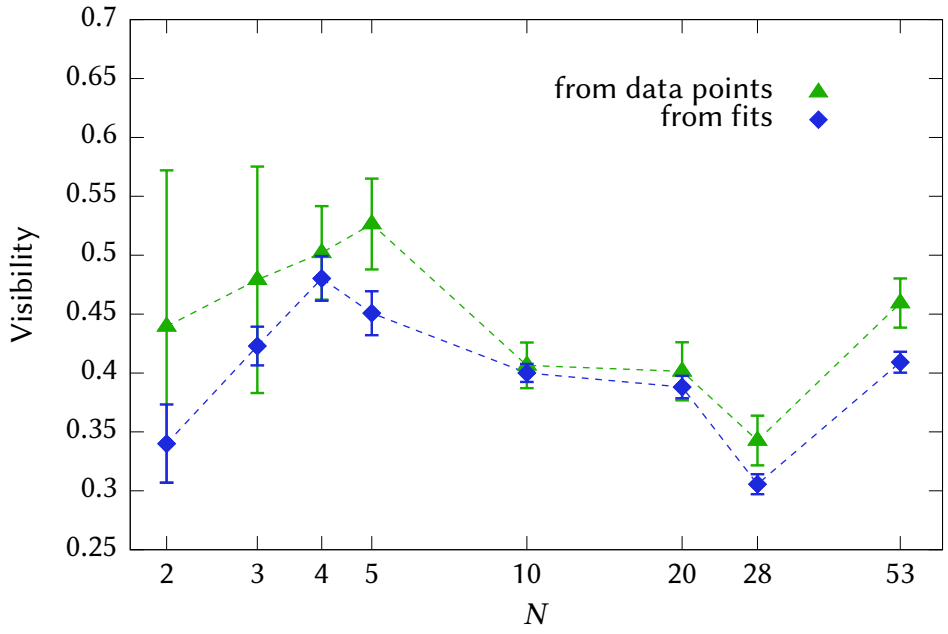

Figure 4.13: The estimated visibilities of measured interference patterns cleaned from the dark counts. The green triangles represent the estimation from measured extremal points, meanwhile the blue squares stand for estimation from fits. The dashed lines connect the neighbouring points to improve the intelligibility of the graph.

the measurable range, see the example with 5 ions in the Fig. 4.10. For more ions it is unlikely to approach the fully constructive interference even more.

On the other hand, the equidistantly positioned emitters would be producing a periodic interference pattern, which repetitively reaches maximal constructive interference with intensity $N^2 \cdot I_{\text{coh-single-ion}}$ for fully coherently and equally contributing emitters. The factor N^2 for coherent addition of constructively interfering waves scales faster than the factor N for incoherent addition, therefore, it is expectable that the theoretical visibility grows with N and goes to the unity at infinity even for partially coherent light.

This growth is evident for 2, 3, and 4 ions in the graph, then the trend no longer continues. The first main reason is the less control over the growing system caused by scaling of the motional decoherence. The second substantial reason is the portion of constructive interference moving away from the fully constructive case with an increasing number of ions. Still, it seems the scaling and trimming factors compensate each other and therefore the measured visibilities remain in the band of values.

We note that the trapping and laser excitation parameters were slightly optimized for reaching sufficiently stable crystals with maximal interference contrast for each number of ions. These gentle optimizations also affected the observed visibilities. We carried out all the measurements in the continuous excitation regime, but the possibility of improving the interference contrast is to employ the pulse excitation. By separating the cooling and probing processes, the contribution of inelastic scattering can be considerably reduced. Furthermore, the motional decoherence effect can be suppressed by utilization of the cooling techniques allowing for reaching lower crystal temperatures.

4.4 Further analysis of the interference from scalable system of ions

The previous section focused on presenting the measured interference patterns and direct consequences. This section focuses on the analysis of the interferometric patterns with respect to the conventional measures of optical phase interference and concerning practical applicability for interferometric sensing. The maximal interference is relevant for directional emission, where the constructive summation of radiation from ions is required to reach a sufficiently high value of emission efficiency in the target direction. The phase resolution is a crucial factor for the sensitivity of interferometric methods. The potential addressability of ions could practically enhance the interference and overcome the limits related to unequal distribution of ions in the Coulombic potential.

4.4.1 Maximal interference intensity

It was discussed that the visibility is heavily affected not only by the partial inelastic contribution and motional decoherence mechanisms but also by a height of the partially constructive maximal interference peak found in the measurable range, as an effect of the non-equidistant distribution of ions in the harmonic potential.

We theoretically analysed the scaling of the height of the partially constructive maximal interference peak as a function of the number of ions up to 20, the result is displayed in the Fig. 4.14. The vertical axis is plotted as the square root of the intensity to improve the readability of the chart. The intensity is the product of the emitted amplitudes, which are normalized to unity for each emitter. The chart contains already mentioned borders inside which has to lay the maximal interference peaks. The bottom border, showed as a dashed red line, is formed by the fully incoherent contribution of emitters and scales as N. The upper border, depicted as a dashed black line, is formed by fully constructive interference of fully coherent

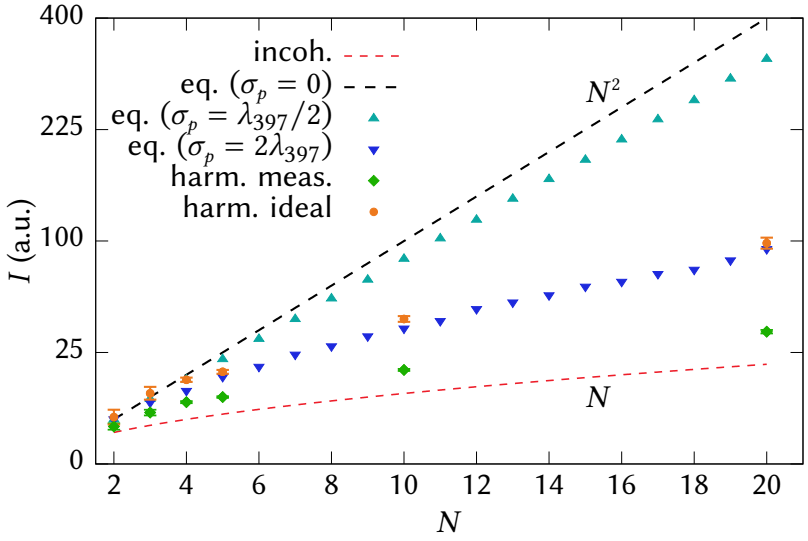

Figure 4.14: The graph shows the maximal intensity of scattered light as a function of the number of emitters with a normalized amplitude of each emitter to unity. The vertical axis scales as the square root of the intensity. The dashed red and black lines represent the limiting case of fully incoherent light and fully coherent light with fully constructive interference, respectively. The green squares and orange dots are the same measured data with recalculated intensities, moreover, the orange dots are corrected from decoherence mechanisms. The triangles were given by simulation with an axially shifted emitters by Gaussian distribution of distance from equidistant positions, the width of the Gaussian shift was $\sigma_p = 2\lambda_{397}$ for teal tringles and $\sigma_p = \lambda_{397}/2$ for blue triangles.

light and scales as N^2.

The green squares represent the measured data, which we renormalized to the amplitude $A_j = 1$ for each ion. The same data were rescaled in the simulation into the fully coherent case, where no inelastic scattering or decoherence mechanism is considered and are depicted as orange circles. The drop from N^2 scaling is caused only by non-equidistant distribution in the harmonic potential and finite tuning range of U_{tip}. The decrease of maximal intensity from a fully constructive case is most apparent for 20 ions, where the value drops from 400 a.u. to approximately 100 a.u., four times less, just by partially constructive summation of amplitudes.

To better understand the situation, we suggest the equivalent simulation with emitters, but with a specific layout. We positioned the emitters equidistantly and then shifted each of them with some random but fixed length, which was given by Gaussian uncertainty with width σ_p. We analysed the maximal intensity for the accessible voltage range in our trap, where the ions remain stable, still, the amplitude of each emitter was set to one. The simulation was repeated 100 times for a set number of emitters and the final maximal intensity was taken as an average from all the realizations to avoid randomness in the final data. The most trivial case is $\sigma_p = 0$, which corresponds to the equidistant case with fully constructive interference corresponding to N^2 scaling. The simulation with width $\sigma_p = \lambda_{397}/2$, showed as teal triangles have scaling of maximal intensity near the upper limit. However, the Gaussian width with the value $\sigma_p = 2\lambda_{397}$, showed as dark blue triangles, produces points where the original equidistant distribution does not play a role anymore. It is equivalent to the fully randomly spread out case of the emitters.

4.4.2 Phase resolution of the interference pattern

The crucial characteristic of interferometric measurement is phase resolution, which is usually a quantitative value of sensitivity. For a very high number of equally spaced emitters, the description leads approximately to the well-known case of the Fabry-Pérot resonator. The previous subsection discussed the distribution of ions in Coulombic potential and how the partial constructive addition of waves affects the interference. On the other hand, the widths of interference peaks are indeed not affected by a portion of the background, the portion of inelastically scattered photons, or other decoherent mechanisms. The shape is solely given by the positions of the emitters.

The analysis of peaks width was made for the highest peak in the measured range of the collected data, shown as an inset in Fig. 4.15. The peaks are taken from the simulations, they are normalized to unity and due to the nonlinear dependency of the interference pattern on the voltage U_{tip}, the fringes were linearized in terms of two-ion distance $d_{2\text{ion}}$, corresponding to the two-ion phase shift $\delta\varphi$. Therefore,

the FWHM width w of peak of two ions is exactly π rad. The maximal peaks for different ion numbers are distinguished by colours, which are the same as in the main Fig. 4.15, where the widths of the estimated peaks are plotted as coloured dots. The interference peaks narrow in width with the number of ions, which is analogous to equidistantly distributed scatterers, nevertheless the plotted peaks are not symmetrical. The estimated widths showing decrease with the number of ions for all measurements. The dependence slows down for 10 and 20 ions, where the widths reach values 0.35π rad and 0.32π rad respectively. The slowdown is caused by the imperfect constructive interference, the same effect, which limits the maximal constructive interference in the local scanning range. Therefore, the phase resolution can be further improved by regularization of the scatterer positions[117,142]. For comparison, we proceed the simulations with equidistantly distributed emitters, their

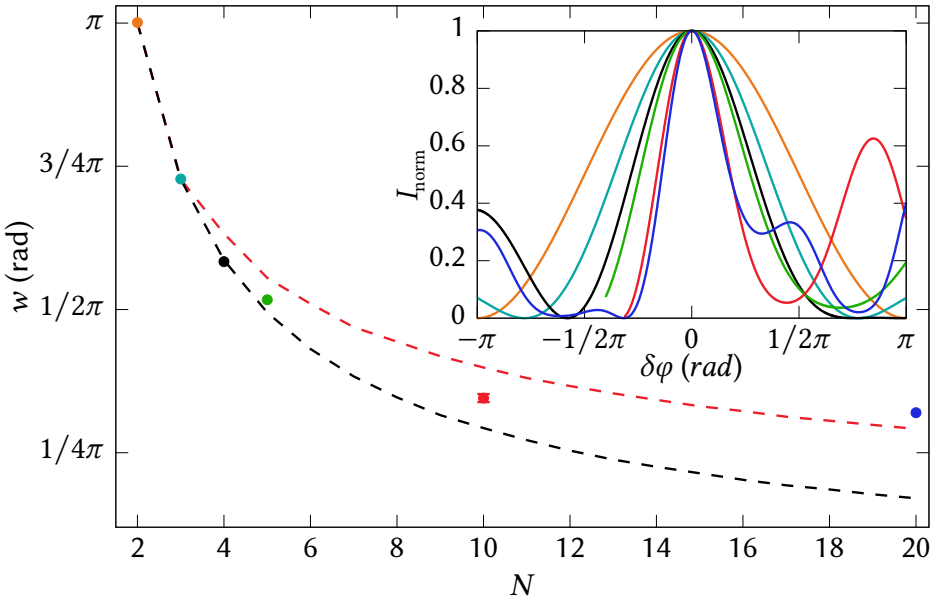

Figure 4.15: The phase sensitivity of interference patterns from ion strings in Coulombic potential. The inset graph shows the shapes of maximal interference peaks from fits in the measured ranges, the intensity of the peaks is normalized to unity and the horizontal axis is linearized to two-ion distance, printed in angular units. The colours correspond to colours in the main graph and mark the number of ions in the crystal. In the main graph, the widths of peaks are plotted as the full width at half maximum (FWHM) w values in angular units as a function of a number of ions, the estimated error bars are below the size of the plotted dots and they are calculated from the tip voltages uncertainty. The dashed black and red lines connect the calculated FWHM widths of 2 up to 20 equidistantly distributed emitters, the calculation was carried out for the smallest as red and the largest as black distances between the neighbouring ions in the Coulombic potential.

distances were taken as the minimal and maximal inter-ion distance between two neighbourhoods in the Coulombic potential. We calculated their peak widths for 2 up to 20 ions and connected them as the dashed red line for the minimal distance in Coulombic potential and as the dashed black line for the maximal distance. The reason the equidistant cases have different peak widths for different inter-emitter distance for more than 3 scatterers is the linearization in terms of two-ion phase shift $\delta\varphi$ distance.

4.4.3 Individual coherent contribution

We chose the example with 20 ions to demonstrate the influence of the individually driven incoherent contribution from the ions on the interference pattern. It is the largest crystal from which we expected the near-equal coherent contribution from all ions, moreover, the interference pattern is well described by the model without Gaussian beam intensity profile.

The most straightforward example can be switching the selected ions fully incoherently emitting, it means the scatterers no longer contribute to the shape of the interference pattern, but solely to the offset of the pattern, which we fit in the model as incoherent intensity I_{incoh}. We set the outermost ions to fully incoherent scatterers in the simulation. Due to symmetry in the crystal, we chose both outermost to amplify the effect. The result of the simulation is depicted as a solid green line in the Fig. 4.16. The data and blue fitting curve are the same as in the Fig. 4.11 and the black curve represents the fit of simulation where we switched the two innermost ions to fully incoherent scatterers. They are also symmetrically positioned due to the even number of ions in the crystal. When we compare these cases, we find that they are distinctly different from each other, with the constructive peaks differing in amplitude, position, and noticeably also in their shape. The majority of green peaks are suppressed, but the left one nearly at 15 V is enhanced and some remain the same. Importantly, the simulated curves with incoherent scatterers do not reproduce the measured data anymore, this is most apparent in the middle of the interference pattern.

Note here that making the outermost or other ions incoherent is different from situation putting them out completely from crystal because the taking off results in a rearrangement of ion positions in the Coulombic potential, which is a completely different case.

The mentioned adjustments rather impair the simulated interference pattern, but the same idea can be experimentally used to improve some peaks. For example, a target peak can be enhanced by banning of the scattering from ions, which contribute out of phase. It can be done by population transfer to long-lived levels. Another possibility is to trap a very long ion string, where central ions have a

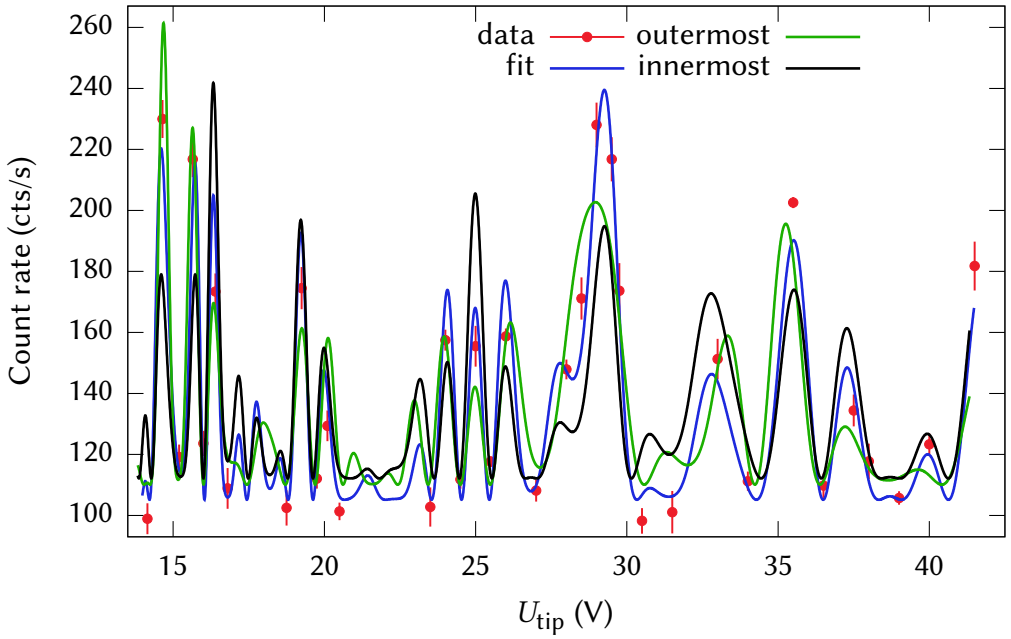

Figure 4.16: The graph displays the interference pattern observed from 20 ions, it shows the simulation and impact of switching some ions scatter fully incoherent light. The measured data are shown as red dots and the solid blue line is the best fit of the calculation, where all 20 ions contribute equally coherently, on the other hand, the green and black lines represent the best fits of calculation with the model corresponding to two outermost and two central ions scattering fully incoherently, respectively.

nearly uniform distribution. The equidistant case can be then approached by addressing only the central part by a narrowed laser beam. Addressing of individual ions could indeed represent a powerful tool, how to compensate the nonuniform distributions of ions.

A more realistic situation corresponds to the smooth modulation of the scattered portion of coherent light from ions along the whole crystal. The most likely situation is when the portion of coherently scattered light continuously declining from the centre of crystal to the edges as the outer ions are less restricted in the Coulombic potential and therefore the amplitude of their motion is higher. We implemented the Gaussian distribution of the coherent contribution from ions into the simulation and fitted the measured data from 20 ions again. The result is printed as a solid green line in the Fig. 4.17. The Gaussian modulation is a function of distance from the centre of the trap, where it is set fully coherently and fall to the edges, where the outermost ions contribute only by $1/e$ portion of the coherent light. The simulation affects the shape of the interference pattern

noticeably, furthermore it does not sit on the measured data. This further supports the claim that ions contribute nearly equally to the interference pattern. It seems the situation with Gaussian modulation is the same as in the example with 28, 53 ions where we have to add into simulation the Gaussian modulation of ion excitation. However, the beam width does not change during measurement and the spatial length of the crystal does, so the individual ion excitation also changes as a function of the crystal extension.

To demonstrate also the less likely situation, we modulated the outermost ions to contribute fully coherently and the modulation falls at the centre to the value $1/e$ of coherent light with inverted Gaussian modulation. The fitted curve is shown as a solid black line in the Fig. 4.17. Again, it leads to the situation when the observed data are not plausibly reconstructed.

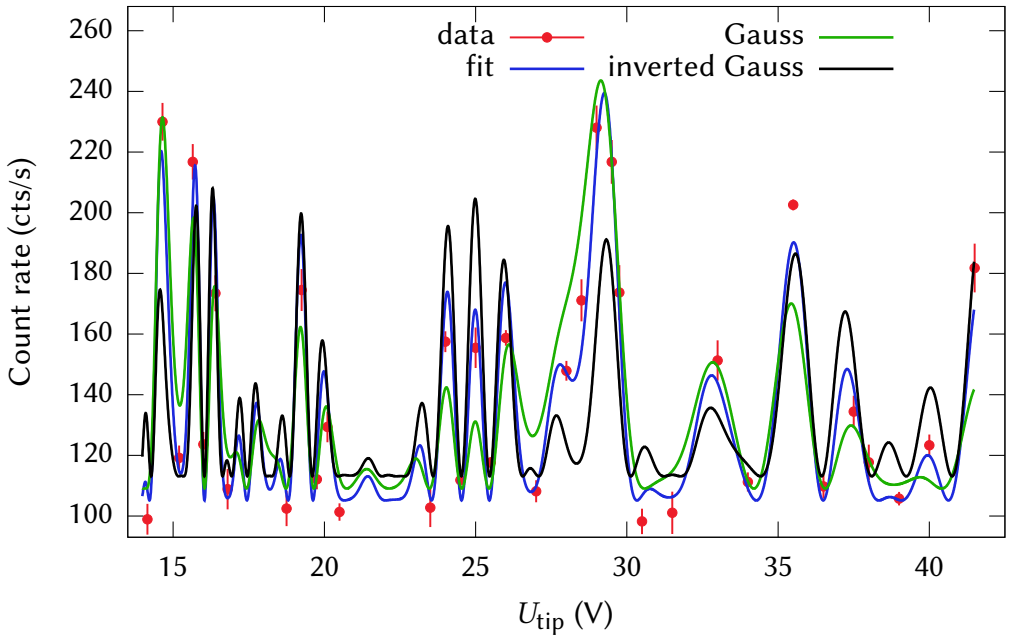

Figure 4.17: The chart shows the interference pattern produced by 20 ions, it presents the simulation and impact of continuous modulation of the portion coherently scattered light from ions. The measured data are shown as red dots and the solid blue line is the best fit of the calculation, where all 20 ions contribute equally coherently, in opposite, the green line represents the best fit of the calculation, where the coherent contribution is modulated by a Gaussian function. In detail, the outermost ions scatter $1/e$ portion of the coherent light while the modulation is set to unity at the centre of the crystal. The black line stands for inverted Gaussian modulation, where the outermost ions scatter fully coherently, while in the centre the modulation drops to $1/e$ coherent contribution.

The simulations underline the high sensitivity of the interference pattern to the contribution of individual ions and pave the way for possible applicability of coherent scattering for long ion strings trapped in the harmonic Coulombic potential.

4.5 Summary

This chapter summarized the experiments concerned with a coherent scattering from long strings of trapped ions. The two-ion case was studied in detail the sources of decoherence were analyzed and implemented into the simulation, which predicted the measured intensity data precisely. The interference fringes were measured from linear chains containing up to 53 ions, and the simplified simulations fit the data plausibly. To authentically reproduce the measured interference patterns for 28, 53 ions, we had to employ a simulation with finite excitation beam width to include the non-uniform ion excitation. The observed interference patterns demonstrated the coherent light interaction from many individual quantum scatterers, which are possibly individually addressable. Other experiments have been limited to very few emitters by the geometry of their setup or by the degree of control of employed quantum scatterers[35–38,119].

Chapter 5

Nonclassical light emitted by ion crystals

The chapter summarizes our studies of nonclassical light observation from large ensembles of single-photon emitters. The large ensembles of trapped ions proved to be a reliable platform for such a test due to high control and long time stability of the system. The nonclassicality was observed in the continuous and pulsed regime, where each of these regimes constitutes a conceptually different source of light. The main parts of the chapter were published by the author and colleagues [A3].

5.1 Introduction

In the section 2.4, it was introduced that the single ion equipped by discrete energy levels emits single photons, therefore, the radiation is always nonclassical, due to impossibility to describe it by a mixture of classical waves[B1]. The disappearance of nonclassicality is generally attributed to the interaction with the environment in the real world.

In pursuit of observing the nonclassical light from a high number of emitters, the experimental arrangement has to fulfil requirements corresponding to the stable number of emitters with stable radiation parameters, tolerance to some portion of thermal noise of background, sufficient coupling efficiency within a feasible time of measurement[1].

The trapped ions in Paul trap match the crucial requirements to observe the nonclassicality from large numbers of ions[1,143]. The extremely long lifetimes of crystal on the order of several days offer the opportunity to observe nonclassical character even from huge ion crystals[144–147]. Due to the simple lambda-type electronic level structure and perfect isolation from outer environment the nonclas-

sical fluorescence from single-atoms were observed[148,149] long ago. The technical progress led more recently to the demonstration of single-photon sources with single trapped ions, which presented high coupling efficiency[150], high-rate production of single-photons[42], and unprecedented parameters in purity[41]. Importantly, the platform of trapped ions advantages from an inter-atomic distance larger than the wavelength of emission caused by the Coulombic repulsion and therefore the collective effects[151] can be mostly neglected. On the other hand the repulsion increases size of crystals, which aggravate the coupling efficiency from such large object. Still the number of ions is precisely known and can be almost deterministically set by gradual ion-loading process.

5.2 Experimental setup

The section goes through the experimental measurement description of nonclassical light emitted of a large number of ions. The technical parameters and limitations are discussed.

5.2.1 Experimental configuration

The simplified experimental scheme of the setup is shown in the Fig. 5.1. The $^{40}Ca^{+}$ ion crystal is Doppler cooled by 397 nm and 866 nm lasers, the polarization is perpendicular to the radial observation direction. The static magnetic field $\approx$ 12 Gauss is applied in the radial observation direction. The radiation is collected by a high NA lens L_O.

The flip mirror in up position reflects the image of ions onto EMCCD camera. The radiation comes into HBT measurement configuration when the flip mirror is tilted. The camera serves for ion number estimation, spatial analysis of the crystal, and setting the homogenous excitation across the whole crystal in the experiment. In all experiments, the camera is equipped by an interference filter (IF) to transmit the 397 nm radiation. This experimental configuration for measurement of nonclassicality has other IF in the collection path and also on each APDs (Countseries, Laser Components). The APDs have a free-space-coupled design, which is more open than fibre version, therefore, the additional IFs are used to reduce the scattered background light. The light in the laboratory was shut down during other experiments, but especially in this measurement of nonclassicality, we had to reduce the in-room light on the minimum and covered half of the collection path by tubes or beam stops. The light is split by a 50:50 beamsplitter (BS) and the overall coupling efficiencies of scattered radiation were estimated as 0.033% and 0.028% on APDs from single ion positioned in the focus of the coupling lens, the estimation was done in the pulsed sequence described in section 5.3.2.

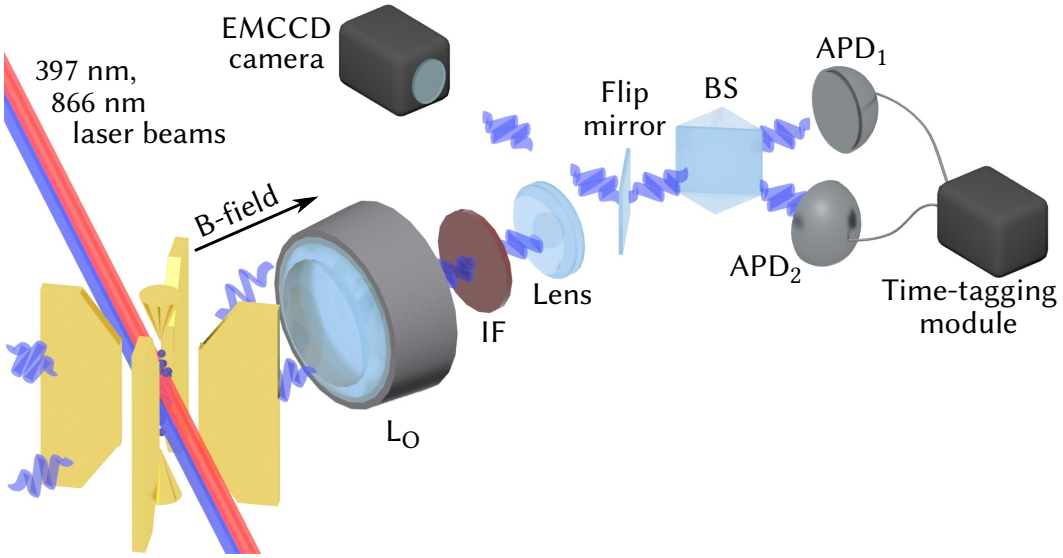

Figure 5.1: The illustration of the experimental setup. The ions are trapped in the linear Paul trap and driven by 397 nm and 866 nm laser beams. The fluorescence is collected by a high numerical aperture lens, in the same direction, the static magnetic field is applied to lift the degeneracy of states. The flip mirror can reflect the image of ions onto EMCCD camera, otherwise, the radiation comes into HBT setup formed by beam-splitter (BS), a pair of APDs and time-tagging recorder.

5.2.2 Optical access

The optical design employes the high NA objective with the object focal length ≈ 66 mm. The collection through the vacuum window induces spherical aberration, which is included in the design of the objective and the objective correct it. The rest of the imaging system includes the 400 mm plano-convex lens and the APDs. The manufacturer specifies about 100 µm surface diameter of nearly equal detection efficiency for APDs.

The measurements of nonclassical light focus on observing it from the largest number of ions as possible, which can be limited by several practical limits like trapping conditions, collection efficiency, or strong background noise. The collection efficiency showed itself as the most problematic. The tests of nonclassicality demand a large set of data[1], this put requirement on high coupling efficiency, otherwise the measurement time grows rapidly. Prolonging can lead to complications of measurement due to higher requirements on the stability of setup and the stability of crystal. The used coupling lens is sufficient from the point of view of collection efficiency, but on the other hand, the small field of view causes the rapid fall of the coupling efficiency for radially displaced emitters. The limited field of view of the whole optical arrangement sharply restricts the effectively observable area.

We measured the decrease of detection efficiency for a single ion displaced in radial and axial observation directions. The measurements are depicted in the Fig. 5.2. The directions correspond to the radial plane of the ion trap and the shift of the single ion was done by applying a static voltage on compensation electrodes. The data are normalized to the maximally measured value, which is located in the

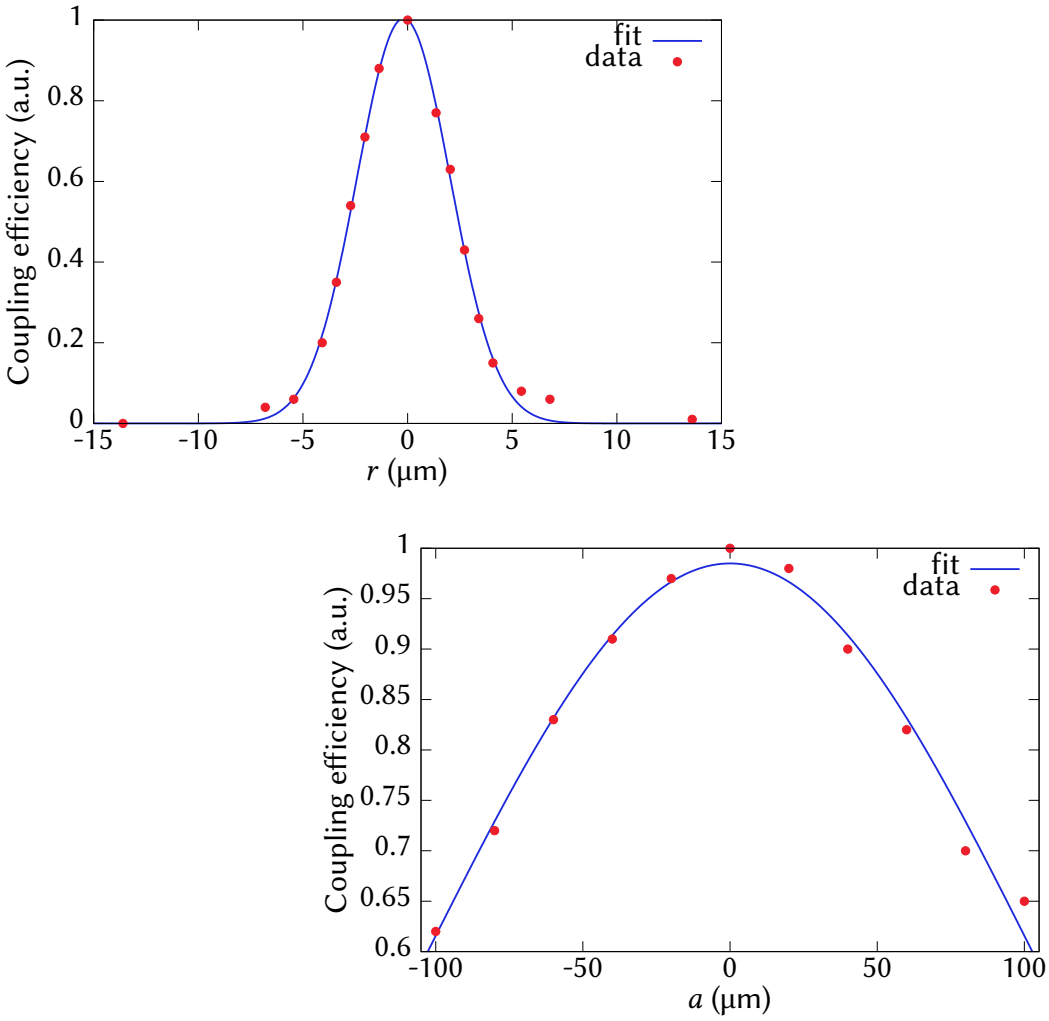

Figure 5.2: The measured and fitted detection efficiencies of different emitter displacements for the employed optical arrangement, the data are normalized to the maximally measured value. The top chart corresponds to the single ion shift in the radial direction and the fitted Gaussian FWHM equals to 5.2 μm. The bottom graph represents the single ion shift along the lens axis and the fitted Gaussian FWHM is 243 μm. All data are estimated in the pulsed excitation regime.

centre. The efficiency profile is fitted by Gaussian function, which fits the data except for the radially displaced ion where the efficiency does not fall so rapidly for a distance higher than 5 µm from the centre. The estimated FWHMs of Gaussian fits are 5.2 µm in the radial direction and 243 µm in the axial direction. The coupling profile is fitted by Gaussian function as sufficient approximation for employed objective[28].

This analysis leads to the answer of how efficient the individual ions are coupled. When we sum the measured particular APD efficiencies, we get the total detection efficiency $\eta_0 = 6.1 \cdot 10^{-4}$ for the ion positioned in the object focal point of the detection optical setup. The assumed Gaussian profiles of smooth data in both directions give us the positional dependency of efficiency

$$\eta(r, a) = \eta_0 \cdot e^{-\frac{r^2}{2\sigma_r^2} - \frac{a^2}{2\sigma_a^2}}, \tag{5.1}$$

where r is the distance from the optical symmetry axis and a is the distance from the object focal plane. The fitted Gaussian uncertainties evaluated from FWHM values equal to $\sigma_r = 2.2\,\mu\text{m}$ and $\sigma_a = 103\,\mu\text{m}$.

The strong coupling restriction in the radial observation direction forced us to optimize trap parameters in order to squeeze the ion crystals into the most compact shape before measurement, but still with a request of maximal stability of the ionic ensemble. The configuration evidently corresponds same secular frequencies, specificaly $f_x \approx f_y \approx f_z \approx 778\,\text{kHz}$ for crystals containing more than 12 ions, the measurements with less and equal than 12 ions are more restricted in the radial direction, the frequencies are $f_x \approx f_y \approx 1341\,\text{kHz}$. The crystals in symmetrical potential are spherical with concentric shell structure[144,145,147,152], which is the most apparent from the largest measured crystal consisting of 275 ions, see the Fig. 5.3.

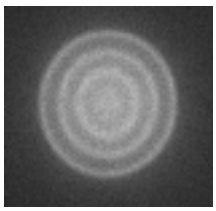

Figure 5.3: The image of 275 ions in symmetrical trapping potential, the picture was taken by the EMCCD camera. The diameter of the crystal spatial extension is approximately 66 µm.

The spatial distribution of the crystal underlines the technical limit on further scaling of the number of emitters within the employed optical detection setup. The Fig. 5.4 shows scaling of count rates from nonclassical measurements for particular crystals. The measurements were performed in the pulse regime described

in section 5.3.2. The detection efficiency scales reasonably for crystals up to 55 ions. Beyond that, ions are placed into higher and higher shells with significantly lower coupling efficiency. The outer shells are coupled well only in limited volume around the axial observation axis, and further adding of the ions have a lower impact on the increase of the count rate.

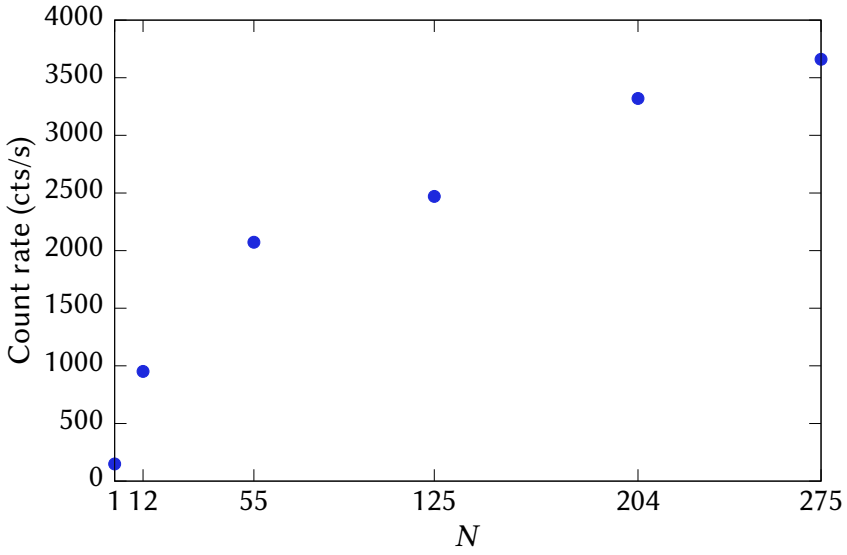

Figure 5.4: The measured count rate as a function of the number of ions in the trap. The data were estimated from nonclassical measurements executed in pulsed regime.

5.2.3 Nonclassical criterion and data processing

The sufficient condition on nonclassical light[1] is employed in terms of the probability P_0 of a no-click of the selected detector and a no-click of both detectors P_{00} in HBT detection arrangement. Then the sufficient criterion for the nonclassical state, marked as distance d, has a form

$$d = P_0 - \sqrt{P_{00}} > 0 \tag{5.2}$$

Note the distance d has not got the meaning of some quantitative value of nonclassicality, it is just a suitable sufficient witness for large nonclassical states. The inequality itself is derived for the symmetric case of both detectors, nevertheless, it can be rewritten for an asymmetric situation, which covers the realistic circumstances with an imbalanced beam splitter or different detection efficiencies of detectors. The condition can be expressed for a known imbalance T into criteria for

particular detectors as[1,143]

$$\begin{aligned} P_{01} &> P_{00}^{T}, \\ P_{02} &> P_{00}^{1-T}, \end{aligned} \tag{5.3}$$

where P_{01} and P_{02} represents a no-click of the first and the second detector, respectively. Then the state is nonclassical if at least one of the criterion is satisfied. The disadvantage of it is the required knowledge of the parameter T with high precision. The practical usage is to multiply the left and right sides of the criteria, which excludes the parameter T and the inequality is $P_{01} \cdot P_{02} > P_{00}$. It is clear that if the inequality is satisfied then one of the inequalities (5.3) is also satisfied, which guarantees the nonclassicality. The distance is then redefined as

$$d_{\mathrm{g}} = P_{0\mathrm{g}} - \sqrt{P_{00}} > 0, \tag{5.4}$$

where $P_{0\mathrm{g}}$ stands for the geometric mean

$$P_{0\mathrm{g}} = \sqrt{P_{01} \cdot P_{02}}. \tag{5.5}$$

The photons are detected by APDs and arrival times are recorded by module (Picoharp300, PicoQuant) with a time resolution of 4 ps. The Fig. 5.5 illustrates the stream of impinging photons on the detectors, which are postprocessed in the PC. To deal with the continual arrival times, the artificial time bin with defined length

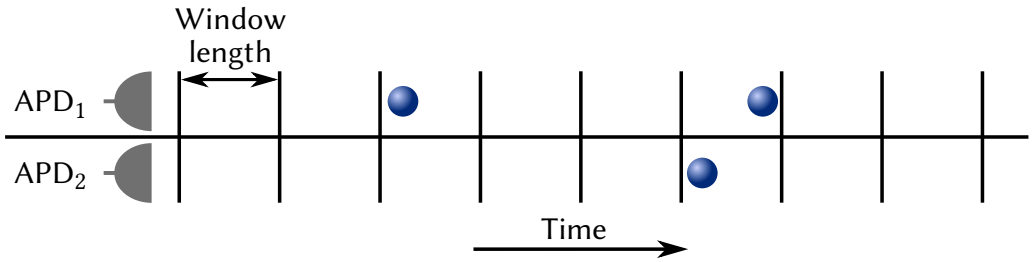

Figure 5.5: Stream of photons impinging onto the detector APD_1 and APD_2. The arrival times were evaluated inside the time bin with defined length.

has to be defined. Then the different events happening inside each window are counted. From the stream of arrival times, we evaluate a number N_{S1} of single clicks on APD_1, equivalently N_{S2} for APD_2, also a number N_{C} of clicks of both detectors within the same window and finally the total number N_{TB} of all time bins of the window length τ in processed measurement. From the numbers of particular events, the evaluation of the probabilities P_{00} and P_{0k}, where k is 1 or 2, is straightforward using the relations

$$P_{00} = \frac{N_{\mathrm{TB}} - N_{\mathrm{S1}} - N_{\mathrm{S2}} - N_{\mathrm{C}}}{N_{\mathrm{TB}}}, \tag{5.6}$$

$$P_{0k} = \frac{N_{TB} - N_{Sk} - N_C}{N_{TB}}. \tag{5.7}$$

The probabilities are finally put into the equations (5.5) and (5.4) to estimate whether the data meet the sufficient condition of nonclassicality with the chosen time-bin length. The error bar of the distance d_g is evaluated statistically by dividing the measurement into five time-equal length parts, from which the distance was estimated independently.

5.3 Measurements of nonclassical light

The measurements of ion fluorescence were carried out in the continuous and in the pulsed regime. Both cases represent different sources of light. The experimental aim was to observe large nonclassical states. All tests of nonclassicality were performed from data sets corresponding to five hours long measurements.

The particular measurement started with trapping an approximate number of ions after that we axially extended the crystal to count the exact number of ions one by one. Before fluorescence measurement, we constricted them to a nearly symmetrical shape, see the Fig. 5.6. After all measurements, we stretched the crystal to

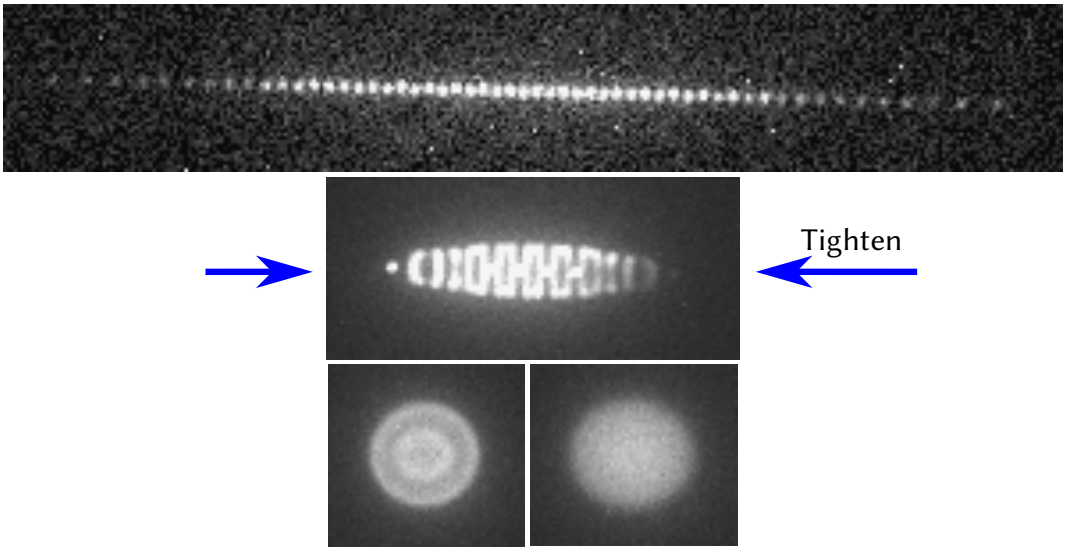

Figure 5.6: The images of crystal containing 55 ions taken by EMCCD camera. The upper picture shows the extended crystal appropriate to count the number of ions. The middle image illustrates the process of squeezing. The bottom pictures represent the shape of the crystal in symmetrical trap potential, the left one illustrates the shell structure, the right one is in more chaotic/plasma state.

precisely count the number of ions again. During the final series of measurements, we had to discard 2 out of 14 measurements, which was most probably caused by rare frequency instability of cooling laser in our setup.

5.3.1 Continuous regime

The regime is defined by continuous excitation of ions by 397 nm and 866 nm lasers. The 397 nm photon emission is detected. The processing was done by time binning the arrival time of photons as it is illustrated in the Fig. 5.5. The window length has to be in this case optimized with respect to the decay of the transition upper state. The Fig. 5.7 shows processed photon arrival correlations as a function of time delay between both APDs. The one-hour measurement with single ion resulted in intensity correlation function $g^{(2)}(0) = 0.064$ for 1 ns length of the time bin.

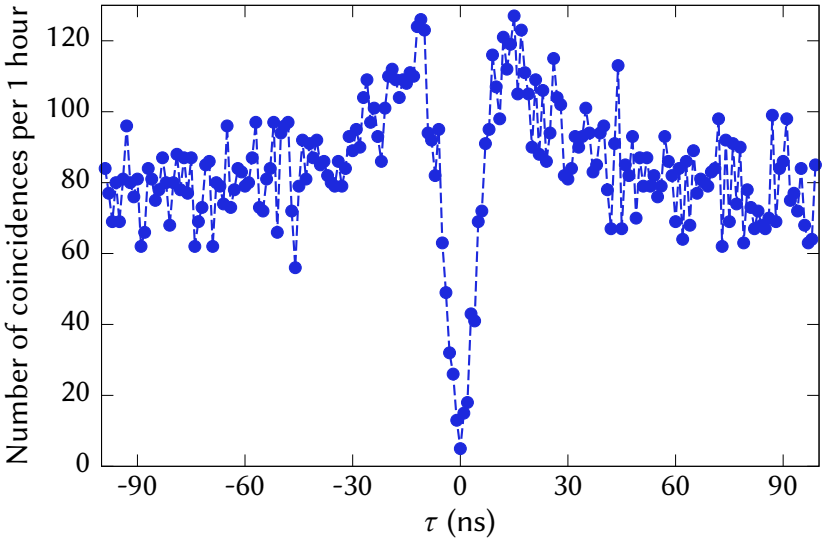

Figure 5.7: The measured intensity correlation function for a single ion in the continuous excitation regime. The data were processed for 1 ns time bin from one-hour data set, and the corresponding $g^{(2)}(0) = 0.064$.

We evaluated the witness value d_g by time binning and processing the raw time arrival data by the procedure described in the subsection 5.2.3. The estimated distances are plotted in the Fig. 5.8 for a few up to 275 employed ions. The data are plotted with a single standard deviation. The standard deviation was evaluated by dividing the whole measurement into five intervals with the same length, and the deviation was obtained from statistics of the five values of d_g. The window length was optimized to get the best ratio of distance d_g and its error bar for single ion and for 275 ion crystal, the compromise of 32 ns time-bin length was chosen.

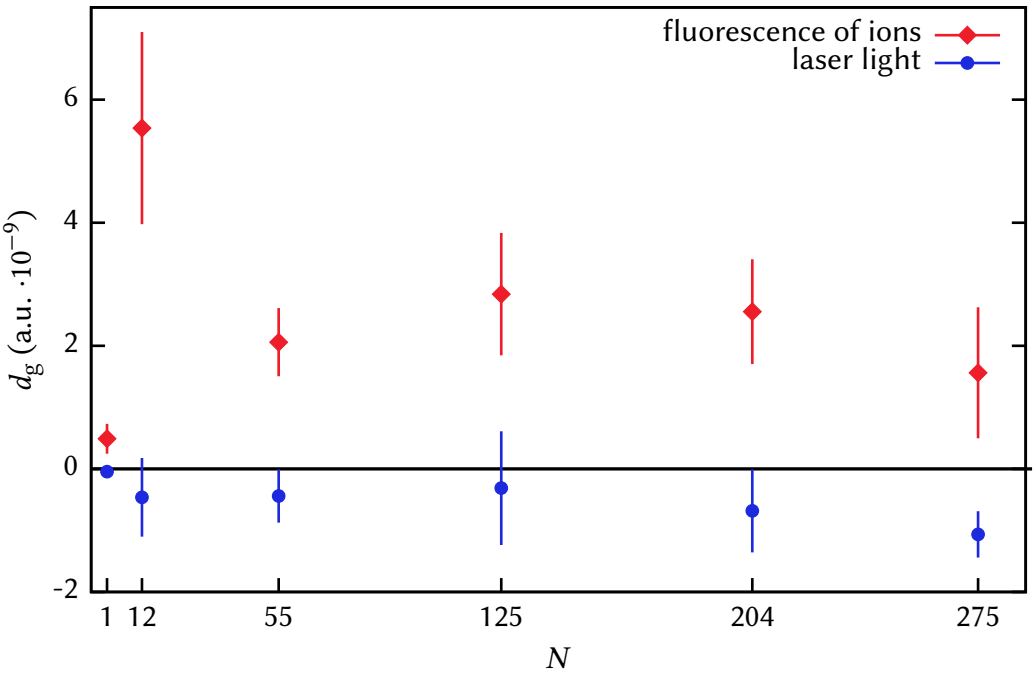

Figure 5.8: The estimated witness of nonclassicality d_g as a function of the number of ions for the fluorescence of ions continuously excited and for the coherent light beam with the corresponding detected count rate depicted as red squares and blue circles, respectively. The chart presents clear separability of the nonclassical ion fluorescence from a coherent laser light. The error bars are shown as one standard deviation.

The blue data points correspond to a measurement check with a coherent laser beam. After measurement of nonclassicality, we kicked the studied crystal from the trap and misaligned the excitation beams to impinge on trap electrodes to reflect into optical detection setup same count rate as in the measurement of nonclassicality. The blue data points are plotted as a function of the number of ions, despite the trap was empty, but the scattered laser light was coupled into the optical detection setup with the same counter rate as in the measurements with the atomic fluorescence. The laser light is the coherent type of light and the distance d_g should be equal to zero or a negative value in case of extra classical thermal noise. That adds another confidence into our nonclassical measurements.

The maximal observed count rate was corresponding to 275 ions, the particular values reached $\approx$ 36 800 cts/s and $\approx$ 31 500 cts/s, which is far from the APDs saturation specified by the manufacturer to about 10^6 cts/s. Specifically, the particular measurement consists of $N_{TB} = 562\,484\,411\,204$ total windows, $N_{S1} = 662\,997\,081$ single clicks on APD_1, $N_{S2} = 567\,105\,311$ single clicks on APD_2 and $N_C = 667\,381$ number of coincidences.

5.3.2 Pulsed regime

The pulsed case employs the same electronic level scheme $4S_{1/2} \leftrightarrow 4P_{1/2} \leftrightarrow 3D_{3/2}$ as continuous excitation regime, however, the laser excitation is applied in pulses. The sequence of the laser pulses with employed lengths is drawn in the Fig. 5.9, which also contains the graph of the measured ion fluorescence intensity within the sequence.

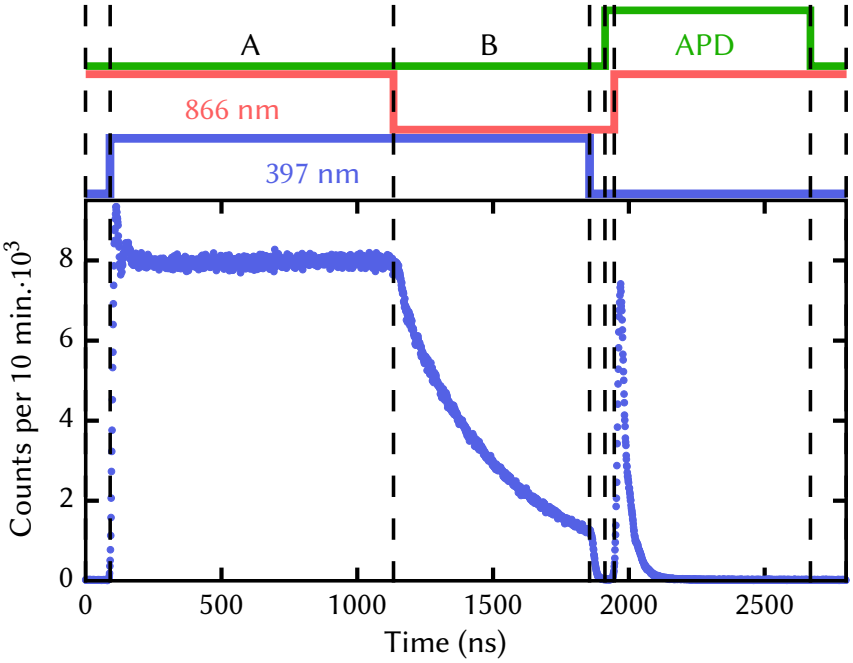

Figure 5.9: The employed pulsed sequence and the fluorescence intensity within it as a function of the sequence time, which is 2800 ns long. The solid green curve represents on/off state of both APDs in nonclassical measurement. The solid red and blue lines present the on/off laser excitation of the crystal by 866 nm and 397 nm beam, respectively. The chart contains fluorescence intensity within the sequence from cumulation over 10 minutes measurement.

The sequence is 2800 ns long and consists of three main parts, namely Doppler cooling, optical pumping of the atomic population to $3D_{3/2}$ state, and detection. Within the Doppler cooling period, both 866 nm and 397 nm lasers are employed to cool the crystal, the section is marked as A. Section B follows by switching off the 866 nm repumper laser beam. The crystal still scatters the 397 nm laser light, but the $4P_{1/2}$ upper level decays with probability 6.4 % into $3D_{3/2}$ metastable state[61], where the population is accumulated due to missing 866 nm repumper beam. The pumping is ended by switching the 397 nm laser excitation off. The remaining fluorescence level corresponds to the population which was not transferred to

$3D_{3/2}$ state. The optical pumping efficiency η_{pump} depends on laser excitation parameters and the number of ions in the trap. We estimated it individually for every specific measurement. The sequence follows by period, where the 866 nm laser excitation is switched on and transfers the population from $3D_{3/2}$ state to $4P_{1/2}$ state. This is followed by spontaneous decay to $4S_{1/2}$ ground state, which radiates at most single photon per single ion, as the multiphoton emission is prohibited[41–43,153]. After the measurement period of the pulse sequence, the 397 nm laser is switched on again and the whole sequence is repeated for a defined number of cycles.

Note that the same pulsed sequence is also convenient for measurement of overall coupling efficiency of light scattered from ions, which we routinely utilize. The detection efficiency is given as an inverse of the number of executed sequences multiplied by the successful detections of photon and corrected by the pumping efficiency η_{pump} of $3D_{3/2}$ state.

The Fig. 5.9 shows the gating of APDs, which are switched on solely in the measurement period of the pulse sequence. The laser beams are switched by acousto-optical modulators (AOMs), which are driven by pulse sequence generation with an unrestricted number of repetitions produced by an FPGA kit (DE2-115, Altera). The APDs incline with small probability to false clicks after gating them on, therefore, they were gated on in advance before triggering the emission and the recorded data of clicks before the emission period were excluded. The emission was localized at the beginning of the detection period, see the Fig. 5.9, and the end part of the detection period after $\approx$ 2.4 µs was removed in order to reduce background accordingly. This post-processing definition of temporal detection mode led to the reduction of recorded clicks by $\approx$ 10 %.

In comparison with a continuous regime, the pulsed regime does not require the time binning of the data, actually, the single sequence defines the single time bin. The technical difficulty is the synchronization of the laser pulses, but also APDs and time-tagging module. The whole experiment driving was done by the single FPGA kit. The most significant advantage of the pulsed regime is the forbidden multiphoton emission within the measurement period of a single sequence. The 397 nm laser excitation beam is also switched off during measurement period, accordingly, it can not contribute to the measured background.

The five-hour-long measurement of single ion fluorescence was processed as a correlation between APDs clicks as a function of time delay between sequences, see the Fig. 5.10. The resulting intensity correlation function correspond to the value $g^{(2)}(0) = 0.036$ in pulsed regime. In comparison with the continuous regime, where the value was $g^{(2)}(0) = 0.064$, the pulsed single-photon source has better quality, and both values are comparable with other realizations of single-photon sources with trapped ions[41–43,153].

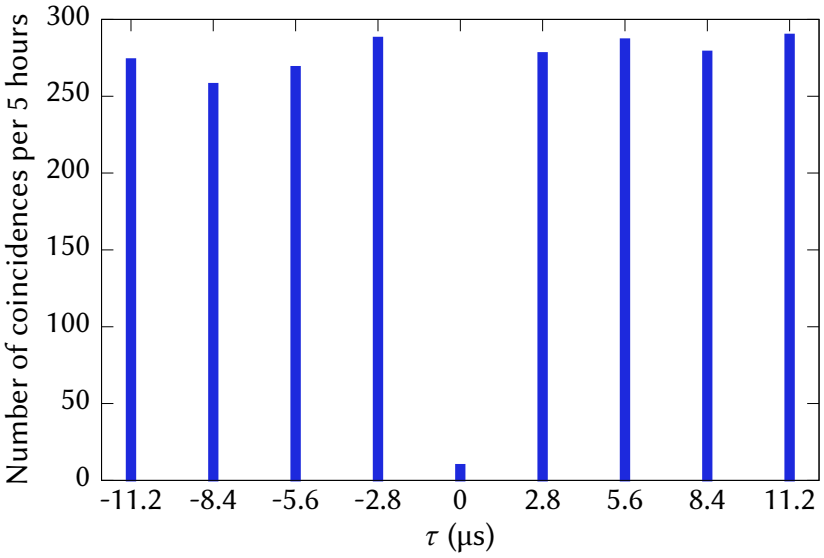

Figure 5.10: The correlation function measured in pulsed sequence plotted as a delay between sequences. The graph was processed from five hours data set of single ion fluorescence, this resulted in $g^{(2)}(0) = 0.036$.

The distances d_g in the pulsed regime measurements were calculated in the same way as in continuous regime, as described in the subsection 5.2.3, the values are plotted in the Fig. 5.11. The red squares represent the measurements with the fluorescence from ions, the blue dots represent laser light. The error bars were obtained again by cutting the total data set into five pieces and the plotted sizes present a single standard deviation. The data were measured for the same number of ions as in the continuous regime, shown in the Fig. 5.8, as the measurements were done with the same crystals.

The measurement started by trapping the reasonably large crystal, the number of ions was precisely counted, then the five hours measurement in the continuous regime was carried out, the number of ions was roughly checked, then the five hours measurement was performed in the pulsed regime and the number of ions was precisely counted again. The ions was kicked away from the trap and the measurement was realized in the same way on the scattered laser beam at 397 nm for five hours in the continuous regime and then in the pulsed regime.

The maximal observed count rate in the pulsed regime was measured with the largest crystal containing 275 ions. The five hours measurement contained $N_{TB} = 6\ 428\ 395\ 286$ windows, which equals to the total number of pulse sequences. These sequences contained $N_{S1} = 34\ 691\ 437$ single clicks on APD_1, $N_{S2} = 30\ 857\ 560$ single clicks on APD_2 and $N_C = 166\ 171$ number of coincidences. We estimated the number of photons on input per sequence from the knowledge of

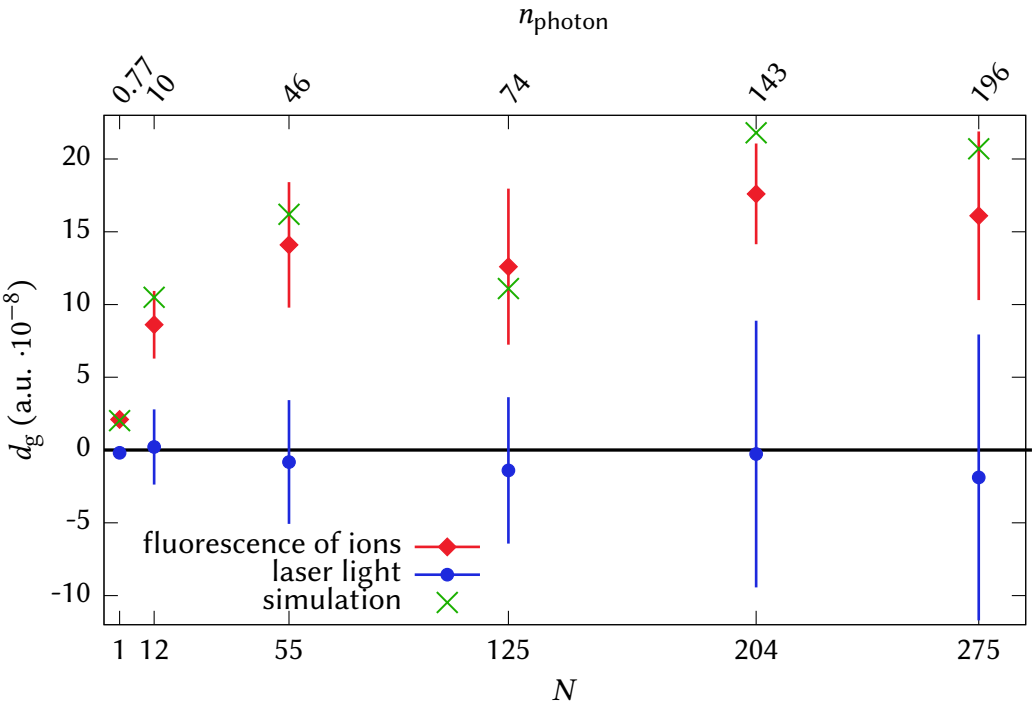

Figure 5.11: The estimated witness of nonclassicality d_g as a function of the number of ions for the fluorescence measured in the pulsed regime. The blue dots represent the same measurement with a laser light and count rate corresponding to the given measurement with ions. The data are provided with one standard deviation of the error bar. The green crosses present the numerical simulation of the distance value. The mean number of emitted photons per sequence n_{photon} is shown above the graph.

optical pumping η_{pump} and number of ions. This gave us a mean number of emitted photons $n_{\text{photon}} = 196$ from the 275 ion crystal and to the best of our knowledge, the value corresponds to the largest photonic field and also the largest system of single-photon emitters on which the discrete nonclassical character of light was demonstrated to the date. The top horizontal axis of the Fig. 5.11 includes the mean number of emitted photons per sequence n_{photon} for other crystals. The theoretical predictions marked as green crosses agree well with the measured distances d_g upon the assumption that each ion is the independent single-photon emitter. The coupling efficiency of each ion was taken into account, see the eq. (5.1). The measurement of distance with a single ion in the trap was fitted to get the detection efficiency for the theoretical model. The rest of the green crosses were calculated without any free fitting parameter, and without assuming any laser excitation inhomogeneity or fluctuations. The simulation considers the ion distribution in concentric shells[A3], which closely resemble the observed spatial distributions of ions

employed in the presented measurements, see the Fig. 5.3.

The measured distances d_g in the pulsed regime scale more favourably than in the continuous regime. This promises better observability and especially scalability to higher ion numbers. The value of distance d_g grow with the number of ions. The evaluation of individual distances d_g together with their error bars resulted in the inequality $d_g(1) < d_g(12)$ with the confidence level of 99.9 % and the inequality $d_g(12) < d_g(55)$ with the confidence level of 99 %. Therefore, distances clearly grow up to 55 ions, beyond 55 ions, the trend is not convincing from point to point. Nevertheless, we carried out the linear weighted fit of the distances for $N \geq 55$, which gave us a mean gradient with its error bar. This provided us with a confidence level of 87 % that the distance value grows from 55 till 275 ions.

The significant technical limit on further scaling of the number of ions in the nonclassical experiment was given by the fast drop of coupling efficiency from emitters shifted in the radial observation direction. We tried to defocus the coupling lens and collect the radiation from a larger area, which resulted in a considerable increase of background, especially from trap electrodes. We filtered out the majority of scattered background by employing 4f scheme with spatial filtration and the estimated radial field of view grew to approximately 20 µm with a small decrease of coupling efficiency. In this configuration, we trapped 1500±200 ions and carried out the measurement in the pulsed regime, which resulted in positive distance $d_g = (9.48 \pm 3.93) \cdot 10^{-7}$ within five hours long run. We were unable to make measurement in continuous regime due to high reflection of 397 nm excitation beam from electrodes. We estimated 534 mean emitted photons, this points to low efficiency of optical pumping. This was caused by highly red detuned 397 nm laser in order to improve the stability of such large crystal.

5.4 Summary

The chapter was focused on our studies of nonclassical properties of light emitted by large ion crystals. The HBT configuration was employed to detect the photon probability distributions of strongly attenuated light scattered from ion crystals, which were excited by continuous and also pulsed laser beams. For single trapped ion, the intensity correlation measurement resulted in $g^{(2)}(0) = 0.064$ in continuous regime with 1 ns window in one-hour measurement and $g^{(2)}(0) = 0.036$ in the pulsed regime with 2.8 µs long sequence in five hours long measurement.

The performed measurements demonstrated the discrete nonclassical character of light from large ion crystals containing up to 275 ions. Additionally, it seems that there is no fundamental limit for further scaling of the number of ions, especially in the pulsed regime, which is enhanced by the absence of excitation 397 nm laser during measurement and by suppressed multi-photon emission. We

observed merely two loses of few ions from crystals during all 14 measurements. The substantial weakness was the coupling efficiency in the radial observation direction, which rapidly decreases due to the magnification of employed optical setup and size of the detection area of the APDs. We made additional measurement with increased radial detection volume, which despite all imperfections of optical detection and stability of 1500±200 ion crystal succeeded in positive distance $d_{\mathrm{g}} = (9.48 \pm 3.93) \cdot 10^{-7}$ with 534 mean value of emitted photons.

Chapter 6

Conclusion

The thesis is dedicated to the studies of fluorescence emitted by trapped and cooled ions. It covers the description of building a new ion trapping apparatus and estimation of the ultimate partial pressure of hydrogen. The apparatus was employed for observing the interference of the emission from tens of ions. The ion crystals served for verification of the preservation nonclassical light emission even for large 3D atomic structures.

6.1 Summary of work

The presented description of construction of a new $^{40}Ca^{+}$ ion trapping setup operating at the room temperature should serve as a solid reference. It covers assembly including the materials choice, cleaning procedures, three-stage bake process. The vacuum pressure is important for lifetime of the crystal. The final background pressure allows trapping tens of ions and their stable storage for many days. This is a crucial property of a scallable system. The quantification of the final partial pressure of hydrogen was carried out by analysis of the formation rate of the CaH^{+} molecules. We observed in total four photochemical reactions during the 51 hours long measurement with a string consisting of 34 $^{40}Ca^{+}$ ions. This puts the upper limit on the partial pressure of hydrogen $P_{H_2} \leq (2.1 \pm 1.1) \cdot 10^{-13}$ mBar for the reaction rate constant k_r [93] and $P_{H_2} \leq (5.5 \pm 2.8) \cdot 10^{-12}$ mBar for k_r [94].

The measurements of phase interference patterns analogous to Young's double slit experiment were presented for selected ion crystals including up to 53 emitters. All patterns were theoretically reproduced by simulation. The previous demonstrations of coherent contribution were limited to a few ions. Our geometric arrangement enhances of observation of a phase-coherent scattering with respect to the number of ions while maintaining the principal possibility of high detection coup-

ling efficiency. The visibilities of the interference patterns remain in the range of 0.31 to 0.53 for all measured crystals. The experiment demonstrated the interaction of coherently scattered light from individual ions of a large crystal, where the addressability of single ions is preserved.

We demonstrated the nonclassical character of fluorescence from several ionic crystals containing hundreds of ions and a single crystal with more than a thousand of ions. The further scaling of the number of ions was technically limited in our setup due to the design of the linear Paul trap and especially due to the optical access and coupling challenges related to efficient coupling of large number of ions to the single photon detection setup. Implementation of optical detection apparatus with larger field of view area at the position of ion crystal could lead to the observation of nonclassical states for even larger structures. The presented measurements prove that the observability of nonclassical properties of light can be boosted to very large photon flux and corresponding number of emitters provided that the thermal fluctuations of emitters can be sufficiently supressed. In turn, this also points to the superb isolation of trapped ion system from the surroundings.

6.2 Outlook

The presented work provides scientific studies, which answer some questions but also naturally open new horizons and several possibilities of examining advanced fundamental phenomena related to the emission of light from trapped ion crystals. These will require technical improvements, which go in hand with some of its practical applications in quantum information processing.

The measurements of interference patterns from linear ion chains were technically limited by inhomogeneous excitation for large crystals. It can be overcome by employing an elliptical profile of the excitation beam and its optical access improvement. The main technical difficulty came from the small collection angle in the axial detection direction caused by coupling through the holes in the tip electrodes. Nevertheless, we currently implement the new ion trapping apparatus with greatly improved axial optical access with up to NA of 0.2. We anticipate the significant improvement of the collective coupling efficiency from long ion strings mediated by directional emission allowed by the observed tunable coherent scattering[40,136]. In principle, further enhancement by employing a low finesse optical resonator along the axial trapping direction can result in a viable path for the achievement of high detection efficiency of light scattered from trapped ions for applications ranging from scalable quantum communication to the high-performance readout of a quantum state in quantum simulations and quantum metrology.

The measurements of temporal photon distribution demonstrated the conservation of nonclassicality for large ion crystals due to excellent control over the trapped ion system. It is another piece of the puzzle of knowledge of nonclassicality leading towards testing other sources like solid-state emitters[154–157] and advanced atomic ensembles[119,158] and its connection to phenomena of superradiance[159,160]. Our measurements substantially shift the observable energy of discrete quantum features of light. It can trigger the construction of intense and macroscopic source of quantum light. We currently test complementary situation, which studies the dependence of observability of sub-Poissonity and photon bunching on the modal structure of the detected field emitted from 3D ionic crystals. Contrary to the presented measurements of nonclassicality for spatially multimode detection, in the opposite situation of polarized and single spatial mode, one expects the idealized textbook[B4] case of light scattering from a large number of phase-jittering light emitters, which in the limit of large crystal results in photon bunching. This shows the intriguing nature of the presented observations and crucial aspect of employment of suitable criteria of nonclassicality. Generally, these types of various experiments can lead to studies of the interaction between the system and its surroundings, which destroys the nonclassical behaviour. Another option is to study the internal dynamics of the system itself. For example, the transition between solid-state and plasma state[152] can be detected by the nonclassical measurement. The situation is suitable for ionic apparatus, which can emulate both states by changing the trapping parameters.

References

Articles covering the presented results

A1 P. Obšil, A. Lešundák, T. Pham, K. Lakhmanskiy, L. Podhora, M. Oral, O. Číp and L. Slodička:
'A room-temperature ion trapping apparatus with hydrogen partial pressure below 10^{-11} mbar',
Review of Scientific Instruments **90**, 083201 (2019).

A2 P. Obšil, A. Lešundák, T. Pham, G. Araneda, M. Čížek, O. Číp, R. Filip and L. Slodička:
'Multipath interference from large trapped ion chains',
New Journal of Physics **21**, 093039 (2019).

A3 P. Obšil, L. Lachman, T. Pham, A. Lešundák, V. Hucl, M. Čížek, J. Hrabina, O. Číp, L. Slodička and R. Filip:
'Nonclassical light from large ensembles of trapped ions',
Physical Review Letters **120**, 253602 (2018).

Other articles published during Ph.D. study

O1 G. Araneda, G. Cerchiari, D. B. Higginbottom, P. Holz, K. Lakhmanskiy, P. Obšil, Y. Colombe and R. Blatt:
'The Panopticon device: An integrated Paul-trap–hemispherical mirror system for quantum optics',
Review of Scientific Instruments **91**, 113201 (2020).

O2 A. Lešundák, T. M. Pham, M. Čížek, P. Obšil, L. Slodička and O. Číp:
'Optical frequency analysis on dark state of a single trapped ion',
Optics Express **28**, 13091–13103 (2020).

O3 L. Podhora, T. Pham, A. Lešundák, P. Obšil, M. Čížek, O. Číp, P. Marek, L. Slodička and R. Filip:
'Unconditional accumulation of nonclassicality in a single-atom mechanical oscillator',
Advanced Quantum Technologies, 2000012 (2020).

O4 J. Mika, L. Podhora, L. Lachman, P. Obšil, J. Hloušek, M. Ježek, R. Filip and L. Slodička:
'Generation of ideal thermal light in warm atomic vapor',
New Journal of Physics **20**, 093002 (2018).

O5 L. Podhora, P. Obšil, I. Straka, M. Ježek and L. Slodička:
'Nonclassical photon pairs from warm atomic vapor using a single driving laser',
Optics Express **25**, 31230–31238 (2017).

Books

B1 R. J. Glauber:
Quantum theory of optical coherence: selected papers and lectures,
(Wiley-VCH, 2007).

B2 R. L. Liboff:
Introductory quantum mechanics,
(Addison-Wesley, 2003).

B3 M. O. Scully and M. S. Zubairy:
Quantum optics,
(Cambridge University Press, 1997).

B4 R. Loudon:
The quantum theory of light,
(OUP Oxford, 2000).

B5 C. Gardiner, P. Zoller and P. Zoller:
Quantum noise: a handbook of markovian and non-markovian quantum stochastic methods with applications to quantum optics,
(Springer Science & Business Media, 2004).

B6 L. Mandel and E. Wolf:
Optical coherence and quantum optics,
(Cambridge University Press, 1995).

B7 A. Chambers:
Modern vacuum physics,
(CRC Press, 2004).

B8 C. Cohen-Tannoudji and D. Guéry-Odelin:
Advances in atomic physics: an overview,
(World Scientific, 2011).

B9 M. Inguscio and L. Fallani:
Atomic physics: precise measurements and ultracold matter,
(OUP Oxford, 2013).

B10 A. Predojević and M. W. Mitchell:
Engineering the atom-photon interaction,
(Springer, 2015).

B11 M. Ladd and P. Rex:
Structure determination by x-ray crystallography,
(Springer, 2013).

B12 C. Cohen-Tannoudji, J. Dupont-Roc and G. Grynberg:
Atom-photon interactions: basic processes and applications,
(Wiley-VCH, 1998).

B13 D. A. Steck:
Quantum and atom optics,
(http://steck.us/teaching, 2007).

Articles, proceedings and theses

1 L. Lachman, L. Slodička and R. Filip:
'Nonclassical light from a large number of independent single-photon emitters',
Scientific Reports **6**, 19760 (2016).

2 A. D. Ludlow, M. M. Boyd, J. Ye, E. Peik and P. O. Schmidt:
'Optical atomic clocks',
Reviews of Modern Physics **87**, 637–701 (2015).

3 C. D. Bruzewicz, J. Chiaverini, R. McConnell and J. M. Sage:
'Trapped-ion quantum computing: progress and challenges',
Applied Physics Reviews **6**, 021314 (2019).

4 J. Zhang, G. Pagano, P. W. Hess, A. Kyprianidis, P. Becker, H. Kaplan, A. V. Gorshkov, Z.-X. Gong and C. Monroe:
'Observation of a many-body dynamical phase transition with a 53-qubit quantum simulator',
Nature **551**, 601 (2017).

5 S. Wehner, D. Elkouss and R. Hanson:
'Quantum internet: A vision for the road ahead',
Science **362**, 6412 (2018).

6 D. Leibfried, R. Blatt, C. Monroe and D. Wineland:
'Quantum dynamics of single trapped ions',
Reviews of Modern Physics **75**, 281–324 (2003).

7 N. Poli, C. W. Oates, P. Gill and G. M. Tino:
'Optical atomic clocks',
La rivista del Nuovo Cimento **36**, 555–624 (2013).

8 S. M. Brewer, J.-S. Chen, A. M. Hankin, E. R. Clements, C. W. Chou, D. J. Wineland, D. B. Hume and D. R. Leibrandt:
'$^{27}Al^{+}$ quantum-logic clock with a systematic uncertainty below 10^{-18}',
Physical Review Letters **123**, 033201 (2019).

9 E. Oelker, R. B. Hutson, C. J. Kennedy, L. Sonderhouse, T. Bothwell, A. Goban, D. Kedar, C. Sanner, J. M. Robinson, G. E. Marti, D. G. Matei, T. Legero, M. Giunta, R. Holzwarth, F. Riehle, U. Sterr and J. Ye:
'Demonstration of 4.8×10^{-17} stability at 1 s for two independent optical clocks',
Nature Photonics **13**, 714–719 (2019).

10 F. Arute, K. Arya, R. Babbush, D. Bacon, J. C. Bardin, R. Barends, R. Biswas, S. Boixo, F. G. Brandao, D. A. Buell et al.:
'Quantum supremacy using a programmable superconducting processor',
Nature **574**, 505–510 (2019).

11 P. W. Shor:
'Polynomial-time algorithms for prime factorization and discrete logarithms on a quantum computer',
SIAM review **41**, 303–332 (1999).

12 T. Monz, D. Nigg, E. A. Martinez, M. F. Brandl, P. Schindler, R. Rines, S. X. Wang, I. L. Chuang and R. Blatt:
'Realization of a scalable shor algorithm',
Science **351**, 1068–1070 (2016).

13 L. K. Grover:
'Quantum mechanics helps in searching for a needle in a haystack',
Physical Review Letters **79**, 325–328 (1997).

14 H. Häffner, C. F. Roos and R. Blatt:
'Quantum computing with trapped ions',
Physics reports **469**, 155–203 (2008).

15 J. I. Cirac and P. Zoller:
'Quantum computations with cold trapped ions',
Physical Review Letters **74**, 4091–4094 (1995).

16 A. Sørensen and K. Mølmer:
'Quantum computation with ions in thermal motion',
Physical Review Letters **82**, 1971–1974 (1999).

17 C. J. Ballance, T. P. Harty, N. M. Linke, M. A. Sepiol and D. M. Lucas:
'High-fidelity quantum logic gates using trapped-ion hyperfine qubits',
Physical Review Letters **117**, 060504 (2016).

18 J. P. Gaebler, T. R. Tan, Y. Lin, Y. Wan, R. Bowler, A. C. Keith, S. Glancy, K. Coakley, E. Knill, D. Leibfried and D. J. Wineland:
'High-fidelity universal gate set for $^{9}Be^{+}$ ion qubits',
Physical Review Letters **117**, 060505 (2016).

19 N. M. Linke, D. Maslov, M. Roetteler, S. Debnath, C. Figgatt, K. A. Landsman, K. Wright and C. Monroe:
'Experimental comparison of two quantum computing architectures',
Proceedings of the National Academy of Sciences **114**, 3305–3310 (2017).

20 V. Schäfer, C. Ballance, K. Thirumalai, L. Stephenson, T. Ballance, A. Steane and D. Lucas:
'Fast quantum logic gates with trapped-ion qubits',
Nature **555**, 75–78 (2018).

21 D. Nigg, M. Mueller, E. A. Martinez, P. Schindler, M. Hennrich, T. Monz, M. A. Martin-Delgado and R. Blatt:
'Quantum computations on a topologically encoded qubit',
Science **345**, 302–305 (2014).

22 M. Żukowski, A. Zeilinger, M. A. Horne and A. K. Ekert:
'"Event-ready-detectors" Bell experiment via entanglement swapping',
Physical Review Letters **71**, 4287–4290 (1993).

23 J.-W. Pan, D. Bouwmeester, H. Weinfurter and A. Zeilinger:
'Experimental entanglement swapping: entangling photons that never interacted',
Physical Review Letters **80**, 3891–3894 (1998).

24 C.-W. Chou, J. Laurat, H. Deng, K. S. Choi, H. De Riedmatten, D. Felinto and H. J. Kimble:
'Functional quantum nodes for entanglement distribution over scalable quantum networks',
Science **316**, 1316–1320 (2007).

25 Y. Wang, M. Um, J. Zhang, S. An, M. Lyu, J.-N. Zhang, L.-M. Duan, D. Yum and K. Kim:
'Single-qubit quantum memory exceeding ten-minute coherence time',
Nature Photonics **11**, 646–650 (2017).

26 M. Bock, P. Eich, S. Kucera, M. Kreis, A. Lenhard, C. Becher and J. Eschner:
'High-fidelity entanglement between a trapped ion and a telecom photon via quantum frequency conversion',
Nature communications **9**, 1–7 (2018).

27 V. Krutyanskiy, M. Meraner, J. Schupp, V. Krcmarsky, H. Hainzer and B. P. Lanyon:
'Light-matter entanglement over 50 km of optical fibre',
npj Quantum Information **5**, 1–5 (2019).

28 M. K. Tey, G. Maslennikov, T. C. Liew, S. A. Aljunid, F. Huber, B. Chng, Z. Chen, V. Scarani and C. Kurtsiefer:
'Interfacing light and single atoms with a lens',
New Journal of Physics **11**, 043011 (2009).

29 Y. R. P. Sortais, H. Marion, C. Tuchendler, A. M. Lance, M. Lamare, P. Fournet, C. Armellin, R. Mercier, G. Messin, A. Browaeys and P. Grangier:
'Diffraction-limited optics for single-atom manipulation',
Physical Review A **75**, 013406 (2007).

30 C. J. Hood, T. W. Lynn, A. C. Doherty, A. S. Parkins and H. J. Kimble:
'The atom-cavity microscope: single atoms bound in orbit by single photons',
Science **287**, 1447–1453 (2000).

31 P. W. H. Pinkse, T. Fischer, P. Maunz and G. Rempe:
'Trapping an atom with single photons',
Nature **404**, 365–368 (2000).

32 L. V. Hau, S. E. Harris, Z. Dutton and C. H. Behroozi:
'Light speed reduction to 17 metres per second in an ultracold atomic gas',
Nature **397**, 594–598 (1999).

33 D. F. Phillips, A. Fleischhauer, A. Mair, R. L. Walsworth and M. D. Lukin:
'Storage of light in atomic vapor',
Physical Review Letters **86**, 783–786 (2001).

34 D. Porras and J. I. Cirac:
'Collective generation of quantum states of light by entangled atoms',
Physical Review A **78**, 053816 (2008).

35 U. Eichmann, J. C. Bergquist, J. J. Bollinger, J. M. Gilligan, W. M. Itano, D. J. Wineland and M. G. Raizen:
'Young's interference experiment with light scattered from two atoms',
Physical Review Letters **70**, 16 (1993).

36 J. Eschner, C. Raab, F. Schmidt-Kaler and R. Blatt:
'Light interference from single atoms and their mirror images',
Nature **413**, 495 (2001).

37 S. Wolf, J. Wechs, J. von Zanthier and F. Schmidt-Kaler:
'Visibility of Young's interference fringes: Scattered light from small ion crystals',
Physical Review Letters **116**, 18 (2016).

38 L. Slodička, G. Hétet, N. Röck, S. Gerber, P. Schindler, M. Kumph, M. Hennrich and R. Blatt:
'Interferometric thermometry of a single sub-doppler-cooled atom',
Physical Review A **85**, 043401 (2012).

39 P. K. Tan, G. H. Yeo, H. S. Poh, A. H. Chan and C. Kurtsiefer:
'Measuring temporal photon bunching in blackbody radiation',
The Astrophysical Journal Letters **789**, L10 (2014).

40 S. Wolf, S. Richter, J. von Zanthier and F. Schmidt-Kaler:
'Light of two atoms in free space: bunching or antibunching?',
Physical Review Letters **124**, 063603 (2020).

41 D. B. Higginbottom, L. Slodička, G. Araneda, L. Lachman, R. Filip, M. Hennrich and R. Blatt:
'Pure single photons from a trapped atom source',
New Journal of Physics **18**, 093038 (2016).

42 C. Kurz, J. Huwer, M. Schug, P. Müller and J. Eschner:
'A high-rate source for single photons in a pure quantum state',
New Journal of Physics **15**, 055005 (2013).

43 H. G. Barros, A. Stute, T. E. Northup, C. Russo, P. O. Schmidt and R. Blatt:
'Deterministic single-photon source from a single ion',
New Journal of Physics **11**, 103004 (2009).

44 W. Paul:
'Electromagnetic traps for charged and neutral particles',
Reviews of Modern Physics **62**, 531–540 (1990).

45 L. S. Brown and G. Gabrielse:
'Geonium theory: physics of a single electron or ion in a penning trap',
Reviews of Modern Physics **58**, 233–311 (1986).

46 R. I. Thompson, T. J. Harmon and M. G. Ball:
'The rotating-saddle trap: a mechanical analogy to RF-electric-quadrupole ion trapping?',
Canadian Journal of Physics **80**, 1433–1448 (2002).

47 J. E. Sträng:
'On the characteristic exponents of floquet solutions to the mathieu equation',
arXiv preprint math-ph/0510076 (2005).

48 R. Wester:
'Radiofrequency multipole traps: tools for spectroscopy and dynamics of cold molecular ions',
Journal of Physics B: Atomic, Molecular and Optical Physics **42**, 154001 (2009).

49 S. Seidelin, J. Chiaverini, R. Reichle, J. J. Bollinger, D. Leibfried, J. Britton, J. H. Wesenberg, R. B. Blakestad, R. J. Epstein, D. B. Hume, W. M. Itano, J. D. Jost, C. Langer, R. Ozeri, N. Shiga and D. J. Wineland:
'Microfabricated surface-electrode ion trap for scalable quantum information processing',
Physical Review Letters **96**, 253003 (2006).

50 J. Labaziewicz, Y. Ge, P. Antohi, D. Leibrandt, K. R. Brown and I. L. Chuang:
'Suppression of heating rates in cryogenic surface-electrode ion traps',
Physical Review Letters **100**, 013001 (2008).

51 R. E. March:
'An introduction to quadrupole ion trap mass spectrometry',
Journal of mass spectrometry **32**, 351–369 (1997).

52 R. E. March:
'Quadrupole ion trap mass spectrometry: a view at the turn of the century',
International Journal of Mass Spectrometry **200**, 285–312 (2000).

53 J. P. Schiffer:
'Phase transitions in anisotropically confined ionic crystals',
Physical Review Letters **70**, 818–821 (1993).

54 D. F. V. James:
'Quantum dynamics of cold trapped ions with application to quantum computation',
Applied Physics B **66**, 181–190 (1998).

55 J. R. De Laeter, J. K. Böhlke, P. De Bièvre, H. Hidaka, H. Peiser, K. Rosman and P. Taylor:
'Atomic weights of the elements. Review 2000 (IUPAC Technical Report)',
Pure and Applied Chemistry **75**, 683–800 (2003).

56 C. Schuck, M. Almendros, F. Rohde, M. Hennrich and J. Eschner:
'Two-color photoionization of calcium using SHG and LED light',
Applied Physics B **100**, 765–771 (2010).

57 E. J. Salumbides, V. Maslinskas, I. M. Dildar, A. L. Wolf, E.-J. van Duijn, K. S. E. Eikema and W. Ubachs:
'High-precision frequency measurement of the 423-nm Ca i line',
Physical Review A **83**, 012502 (2011).

58 J. Jin and D. A. Church:
'Precision lifetimes for the Ca^+ 4p ^{2}p levels: experiment challenges theory at the 1% level',
Physical Review Letters **70**, 3213–3216 (1993).

59 P. A. Barton, C. J. S. Donald, D. M. Lucas, D. A. Stevens, A. M. Steane and D. N. Stacey:
'Measurement of the lifetime of the $3d^2D_{5/2}$ state in $^{40}Ca^+$',
Physical Review A **62**, 032503 (2000).

60 M. Chwalla, J. Benhelm, K. Kim, G. Kirchmair, T. Monz, M. Riebe, P. Schindler, A. S. Villar, W. Hänsel, C. F. Roos, R. Blatt, M. Abgrall, G. Santarelli, G. D. Rovera and P. Laurent:
'Absolute frequency measurement of the $^{40}Ca^+$ $4s\ ^2S_{1/2} - 3d\ ^2D_{5/2}$ clock transition',
Physical Review Letters **102**, 023002 (2009).

61 M. Ramm, T. Pruttivarasin, M. Kokish, I. Talukdar and H. Häffner:
'Precision measurement method for branching fractions of excited $P_{1/2}$ states applied to $^{40}Ca^+$',
Physical Review Letters **111**, 023004 (2013).

62 H. Oberst:
'Resonance fluorescence of single barium ions',
Ph.D. thesis (1999).

63 H. J. Kimble, M. Dagenais and L. Mandel:
'Photon antibunching in resonance fluorescence',
Physical Review Letters **39**, 691–695 (1977).

64 P. Grangier, G. Roger and A. Aspect:
'Experimental evidence for a photon anticorrelation effect on a beam splitter: a new light on single-photon interferences',
Europhysics Letters (EPL) **1**, 173–179 (1986).

65 A. Aspect, C. Imbert and G. Roger:
'Absolute measurement of an atomic cascade rate using a two photon coincidence technique. Application to the $4p^2{}^1S_0$-$4s4p^1P_1$-$4s^2{}^1S_0$ cascade of calcium excited by a two photon absorption',
Optics Communications **34**, 46–52 (1980).

66 N. Marquardt:
'Introduction to the principles of vacuum physics',
Cern (1999).

67 S. G. Jennings:
'The mean free path in air',
Journal of Aerosol Science **19**, 159–166 (1988).

68 N. Friis, O. Marty, C. Maier, C. Hempel, M. Holzäpfel, P. Jurcevic, M. B. Plenio, M. Huber, C. Roos, R. Blatt and B. Lanyon:
'Observation of entangled states of a fully controlled 20-qubit system',
Physical Review X **8**, 021012 (2018).

69 T. Monz, P. Schindler, J. T. Barreiro, M. Chwalla, D. Nigg, W. A. Coish, M. Harlander, W. Hänsel, M. Hennrich and R. Blatt:
'14-qubit entanglement: creation and coherence',
Physical Review Letters **106**, 130506 (2011).

70 J. Keller, T. Burgermeister, D. Kalincev, A. Didier, A. Kulosa, T. Nordmann, J. Kiethe and T. Mehlstäubler:
'Controlling systematic frequency uncertainties at the 10^{-19} level in linear Coulomb crystals',
Physical Review A **99**, 013405 (2019).

71 J. Kiethe, R. Nigmatullin, D. Kalincev, T. Schmirander and T. Mehlstäubler:
'Probing nanofriction and aubry-type signatures in a finite self-organized system',
Nature Communications **8**, 15364 (2017).

72 C. Maier, T. Brydges, P. Jurcevic, N. Trautmann, C. Hempel, B. P. Lanyon, P. Hauke, R. Blatt and C. F. Roos:
'Environment-assisted quantum transport in a 10-qubit network',
Physical Review Letters **122**, 050501 (2019).

73 S. Ulm, J. Roßnagel, G. Jacob, C. Degünther, S. Dawkins, U. Poschinger, R. Nigmatullin, A. Retzker, M. Plenio, F. Schmidt-Kaler and K. Singer:
'Observation of the kibble–zurek scaling law for defect formation in ion crystals',
Nature communications **4**, 2290 (2013).

74 C. D. Bruzewicz, R. McConnell, J. Chiaverini and J. M. Sage:
'Scalable loading of a two-dimensional trapped-ion array',
Nature Communications **7**, 13005 (2016).

75 P. Micke, J. Stark, S. A. King, T. Leopold, T. Pfeifer, L. Schmöger, M. Schwarz, L. J. Spieß, P. O. Schmidt and J. R. Crespo López-Urrutia:
'Closed-cycle, low-vibration 4 k cryostat for ion traps and other applications',
Review of Scientific Instruments **90**, 065104 (2019).

76 G. Pagano, P. W. Hess, H. B. Kaplan, W. L. Tan, P. Richerme, P. Becker, A. Kyprianidis, J. Zhang, E. Birckelbaw, M. R. Hernandez, Y. Wu and C. Monroe:
'Cryogenic trapped-ion system for large scale quantum simulation',
Quantum Science and Technology **4**, 014004 (2018).

77 M. Brownnutt, M. Kumph, P. Rabl and R. Blatt:
'Ion-trap measurements of electric-field noise near surfaces',
Reviews of Modern Physics **87**, 1419 (2015).

78 Q. A. Turchette, B. E. King, D. Leibfried, D. M. Meekhof, C. J. Myatt, M. A. Rowe, C. A. Sackett, C. S. Wood, W. M. Itano, C. Monroe et al.:
'Heating of trapped ions from the quantum ground state',
Physical Review A **61**, 063418 (2000).

79 K. Lakhmanskiy, P. Holz, D. Schärtl, B. Ames, R. Assouly, T. Monz, Y. Colombe and R. Blatt:
'Observation of superconductivity and surface noise using a single trapped ion as a field probe',
Physical Review A **99**, 023405 (2019).

80 L. D. Carr, D. DeMille, R. V. Krems and J. Ye:
'Cold and ultracold molecules: science, technology and applications',
New Journal of Physics **11**, 055049 (2009).

81 H. Lehmitz, J. Hattendorf-Ledwoch, R. Blatt and H. Harde:
'Population trapping in excited Yb ions',
Physical Review letters **62**, 2108 (1989).

82 A. Hankin, E. Clements, Y. Huang, S. Brewer, J.-S. Chen, C. Chou, D. Hume and D. Leibrandt:
'Systematic uncertainty due to background-gas collisions in trapped-ion optical clocks',
Physical Review A **100**, 033419 (2019).

83 R. Calder and G. Lewin:
'Reduction of stainless-steel outgassing in ultra-high vacuum',
British Journal of Applied Physics **18**, 1459 (1967).

84 B. Roth, P. Blythe, H. Wenz, H. Daerr and S. Schiller:
'Ion-neutral chemical reactions between ultracold localized ions and neutral molecules with single-particle resolution',
Physical Review A **73**, 042712 (2006).

85 K. Sugiyama and J. Yoda:
'Production of YbH^+ by chemical reaction of Yb^+ in excited states with H_2 gas',
Physical Review A **55**, R10 (1997).

86 T. M. Hoang, Y.-Y. Jau, R. Overstreet and P. D. D. Schwindt:
'YbH^+ formation in an ytterbium ion trap',
Physical Review A **101**, 022705 (2020).

87 K. Mølhave and M. Drewsen:
'Formation of translationally cold MgH^+ and MgD^+ molecules in an ion trap',
Physical Review A **62**, 011401 (2000).

88 P. F. Staanum, K. Højbjerre, R. Wester and M. Drewsen:
'Probing isotope effects in chemical reactions using single ions',
Physical Review Letters **100**, 243003 (2008).

89 P. F. Staanum, K. Højbjerre, P. S. Skyt, A. K. Hansen and M. Drewsen:
'Rotational laser cooling of vibrationally and translationally cold molecular ions',
Nature Physics **6**, 271 (2010).

90 T. Schneider, B. Roth, H. Duncker, I. Ernsting and S. Schiller:
'All-optical preparation of molecular ions in the rovibrational ground state',
Nature Physics **6**, 275 (2010).

91 S. Lépine, R. M. Rich and M. M. Shara:
'LSR 1610−0040: The First Early-Type L Subdwarf',
The Astrophysical Journal Letters **591**, L49 (2003).

92 D. Petitprez, B. Lemoine, C. Demuynck, J. Destombes and B. Macke:
'Infrared diode laser spectroscopy of CaH and CaD (X 2Σ+). Determination of mass-independent parameters',
The Journal of Chemical Physics **91**, 4462−4467 (1989).

93 N. Kimura, K. Okada, T. Takayanagi, M. Wada, S. Ohtani and H. A. Schuessler:
'Sympathetic crystallization of CaH^+ produced by a laser-induced reaction',
Physical Review A **83**, 033422 (2011).

94 A. K. Hansen, M. A. Sørensen, P. F. Staanum and M. Drewsen:
'Single-ion recycling reactions',
Angewandte Chemie International Edition **51**, 7960−7962 (2012).

95 P. Weck, P. Stancil and K. Kirby:
'Theoretical study of the rovibrationally resolved transitions of CaH',
The Journal of Chemical Physics **118**, 9997−10005 (2003).

96 R. Rugango, A. T. Calvin, S. Janardan, G. Shu and K. R. Brown:
'Vibronic spectroscopy of sympathetically cooled CaH^+',
ChemPhysChem **17**, 3764−3768 (2016).

97 C.-w. Chou, C. Kurz, D. B. Hume, P. N. Plessow, D. R. Leibrandt and D. Leibfried:
'Preparation and coherent manipulation of pure quantum states of a single molecular ion',
Nature **545**, 203 (2017).

98 M. Guggemos:
'Precision spectroscopy with trapped $^{40}Ca^+$ and $^{27}Al^+$ ions',
Ph.D. thesis (2017).

99 S. V. Kagwade, C. R. Clayton, D. Chidambaram and G. P. Halada:
'Photochemical breakdown of acetone on copper',
Electrochimica Acta **46**, 2337−2342 (2001).

100 L. Westerberg, B. Hjörvarsson, E. Wallén and A. Mathewson:
'Hydrogen content and outgassing of air-baked and vacuum-fired stainless steel',
Vacuum **48**, 771−773 (1997).

101 W. Prins and J. J. Hermans:
'Theory of permeation through metal coated polymer films',
Journal of Physical Chemistry **63** (1959).

102 A. Lešundák:
'Distance measurements with mode-filtered frequency comb and analysis of fluorescence from trapped ion at modulated dark state',
Ph.D. thesis (2019).

103 C. Hempel:
'Digital quantum simulation, schrödinger cat state spectroscopy and setting up a linear ion trap',
Ph.D. thesis (2014).

104 H. A. Fürst:
'Trapped ions in a bath of ultracold atoms',
Ph.D. thesis (2019).

105 A. H. Nizamani, M. A. Rind, N. M. Shaikh, A. H. Moghal and H. Saleem:
'Versatile ultra high vacuum system for ion trap experiments: design and implementation',
International Journal of Advancements in Research & Technology **2** (2013).

106 G. Araneda, S. Walser, Y. Colombe, D. B. Higginbottom, J. Volz, R. Blatt and A. Rauschenbeutel:
'Wavelength-scale errors in optical localization due to spin–orbit coupling of light',
Nature physics **15**, 17–21 (2019).

107 R. H. Lehmberg:
'Radiation from an N-atom system. I. General formalism',
Physical Review A **2**, 883 (1970).

108 C. Skornia, J. v. Zanthier, G. S. Agarwal, E. Werner and H. Walther:
'Nonclassical interference effects in the radiation from coherently driven uncorrelated atoms',
Physical Review A **64**, 063801 (2001).

109 R. T. Sutherland and F. Robicheaux:
'Collective dipole-dipole interactions in an atomic array',
Physical Review A **94**, 013847 (2016).

110 A. L. Patterson:
'A direct method for the determination of the components of interatomic distances in crystals',
Zeitschrift für Kristallographie-Crystalline Materials **90**, 517–542 (1935).

111 G. Birkl, M. Gatzke, I. H. Deutsch, S. L. Rolston and W. D. Phillips:
'Bragg scattering from atoms in optical lattices',
Physical Review Letters **75**, 2823 (1995).

112 C. Weitenberg, P. Schauß, T. Fukuhara, M. Cheneau, M. Endres, I. Bloch and S. Kuhr:
'Coherent light scattering from a two-dimensional mott insulator',
Physical Review Letters **106**, 215301 (2011).

113 M. Weidemüller, A. Hemmerich, A. Görlitz, T. Esslinger and T. W. Hänsch:
'Bragg diffraction in an atomic lattice bound by light',
Physical Review Letters **75**, 4583 (1995).

114 S. Slama, C. von Cube, B. Deh, A. Ludewig, C. Zimmermann and P. W. Courteille:
'Phase-sensitive detection of bragg scattering at 1D optical lattices',
Physical Review Letters **94**, 193901 (2005).

115 G. Raithel, G. Birkl, A. Kastberg, W. D. Phillips and S. L. Rolston:
'Cooling and localization dynamics in optical lattices',
Physical Review Letters **78**, 630 (1997).

116 A. Schilke, C. Zimmermann, P. W. Courteille and W. Guerin:
'Photonic band gaps in one-dimensionally ordered cold atomic vapors',
Physical Review Letters **106**, 223903 (2011).

117 H. L. Sørensen, J.-B. Béguin, K. W. Kluge, I. Iakoupov, A. S. Sørensen, J. H. Müller, E. S. Polzik and J. Appel:
'Coherent backscattering of light off one-dimensional atomic strings',
Physical Review Letters **117**, 133604 (2016).

118 M. Weidemüller, A. Görlitz, T. W. Hänsch and A. Hemmerich:
'Local and global properties of light-bound atomic lattices investigated by bragg diffraction',
Physical Review A **58**, 4647 (1998).

119 A. Neuzner, M. Körber, O. Morin, S. Ritter and G. Rempe:
'Interference and dynamics of light from a distance-controlled atom pair in an optical cavity',
Nature Photonics **10**, 303–306 (2016).

120 J. N. Tan, J. J. Bollinger, B. Jelenkovic and D. Wineland:
'Long-range order in laser-cooled, atomic-ion wigner crystals observed by bragg scattering',
Physical Review Letters **75**, 4198 (1995).

121 W. M. Itano, J. J. Bollinger, J. N. Tan, B. Jelenković, X.-P. Huang and D. Wineland:
'Bragg diffraction from crystallized ion plasmas',
Science **279**, 686–689 (1998).

122 T. Kauten, R. Keil, T. Kaufmann, B. Pressl, Č. Brukner and G. Weihs:
'Obtaining tight bounds on higher-order interferences with a 5-path interferometer',
New Journal of Physics **19**, 033017 (2017).

123 E. Shahmoon, M. D. Lukin and S. F. Yelin:
'Quantum optomechanics of a two-dimensional atomic array',
Physical Review A **101**, 063833 (2020).

124 W. M. Itano, J. C. Bergquist, J. J. Bollinger, D. J. Wineland, U. Eichmann and M. G. Raizen:
'Complementarity and young's interference fringes from two atoms',
Physical Review A **57**, 4176–4187 (1998).

125 C. Cabrillo, J. I. Cirac, P. Garcia-Fernandez and P. Zoller:
'Creation of entangled states of distant atoms by interference',
Physical Review A **59**, 1025 (1999).

126 L. Slodička, G. Hétet, N. Röck, P. Schindler, M. Hennrich and R. Blatt:
'Atom-atom entanglement by single-photon detection',
Physical Review Letters **110**, 083603 (2013).

127 C. Thiel, J. von Zanthier, T. Bastin, E. Solano and G. S. Agarwal:
'Generation of symmetric dicke states of remote qubits with linear optics',
Physical Review Letters **99**, 193602 (2007).

128 A. Maser, R. Wiegner, U. Schilling, C. Thiel and J. von Zanthier:
'Versatile source of polarization-entangled photons',
Physical Review A **81**, 053842 (2010).

129 Z. Ficek and R. Tanaś:
'Entangled states and collective nonclassical effects in two-atom systems',
Physics Reports **372**, 369–443 (2002).

130 T. Bastin, C. Thiel, J. von Zanthier, L. Lamata, E. Solano and G. S. Agarwal:
'Operational determination of multiqubit entanglement classes via tuning of local operations',
Physical Review Letters **102**, 053601 (2009).

131 W. Vogel and D.-G. Welsch:
'Squeezing pattern in resonance fluorescence from a regular N-atom system',
Physical Review Letters **54**, 1802 (1985).

132 R. G. DeVoe and R. G. Brewer:
'Observation of superradiant and subradiant spontaneous emission of two trapped ions',
Physical Review Letters **76**, 2049 (1996).

133 L. L. Jin, M. Macovei, S. Q. Gong, C. H. Keitel and J. Evers:
'Squeezing in strong light scattered by a regular structure of atoms',
Optics Communications **283**, 790–794 (2010).

134 C. J. Mewton and Z. Ficek:
'Radiative properties of a linear chain of coupled qubits',
Journal of Physics B **40**, S181 (2007).

135 J. P. Clemens, L. Horvath, B. C. Sanders and H. J. Carmichael:
'Collective spontaneous emission from a line of atoms',
Physical Review A **68**, 023809 (2003).

136 G. Araneda, D. B. Higginbottom, L. Slodička, Y. Colombe and R. Blatt:
'Interference of single photons emitted by entangled atoms in free space',
Physical Review Letters **120**, 193603 (2018).

137 B. Casabone, K. Friebe, B. Brandstätter, K. Schüppert, R. Blatt and T. E. Northup:
'Enhanced quantum interface with collective ion-cavity coupling',
Physical Review Letters **114**, 023602 (2015).

138 S. Oppel, R. Wiegner, G. S. Agarwal and J. von Zanthier:
'Directional superradiant emission from statistically independent incoherent nonclassical and classical sources',
Physical Review Letters **113**, 263606 (2014).

139 T. Wong, S. M. Tan, M. J. Collett and D. F. Walls:
'Interference of resonance fluorescence from two four-level atoms',
Physical Review A **55**, 1288–1299 (1997).

140 D. Rotter:
'Quantum feedback and quantum correlation measurements with a single barium ion',
Ph.D. thesis (2008).

141 A. Härter, A. Krükow, A. Brunner and J. H. Denschlag:
'Long-term drifts of stray electric fields in a paul trap',
Applied Physics B **114**, 275–281 (2014).

142 H. Tamura, H. Nguyen, P. R. Berman and A. Kuzmich:
'Phase matching in lower dimensions',
Physical Review Letters **125**, 163601 (2020).

143 R. Filip and L. Lachman:
'Hierarchy of feasible nonclassicality criteria for sources of photons',
Physical Review A **88**, 043827 (2013).

144 R. W. Hasse and V. V. Avilov:
'Structure and madelung energy of spherical coulomb crystals',
Physical Review A **44**, 4506–4515 (1991).

145 M. Drewsen, C. Brodersen, L. Hornekær, J. S. Hangst and J. P. Schifffer:
'Large ion crystals in a linear paul trap',
Physical Review Letters **81**, 2878 (1998).

146 H. Totsuji, T. Kishimoto, C. Totsuji and K. Tsuruta:
'Competition between two forms of ordering in finite coulomb clusters',
Physical Review Letters **88**, 125002 (2002).

147 K. Okada, M. Wada, T. Takayanagi, S. Ohtani and H. A. Schuessler:
'Characterization of ion coulomb crystals in a linear paul trap',
Physical Review A **81**, 013420 (2010).

148 F. Diedrich and H. Walther:
'Nonclassical radiation of a single stored ion',
Physical Review Letters **58**, 203–206 (1987).

149 M. Schubert, I. Siemers, R. Blatt, W. Neuhauser and P. E. Toschek:
'Photon antibunching and non-poissonian fluorescence of a single three-level ion',
Physical Review Letters **68**, 3016–3019 (1992).

150 A. Stute, B. Casabone, B. Brandstätter, K. Friebe, T. E. Northup and R. Blatt:
'Quantum-state transfer from an ion to a photon',
Nature photonics **7**, 219–222 (2013).

151 R. G. Brewer:
'Two-ion superradiance theory',
Physical Review A **52**, 2965–2970 (1995).

152 L. Hornekær and M. Drewsen:
'Formation process of large ion coulomb crystals in linear paul traps',
Physical Review A **66**, 013412 (2002).

153 P. Maunz, D. Moehring, S. Olmschenk, K. C. Younge, D. N. Matsukevich and C. Monroe:
'Quantum interference of photon pairs from two remote trapped atomic ions',
Nature Physics **3**, 538–541 (2007).

154 O. A. Shcherbina, G. A. Shcherbina, M. Manceau, S. Vezzoli, L. Carbone, M. De Vittorio, A. Bramati, E. Giacobino, M. V. Chekhova and G. Leuchs:
'Photon correlations for colloidal nanocrystals and their clusters',
Optics Letters **39**, 1791–1794 (2014).

155 L. J. Rogers, K. D. Jahnke, T. Teraji, L. Marseglia, C. Müller, B. Naydenov, H. Schauffert, C. Kranz, J. Isoya, L. P. McGuinness and F. Jelezko:
'Multiple intrinsically identical single-photon emitters in the solid-state',
Nature Communications **5**, 4739 (2014).

156 C. Palacios-Berraquero, D. M. Kara, A. R.-P. Montblanch, M. Barbone, P. Latawiec, D. Yoon, A. K. Ott, M. Loncar, A. C. Ferrari and M. Atatüre:
'Large-scale quantum-emitter arrays in atomically thin semiconductors',
Nature Communications **8**, 15093 (2017).

157 E. Moreva, P. Traina, J. Forneris, I. P. Degiovanni, S. Ditalia Tchernij, F. Picollo, G. Brida, P. Olivero and M. Genovese:
'Direct experimental observation of nonclassicality in ensembles of single-photon emitters',
Phys. Rev. B **96**, 195209 (2017).

158 T. E. Northup and R. Blatt:
'Quantum information transfer using photons',
Nature Photonics **8**, 356–363 (2014).

159 D. Bhatti, J. Von Zanthier and G. S. Agarwal:
'Superbunching and nonclassicality as new hallmarks of superradiance',
Scientific Reports **5**, 17335 (2015).

160 F. Jahnke, C. Gies, M. Aßmann, M. Bayer, H. Leymann, A. Foerster, J. Wiersig, C. Schneider, M. Kamp and S. Höfling:
'Giant photon bunching, superradiant pulse emission and excitation trapping in quantum-dot nanolasers',
Nature Communications **7**, 11540 (2016).